Porous Silicon Multilayers For Gigahertz Bulk Acoustic Wave Devices

Thomas, Leigh-Anne

Award date:
2011

Awarding institution:
University of Bath

Porous Silicon Multilayers For Gigahertz Bulk Acoustic Wave Devices

Leigh-Anne Thomas

A thesis submitted for the degree of Doctor of Philosophy
University of Bath
Department of Physics
July 2011

Contents

List of Tables and Figures **I**

List of Abbreviations and Symbols **IX**

Publications Related to this Thesis **XIV**

Abstract **1**

1 Introduction **2**

1.1 Porous Silicon 2

1.2 Applications of Multilayers 3

2 Elastic Properties of Bulk Materials **8**

2.1 Directional Dependence of the Elastic Properties of a Cubic Crystal System 12

2.1.1 Directional Dependence of Wave Velocity 18

2.2 Elastic Properties of a Tetragonal Crystal System 21

3 Properties of Multilayered Structures **25**

3.1 Bragg Mirrors 28

3.2 Symmetric and Asymmetric Mirrors 35

3.3 Impedance Profiling: Bragg Mirrors and Rugate Filters 39

3.4 Optical Properties of ‘Acoustic’ Mirrors 41

3.5 Fabry-Perot Filters (Microcavities) 42

4	**Electrochemical Etching of Porous Silicon**	**45**
4.1	Etching Procedure	52
4.2	Fabrication of Porous Silicon Multilayers	57
4.2.1	Bragg Mirrors	58
4.2.2	Rugate Filters	60
4.2.3	Fabry-Perot Filters (Microcavities)	61
4.3	Effect of the Inclusion of Etch Breaks	62
5	**Characterisation of Porous Silicon Layers**	**68**
5.1	Layer Thickness and Porosity	68
5.2	Effective Refractive Index of Single Porous Silicon Layers	69
5.3	Effective Medium Approximations	76
5.4	Acoustic Transmission Measurements through Porous Silicon Layers	81
5.4.1	Longitudinal Velocity Dependence upon Porosity	84
5.4.2	Acoustic Transmission Measurements through Multi-Layered Porous Silicon	90
5.5	Atomic Force Microscopy Imaging of Porous Silicon	91
5.6	Optical Characterisation of Porous Silicon Multilayers	96
6	**Models of Porous Silicon Multilayers**	**100**
6.1	Bragg Mirror Model	101
6.2	Rugate Filter Model	105
6.3	Effect of Symmetry on the Modes of a Bragg Mirror with the Fundamental Mode at 20 GHz	109
6.4	Interface Roughness Effects	113
7	**Experimental Measurements of Porous Silicon Multilayers**	**120**
7.1	Bragg Mirrors	120

7.1.1 Symmetric and Asymmetric Bragg Mirrors 123
7.1.2 Effect of Etch Breaks on Porous Silicon Bragg Mirrors 124
7.2 Rugate Filters 126
7.2.1 Effect of Etch Breaks on Porous Silicon Rugate Filters 129
7.2.2 Porous Silicon Acoustic Rugate Filter with a Single Stopband 131
7.3 Fabry-Perot Filters (Microcavities) 132
7.4 Apodisation and Impedance-Matching 134
7.5 Collaborative Work with the University of Nottingham 137
7.5.1 Fabrication and Characterisation of Porous Silicon Multilayers for 20 GHz Applications 138
7.5.2 Pump-Probe Experiment on Porous Silicon Multilayers for 20 GHz Applications 141

8 Loss and Elastic Properties of Porous Silicon 146
8.1 Loss Mechanisms 147
8.1.1 Attenuation 148
8.1.2 Scattering at Boundaries 153
8.1.3 Measured Loss in Single-Layered Porous Silicon 154
8.2 Elastic Properties of Porous Silicon 161
8.2.1 Influence of Pore Geometry on the Young's Modulus of Porous Silicon 165

Conclusions 168

Acknowledgements 170

Appendix XV

References XVII

List of Tables and Figures

Figure 1.1 (Left) Conventional SMR with two electrodes. (Right) Cross-sectional SEM image of a seven-layer Mo/SiO_2 Bragg reflector for use at 2.5 GHz.

Figure 2.1 Longitudinal, vertical shear and horizontal shear wave examples.

Figure 2.2 The seven crystal systems showing the unit cell for each of the fourteen Bravais lattices.

Figure 2.3 Model of a Silicon crystal seen along the [100] (left) and [110] (right) crystallographic directions.

Figure 2.4 Cubic crystal with [100], [110] and [111] directions showing α, β, γ with respect to x, y, z axes shown for the [110] direction only.

Figure 2.5 Young's modulus of gold (cubic symmetry) where c_{11}=185.0GPa, c_{12}=158.0GPa and c_{44}=39.7GPa.

Figure 2.6 Slowness Surface for an isotropic solid for propagation in an arbitrary plane.

Figure 2.7 (Above) Slowness surface for an anisotropic solid with cubic symmetry for propagation in a cube face (GaAs) and (Below) longitudinal velocity V_L shown for travel in the [100] direction along the x-axis for wave propagation through (100) plane.

Table 2.1 Acoustic velocities through Si in each crystallographic direction.

Figure 2.8 Slowness surface for an anisotropic solid with tetragonal symmetry for propagation in a 'cube' face (rutile).

Figure 3.1 Reflection of a normally incident wave at a plane boundary.

Figure 3.2 (Left) Bragg reflector consisting of a stack of multilayers of high Z_1 and low Z_2 acoustic impedance layers of thickness d_1 and d_2 on a cSi substrate and (Right) increasing reflectivity of the stopband with an increasing number of layers.

Figure 3.3 Optical Bragg mirror with fundamental stopband at 700 nm.

Figure 3.4 The porosity dependence of the effective acoustic impedance profile for p++ Si wafers.

Figure 3.5 (Left) As the number of pairs of layers in the stack N is increased, the transmittance of acoustic waves through the stack decreases and

(Right) the larger the impedance mismatch between the layer pairs, the less pairs are needed to obtain a deep transmittance stopband.

Figure 3.6 Calculated dispersion relations for a (left) symmetrical and (right) asymmetrical multilayered mirror with the parameters stated in figure 3.7.

Figure 3.7 Examples of balanced (left) and unbalanced (right) Bragg mirrors. The parameters used for these simulations are as follows, $d1$=2.089μm $d2$=1.677μm $p1$=0.645 $p2$=0.735 (left) and $d1$=2.168μm $d2$=1.05μm $p1$=0.61 $p2$=0.71 (right) where both mirrors have N=15 pairs of layers.

Figure 3.8 (Left) Symmetric Bragg mirror for $\tau_1 = \tau_2$ with parameters d_1=1.31μm and d_2=1.44μm and (Right) asymmetric Bragg mirror for $\tau_1 = 5\,\tau_2$ with parameters d_1=2.19μm and d_2=0.48μm.

Figure 3.9 Acoustic impedance profile for a Bragg mirror (top) and a rugate filter (bottom).

Figure 3.10 Effect of the acoustic impedance profile on the response of the acoustic multi-layer designed for $d1$=$d2$=1.4μm $p1$=0.42 $p2$=0.56 and N=15.

Figure 3.11 Optical (left) and acoustic (right) simulations of a Bragg mirror and rugate filter with $d1$=$d2$=1.05μm $p1$=0.605 $p2$=0.665 N=20.

Figure 3.12 Example of a pSi optical Microcavity with Q-factor ~1,450.

Figure 3.13 Layer structure describing a micro-cavity which contains a defect cavity layer sandwiched between two Bragg mirrors.

Figure 4.1 PSi multilayer seen on the surface of a Si wafer.

Figure 4.2 SEM images of the interface between bulk and pSi for p-doped <100> silicon electrodes anodized in ethanoic HF.

Figure 4.3 Pore morphology in the (100) and (111) planes.

Figure 4.4 SEM images of multilayered pSi without a clean cleave so that a (Left) 3-D view of the layered system is visible and shows the (110) plane at an angle to the substrate for sample #6 and (Right) the wider pore diameter for a higher porosity layer on top of a lower porosity layer for sample #3.

Figure 4.5 Micrographs of pSi structures. Column-like appearance of pSi in [100] direction. (Left) PSi multilayer on cSi substrate. (Right) PSi at the cSi interface.

Figure 4.6 Reaction of electrochemical etching of Si in HF based ethanoic solution.

Figure 4.7 Electrochemical etch cell set-up.

Figure 4.8 Calibration curves for heavily boron doped SSP Si wafers etched in the [100] crystallographic direction for wafers with resistivity of 1 – 5 mΩ cm with best fit through data for (a) etch rate and (b) porosity as a function of the current.

Figure 4.9 Current density profile used to fabricate Bragg mirrors alongside an SEM contrast image of the alternating layers of high (dark) and low (light) porosity. The SEM scale shown is for 2 μm for sample #50. Lower porosity layers have higher electron density and so show up as lighter regions.

Figure 4.10 (a) Current-time etch profile of one cycle used for sample #52 and (b) SEM image of pSi rugate filter sample #52.

Figure 4.11 Enlarged section of layers next to the substrate for rugate sample #52.

Figure 4.12 SEM image of (Right) pSi microcavity on bulk Si substrate and (Left) defect layer in pSi microcavity for sample # 41.

Figure 4.13 Bragg mirror sample #1 etched without etch breaks showing HF depletion throughout the layers. Layers become thinner towards the substrate (right hand side) and darker (due to lower electron density) as the porosity increases and the mirror becomes chirped.

Figure 4.14 (a) SEM image of a pSi rugate filter sample #23 etched with 32 sub-layers and (c) pSi Bragg mirror sample #42 (b) SEM contrast profile of the pSi rugate filter of (a) showing filter period thickness of 2.14 μm and (d) Bragg mirror of (c) sample #42.

Figure 4.15 (a) Bottom and (b) top 4 pairs of AB layers of sample #42 and (c) contrast profile taken through the Bragg mirror sample #42 also shown in figure 4.14(c).

Figure 5.1 Optical Fabry-Perot set-up for measuring the effective refractive index of the porous layer.

Figure 5.2 Fabry-Perot interference pattern seen from a single layered pSi sample with a porosity of 70%.

Figure 5.3 Single pSi layer on bulk cSi substrate acting as a Fabry-Perot interferometer.

Figure 5.4 Real n(E) and imaginary k(E) parts of the refractive index of Si showing the dispersion curves for this material.

Figure 5.5 Different EMAs for calculating porosity using effective refractive index *n* of layer.

Figure 5.6 (Top) Transducer set-up for S_{21} transmission measurements and (Bottom) close up of transducers with wave propagation through the sample.

Figure 5.7 Frequency spectrum showing the response of the transducers at a power of 20dBm.

Figure 5.8 The original signal described by the set of X_k complex numbers in the frequency domain.

Figure 5.9 The Fourier transform of the original signal from the frequency domain into the time domain for sample *B3* (see table 5.1).

Figure 5.10 Schematic illustration of reflection-dependent paths.

Table 5.1 The properties of the samples used to determine the velocity dependence upon porosity *V(p)*.

Figure 5.11 Measured longitudinal velocity dependence on porosity for p++ pSi in the [100] crystallographic direction (circles) with theoretical fit and comparison to p+ pSi.

Figure 5.12 (Left) Sample measurement of Bragg mirror sample #1 showing three stopbands without normalisation to the transducer response which is also shown and (Right) normalised sample measurement showing the first three stopband modes.

Figure 5.13 Dissolution of four pSi single layers in NaOH solution placed in an ultrasonic bath at 29 °C (filled circles) and at 34 °C (unfilled circle).

Figure 5.14 AFM contact mode height scans for the (a) pSi - cSi surface (10 μm x 10 μm) and (b) the back-side surface of a p++ Si wafer (75 μm x 75 μm).

Figure 5.15 Height histograms for the three scan areas for the pSi - cSi surface of p++[100] pSi sample after removal of a 73 μm porous layer (sample *D*).

Table 5.2 Surface roughness (rms) values for each porous layer removed.

Figure 5.16 Gaussian Height distributions of the pSi - cSi interface for samples of varying thicknesses.

Figure 5.17 Height histogram for the back-side of a p++[100] Si wafer.

Figure 5.18 Optical stopband seen from a pSi Bragg mirror, sample #9.

Figure 5.19 Optical spectra for Bragg mirror sample # 1, showing high order modes in the visible region for M=16 at 512nm and other orders at 545nm, 584nm, 629nm, 694nm and 735nm.

Figure 5.20 Optical response of a pSi rugate filter.

Figure 6.1 The block diagram used for the transfer matrix method of modelling.

Figure 6.2 Modelling the rugate filter using the TMM.

Figure 6.3 Porosity profile of the rugate filter modelled in steps using the TMM.

Figure 6.4 Simulation of transmission through pSi acoustic rugate filter with stepped porosity profile shown in inset with p_{high}=0.55 p_{low}=0.47, half-cycle thicknesses of d_1=1.31 μm d_2=1.44 μm and N=15 repeats based on smoothing a quarter-wave Bragg mirror.

Table 6.1 Symmetry (τ_1/τ_2) of the Bragg mirror for each value of Γ chosen.

Figure 6.5 Examples of some of the transmission specta of the Bragg multi-layers shown for D=140nm with (left) Γ= 0.3 and (right) Γ= 0.5.

Figure 6.6 Dependence of the stop-band widths on Γ for the case when D=140nm showing the stop-band orders from M=1 to M=5.

Figure 6.7 Interface between the pSi layer and cSi substrate.

Figure 6.8 Porosity profiles for interface roughnesses of σ = 2nm, 6nm, 10nm, 25nm with p_1=0.56, p_2=0.46, d_1=98nm, d_2=42nm (Γ=0.7) and N=35.

Figure 6.9 Reduction in stopband depth and width for rough interfaces for the case when Γ=0.7 without interface roughness (0 nm) and roughness applied to porosity profile (25 nm).

Figure 6.10 Dependence of the first three stopbands on interface roughness for (left) Γ=0.2 and (right) Γ=0.7.

Figure 6.11 The dependence of each stopband depth on interface roughness for (left) Γ=0.2 and (right) 0.7.

Figure 7.1 Transmission spectrum observed from a Bragg mirror sample without enough layers to produce a stopband at 1 GHz, the mirror has 8 pairs of layers.

Figure 7.2 (Top) Effect of the number of layers in a Bragg mirror on the stopband depth and (Bottom) SEMs of the Bragg mirror samples (left) #44, (middle) #45 and (right) #46 with N=5, 10 and 15 pairs of layers respectively.

Figure 7.3 Transmission through pSi Bragg mirrors showing rejection bands centred at (Left) 1.2 GHz and (Right) 0.9 GHz.

Figure 7.4 Transmission through pSi Bragg mirrors that are (Left) balanced showing odd modes M=1 and M=3, and (Right) unbalanced exhibiting four stop bands for both odd and even modes.

Figure 7.5 (Left) Bragg mirror #50 compared with (right) Bragg mirror #51, this mirror has the lowest frequency stopband observed in this investigation.

Figure 7.6 (left) Bragg mirror and (right) rugate filter with fit, with the same AB layer porosities of p_1=0.43 and p_2=0.57.

Figure 7.7 Reduction of higher orders for a rugate filter compared to a Bragg mirror.

Figure 7.8 Optical response of a (left) Bragg mirror and (right) rugate filter in the infrared region of the spectrum.

Figure 7.9 Rugate filter without (top left) and with etch breaks (top right) with simulated fit to experimental data and the direct comparison of the two data (below).

Figure 7.10 PSi acoustic rugate filter exhibiting only the fundamental stopband at 0.95 GHz with bandwidth of 0.2 GHz and stopband depth of 40 dB.

Figure 7.11 A pSi based acoustic microcavity exhibiting a stopband at 1.16 GHz with bandwidth 0.21 GHz, with a central transmission peak in the stopband for Q-factor ~ 90.

Figure 7.12 (Left) PSi based acoustic microcavity with the fundamental mode at 0.93 GHz with 0.4 GHz bandwidth and 50dB rejection with the second order mode located at 1.8 GHz. (Right) PSi acoustic microcavity previously shown in figure 4.12, with a transmission peak located in the centre of the stopband at 0.97 GHz.

Figure 7.13 (Left) PSi acoustic microcavity with the fundamental mode at 1.06 GHz with 0.2 GHz bandwidth at 30 dB rejection. (Right) PSi acoustic microcavity with the fundamental mode at 1.23 GHz with a bandwidth of 0.4 GHz with 40 dB rejection and Q-factor ~ 210.

Figure 7.14 PSi rugate filter without (left) and with (right) an apodisation function of sin(x) from 0 to π including index-matching layers giving clear sidelobe suppression.

Figure 7.15 (Left) Sine apodised pSi acoustic microcavity and (Right) sine apodised pSi Bragg mirror.

Figure 7.16 Double-band optical rugate filter with two periods and the dependence of the electric field measured in different crystallographic directions.

Table 7.1 Etch parameters used for the fabrication of these samples.

Figure 7.17 SEM image of sample 4 where the pSi Bragg mirror is seen on the substrate with the pSi multilayer shown with dark areas indicating high porosity and light areas low porosity.

Figure 7.18 Optical response of sample 4 showing the measured and fitted data.

Figure 7.19 Predicted locations of the band-gaps based on the measured layer thicknesses and porosities deduced from optical response data for sample 3.

Figure 7.20 Pump-probe experimental set-up to measure the response of the pSi multilayers.

Figure 7.21 The pump-probe spectra measured for samples 2 (left) and 4 (right).

Figure 7.22 The pump-probe spectra measured for sample 3 for different areas on the surface of the pSi multilayer for (left) 2 GHz and (right) 5 GHz resolutions.

Figure 8.1 Multiple Reflections within each of the sample layers.

Table 8.1 Additional samples used for the loss measurements.

Figure 8.2 Fourier transform peak amplitudes from a single-layered pSi sample with peaks corresponding to sets of reflections within the pSi layer and cSi substrate region.

Figure 8.3 Attenuation as a function of porosity for p++ pSi for measurements in the [100] crystallographic direction at a frequency of 1GHz.

Figure 8.4 Reflection peaks in the porous layer on a logarithmic intensity scale against round trips.

Figure 8.5 Attenuation coefficient for longitudinal acoustic waves through one micron of porous material as a function of porosity, for p++ pSi with measurements in the [100] crystallographic direction.

Figure 8.6 Comparison between the c_{11} elastic constant found empirically for p+ (dashed line), and p++ (solid line) pSi based upon longitudinal velocity measurements (circles).

Figure 8.7 Porosity and directional dependence of Young's Modulus E_{ijk} for p+ pSi.

Figure 8.8 (Left) Cubic pore, (middle) cross-shaped pore and (right) spherical pore.

Figure 8.9 Effect of pore geometry on Young's modulus for pSi using $E_{cSi[100]}$ = 130GPa.

List of Abbreviations and Symbols

Chapter 1

pSi	Porous Silicon
cSi	Crystalline Silicon
EMA	Effective Medium Approximation
BAW	Bulk Acoustic Wave
SAW	Surface Acoustic Wave
FBAR	Film Bulk Acoustic Resonator
SMR	Solidly Mounted Resonator
CVD	Chemical Vapour Deposition
MBE	Molecular Beam Epitaxy

Chapter 2

p++	Heavily Doped with Boron
σ	Tensile Stess
ε	Tensile Strain
c	Elastic Stiffness
s	Elastic Compliance
P	Simple Cubic
I	Body Centred Cubic
F	Face Centred Cubic
E	Young's Modulus
a	Lattice Constant
K	Bulk Modulus
A	Anisotropy Factor
k	Wave Vector
ω	Angular Frequency
V_p	Phase Velocity
ρ	Material Density
V_L	Longitudinal Wave Velocity
V_T	Shear Wave Velocity

Chapter 3

MOCVD	Metal Organic Chemical Vapour Deposition
Z	Acoustic Impedance
v_x	Particle Velocity
T	Traction Force
r_v	Particle Velocity Reflection Coefficient
t_v	Particle Velocity Transmission Coefficient
r_T	Stress Reflection Coefficient
t_T	Stress Transmission Coefficient
R	Reflectance
T	Transmittance
n	Refractive Index
d	Layer Thickness
N	Number of Bi-layers
M	Mode Number
λ_B	Optical Bragg Wavelength
$\Delta\lambda$	Bandwidth of Optical Stopband
R_B	Reflectance of Stopband
f	Frequency
T_B	Transmittance of Stopband
f_B	Frequency of Acoustic Stopband
Δf	Bandwidth of Acoustic Stopband
f_B	Bragg Frequency
ρ_0	Density of Silicon
p	Porosity
V_0	Longitudinal Wave Velocity through Silicon
k	Empircal Exponent Constant
Z_{pSi}	Acoustic Impedance of Porous Silicon
Z_{cSi}	Acoustic Impedance of Crystalline Silicon
dZ	Impedance Mismatch
k	Wavevector
τ	Time of Flight
ΔZ	Impedance Mismatch

Chapter 4

CZ	Czochralski Crystal Growth
SEM	Scanning Electron Microscope
SSP	Single Side Polished
DSP	Double Side Polished
AFM	Atomic Force Microscope
p-	Lightly Doped with Boron
p+	Moderately Doped with Boron
J_c	Current Density
I	Current
A	Surface Area

Chapter 5

CCD	Charge-Coupled Device
VNA	Vector Network Analyser
ARC	Anti-reflection Coating
rms	Root Mean Square Value
m	mass
V	Volume
D	Diameter
Δl	Path Delay
δ	Phase Difference
n_0	Refractive Index of Air
λ_c	Constructive Interference
λ_d	Destructive Interference
ε	Dielectric Constant
k_{ex}	Extinction Coefficient
α	Absorption Coefficient
f_i	Volume Filling Fraction
ε_{eff}	Effective Dielectric Constant
ε_{air}	Dielectric Constant of Air
n_{eff}	Effective Refractive Index

S_{21}	Scattering Parameter
Δf	Frequency Span
Z_i	Height Deviation

Chapter 6

TMM	Transfer Matrix Method
H-S	Herzberger-Salzberg
UV	Ultraviolet
$\underline{\underline{M}}$	Characteristic Matrix
β	Phase Thickness
η_0	Optical Admittance of Incident Medium
η_s	Optical Admittance of Substrate Material
γ	Physical Thickness
Y	Optical Admittance of the Stack
n(E)	Real Part of Refractive Index
k(E)	Imaginary Part of Refractive Index
E	Photon Energy
Λ	Period or Pitch
D	Total Thickness of Multi-layered Stack
σ	Interface Roughness

Chapter 8

GMC	Generalised Method of Cells
MSA	Minimum Solid Area
α_T	Thermal Conductivity
α_V	Viscous Damping
α	Attenuation
F	Applied Force
k	Spring Constant
x	Displacement
ε	Tensile Strain
σ	Tensile Stress

η	Viscosity
$\underline{u}$	Particle Displacement
β	Attenuation in Porous Silicon
α	Attenuation in Crystalline Silicon
μ	Poisson Ratio
G	Shear Modulus
ϕ	Volume Fraction
f	Porosity Factor
E	Young's Modulus
k	Exponent Constant

Publications Related to this Thesis

Thomas et al, 'Hypersonic Rugate Filters Based On Porous Silicon', paper published in Applied Physics Letters, **97**, 173503 (2010)

Porous Semiconductors - Science and Technology (PSST) Conference, Valencia, March 2010 – (O15-O5) Oral Presentation: 'Porous Silicon Rugate Filters for Hypersonic Applications', Thomas, Snow.

Materials Research Society Conference, Boston, December 2009 – (CC8.6) Oral Presentation: 'Hypesonic Rugate Filters Using Spatially Modulated Nanoporous Silicon', Thomas, Aliev, Snow.

NanoSmat Conference, Rome, October 2009 – (NS143) Oral Presentation: 'Multilayered Acoustic Devices Using Spatially Modulated Nanoporous Silicon', Thomas, Aliev, Snow.

Abstract

Acoustic filters for signal filtering are used in wireless technologies operating at gigahertz frequencies for communication systems such as next generation cell phones. Multilayered porous silicon structures have been fabricated from silicon wafers to create the Bragg mirror section of a bulk acoustic wave filter. These porous silicon multilayers have been designed for use from 500 MHz – 20 GHz with primary focus on frequencies at 1 GHz.

The porous silicon multilayers consist of alternating layers of high and low acoustic impedance layers on a bulk silicon substrate. They are fabricated using electrochemical etching where the current density during the etch determines the porosity and hence acoustic impedance of each layer. Bragg mirrors, Fabry-Perot filters, microcavities and rugate filters can be produced in this way due to the control of the tuneable porosity profile throughout the structure. The porosity of the layer modifies the elastic constants of the layer such as the Young's modulus and hence the velocity of the bulk acoustic waves travelling through it. The behaviour of bulk acoustic waves through silicon is known but in order to fabricate porous silicon acoustic filters, the dependence of the longitudinal wave velocity as a function of porosity must also be known. This has been studied using acoustic transmission measurements on single porous silicon layers and then extended to multilayered structures.

Rugate filters are single frequency filters that have not previously been studied for acoustic applications. In this study the first acoustic rugate filters have been fabricated using porous silicon material that exhibit only one stop-band near 1 GHz. Bragg mirrors have been made with acoustic transmission measurements showing the locations of the stopbands. Porous silicon microcavities have also been fabricated along with filters that have apodisation functions.

This work could form the basis of future efforts to produce and incorporate all-Si multilayers into acoustic filters that are easily fabricated at a high level of quality and reliability that will serve to be efficient and cost effective.

1 Introduction

1.1 Porous Silicon

Porous silicon (pSi) is a form of silicon (Si) which can be produced using anodic electrochemical etching of doped bulk silicon wafers to create pSi films on bulk crystalline silicon (cSi) substrates.[1] PSi material has been studied extensively for two decades following the observation of its efficient room temperature luminescence in 1990[2] demonstrating the interest in this material due to the utility and adaptability of pSi as a functional material.[3] The porosity is defined as the ratio of the void volume to the total volume of the Si film. Si is a versatile material chosen for use in this investigation due to its well defined properties, inexpensive availability and most importantly for the ability to make it porous in nature. Silicon is the second most abundant element in the Earth's crust after oxygen and naturally occurs as silicon dioxide and silicates. For example, around a fifth of the Earth's surface is covered by desert and a large part of this is sand (or silicates). Silicon is mainly used in the semiconductor industry and makes up the principal material used for computer components such as transistors, integrated circuits and chips. PSi has mainly found uses in optical devices and only fairly recently has research been done to investigate its elastic properties for incorporation into acoustic devices. [4, 5]

PSi has a very large surface area relative to its volume and has different optical and acoustic properties compared to Si. The shapes and sizes of the pores can be very different depending on the initial conditions of the bulk Si wafer from which pSi is made. PSi consists of regions void of material, known as pores that are connected via thin strands and bridges of cSi. Si is an anisotropic material giving even more dimensions for the control of pSi structures and morphologies. Given the huge choice of parameters that give control over porosity, depth and morphology of pSi this material is highly tuneable. However, since acoustic properties depend on material structure it is necessary to study these before any acoustic devices can be made using a multilayered pSi system. Using existing literature for data on the acoustic properties of pSi, a theoretical study of the acoustic characteristics of pSi Bragg mirrors and

rugate filters has previously been done.[6] However, specific knowledge of the elastic properties of pSi with different doping levels and morphologies has not been extensively studied and the behaviour of longitudinal acoustic waves in pSi is not well characterised.[7]

The fabricated multilayered pSi structures have been characterised by means of optical interferometer measurements that give the porosity of each porous layer when combined with an effective medium approximation (EMA) model.[8] The fabricated structures have known physical properties and are studied using acoustic transmission spectroscopy whereby longitudinal acoustic waves are generated using a pair of ultrasonic transducers. The longitudinal waves are coupled into the fabricated structures through a coupling liquid and the response of the pSi multilayers to acoustic waves is studied by looking at the transmission of acoustic waves through the structures. Acoustic studies have been performed on a series of multilayers with varying initial parameters such as different porosities and layer thickness. Multilayered pSi is used to create stopbands since the combination of layers can be made to represent a good reflector of longitudinal acoustic waves. The samples have been tailored to produce specific desired acoustic properties such as stopband width and location in the frequency domain.

1.2 Applications of Multilayers

Applications of this work include wireless technologies. Work on wireless technology started as early as 1880 and later Marconi and Braun were awarded the Nobel Physics Prize for their contributions to wireless technology in 1909. Since then enormous amounts of resources and time have been invested in improving wireless technology. Today semiconductor components are used for wireless devices such as remote controls, GPS systems, wireless internet connections such as Wi-Fi, mobile phone and telecommunications. Wireless communications span the spectrum from 9 kHz to 300 GHz and acoustic filters are needed for signal processing. These can be used to filter out background noise in a system or to remove interfering frequencies. Filters can be electronically based using capacitors, inductors and resistors to create bandpass filters that only allow a set bandwidth of frequencies. The filters investigated in this thesis

are related to bulk acoustic wave (BAW) devices that rely on the propagation of acoustic waves from a piezoelectric material and waves are coupled into a multilayered mirror section.

The most well-known piezoelectric material is quartz which is a crystalline material, also known as silicon dioxide (SiO_2). When a mechanical force is applied to a piezoelectric material an electrical charge gives rise to a potential difference across the material due to the separation of atomic charges within the material. This potential difference or voltage will be proportional to the stress applied to the material and is useful for transducers where an applied voltage leads to mechanical action that generates mechanical waves that can be coupled into a material. Transducers are used to excite BAW and surface acoustic waves (SAW) incorporated into devices designed for use at different frequencies depending on the application and include resonators and filters for signal processing. Some filter examples include high-pass, low-pass, bandpass and notch filters and these can have bandwidths of up to 4.5% of the operating frequency.[9] The acoustic filters designed in this investigation are heavily based on notch filters that cut a small region of frequencies without affecting the majority of other frequencies that are allowed to pass. The acoustic filters in this investigation are based on pSi and have been shown to exhibit stopbands of up to 40% of the operating frequency.

Thin film resonators for military and commercial wireless applications use Film Bulk Acoustic Resonators (FBAR) and Solidly Mounted Resonators (SMR) as shown in figure 1.1 that operate from 500 MHz to 20 GHz. FBARs can be found as RF filters in mobile phones to remove unwanted frequencies and in duplexers, where the transmitter and receiver are isolated and share a common antenna. FBARs are beginning to replace SAW devices due to their smaller size and improvements in the maximum operating frequencies. They operate in the same way as SMRs having a piezoelectric region sandwiched between two electrodes where longitudinal waves are excited into a reflector region. The piezoelectric material is usually aluminium nitride (AlN) or zinc oxide (ZnO). These types of device are less prone to surface contamination compared to SAW devices but are more difficult to manufacture.[10]

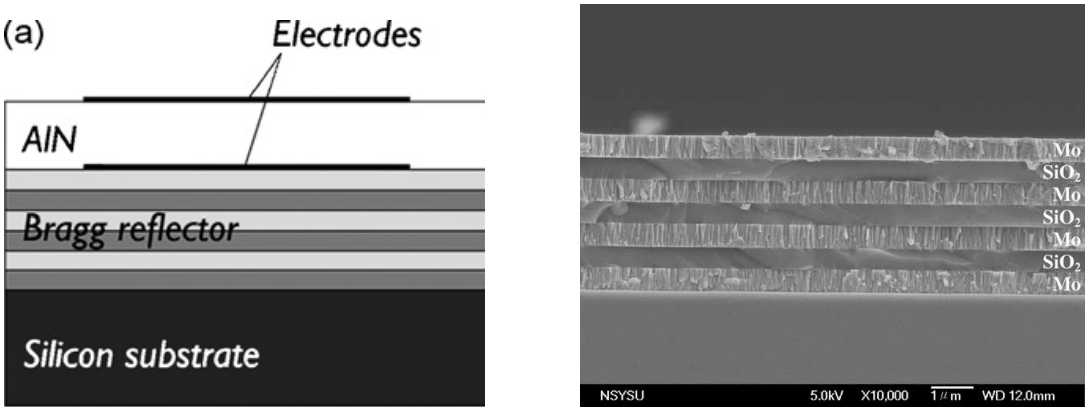

Figure 1.1 (Left) Conventional SMR with two electrodes.[11] (Right) Cross-sectional SEM image of a seven-layer Mo/SiO_2 Bragg reflector for use at 2.5 GHz.[12]

SMRs consist of a piezoelectric layer sandwiched between two electrodes which is fabricated directly onto the substrate material and a Bragg mirror is used to isolate the SMR from the substrate i.e. a reflector stack isolates the resonator acoustic fields from the substrate. The reflector stacks used in SMRs are essentially BAW devices that are based on a multilayered structure. The reflector stack/Bragg mirror consists of layers of high and low acoustic impedance where high impedance layers are typically made from tungsten (W) or molybdenum (Mo) and low impedance layers from SiO_2. These layers are thin films <100nm to micron thickness depending on the application. Generally, the higher the frequency that is needed the thinner the layers will be. For example, this work is focused on the development of the reflector stack from all silicon material and layers are typically of micron thickness for fundamental frequencies of 1 GHz but for fundamental frequencies at 20 GHz the layers need to be ~ 50 nm in thickness. The porous nature of the layers made from all silicon material give another method to control the central operating frequency of the multilayer since the pores could be filled with liquid to modify the acoustic impedance of the overall structure and hence modify the frequency response.

Current methods of thin film production are based on deposition techniques that are generally chemical or physical based that can build each layer consecutively using the two different impedance materials. Chemical vapour deposition (CVD) exposes the substrate material to a chemical based reaction that creates the desired end product

and physical deposition techniques such as sputtering use a target material to deposit the layers onto the substrate. Other methods of thin film production include molecular beam epitaxy (MBE)[13] which uses both chemical and physical deposition techniques, where a single layer of atoms is deposited at a time and the layer thickness can be controlled within tens of nanometers and more than one material can be used to create a compound.

In general, the more layers that are used, the higher the reflectance of the reflecting stack. However, there will be a limit to the physical number of layers as there are internal stresses/strains at the interfaces within the stack due to a mismatch in the material properties and this can cause layers to become distorted and detach. In addition, the surface roughness is important for device quality and the more pairs of layers used the higher this roughness becomes, leading to lower quality interfaces.[14]

There are differences to be seen between the conventional manufacturing techniques used to create multilayers via deposition and the techniques used for the fabrication of multilayers in this investigation. Whereas for the deposition techniques the reflector is built up in layers from the top of the substrate material, the method used here fabricates the multilayer from the surface of the substrate down into the substrate itself. Fabrication of multilayers from Si have been done using etching techniques that are inexpensive and fast in comparison to deposition techniques. Not much equipment is needed for the fabrication of pSi multilayers.

The materials used in the manufacture of SMR and FBAR resonators and filters have well known physical properties due to their numerous studies and characterisations. Material properties such as the mechanical, acoustic, energy loss mechanisms and thermal properties are well known for materials used in the semiconductor industry. Their crystal structure is also well understood because time has been invested in improving the performance and quality of these devices in addition to reducing their cost of production. Wireless devices designed to operate at higher frequencies ~ 100 GHz are difficult to manufacture because energy losses rapidly increase and become a limiting factor. The continual search for materials that have more suitable properties to expand the uses of existing devices and applications allows for their continual improvement in quality and performance. Si is a versatile material and is a well

known existing semiconductor component. PSi is a much younger material in comparison and although much is known about its optical properties, much less has been invested in researching its acoustic properties. This work has studied the acoustic properties of pSi layers, specifically the BAW propagation of longitudinal waves through pSi material and this information has enabled the production of pSi multilayers suitable for use in wireless applications at 1 GHz. The use of an existing material with recently determined acoustic properties could improve and extend the performance of existing wireless devices.

A brief introduction to pSi has been given in this chapter as well as some applications of existing semiconductor based multilayers. The manufacturing technique used to fabricate the pSi multilayers studied in this thesis is different to the techniques used to fabricate existing multilayered resonators introduced in this chapter. The acoustic responses of multilayer resonators depend on the elastic properties of the material used. The elastic properties of materials will be discussed in the next chapter with emphasis on the material Si.

2 Elastic Properties of Bulk Materials

Crystals are made up of a unit cell repeated in space and the point group of the crystal determines the symmetry of the macroscopic physical properties. These determine the physical behaviour of the crystals in the different crystallographic directions or the crystal anisotropy. The symmetry of the crystal relates to the symmetry of the positions of the atoms making up the unit cell of the crystal. The principal axis (also written as c-axis or z-axis) is the axis with the highest degree of symmetry; a fourfold axis has a higher degree of symmetry than a twofold axis. The point groups of the crystal are made up of each of the groups having a different number of symmetry operations, for example the point group C_3 has three symmetry operations on an atom. In total there are 32 crystallographic point groups which are the crystal classes and each of these will reside within one of the seven crystal systems. These are described in more detail later in this chapter.

Longitudinal and shear waves can be excited within materials. An acoustic wave propagates through a material by particle displacement and consequently stress and strain fields.[15,16] The elastic properties of materials depend upon their structure and this determines their response to acoustic waves and the velocities of different types of waves propagating within the material. For isotropic materials the elastic properties are the same in any arbitrary direction. For anisotropic materials the elastic properties are different depending upon the crystallographic direction chosen and this affects the propagating waves. Models exist within the literature to predict the response of isotropic materials. When an anisotropic material is to be modelled, there are often a set of assumptions that are considered. For example, one type of isotropic material may be embedded within another second type of material, such as for spherical inclusions within a matrix. The combination of isotropic areas within the matrix resembles a form of anisotropy.[17] If the anisotropic behaviour of a material is not adequately taken into account it could lead to inaccurate results. Biot (1956) first developed a theory for the propagation of elastic waves through a fluid-saturated porous medium. Biot's theory for elastic moduli has been used to predict and confirm observations of bulk acoustic waves in porous media.[18] Eshelby's approach considers an 'inclusion' within an infinite homogeneous isoptropic elastic medium that

undergoes a change of shape and size and uses elastic stresses and strains to determine the elastic state of the inclusion and surrounding material.[19, 20] Generally, there are two approaches that different groups within each field of research use to model the response of anisotropic materials. Engineering approaches study the macroscopic properties of the material by directly measuring elastic moduli such as the Young's modulus by techniques such as nano-indentation. Research within the geophysics and seismology community tend to model the behaviour of porous rock such as sandstone by looking at the microstructure of the materials by using elastic constants and pores within a matrix. Some naturally occurring rock is porous in nature and often filled with fluid so these models generally use effective elastic constants to suit the environmental conditions of measurement. The second is the approach taken to model the pSi in this investigation.

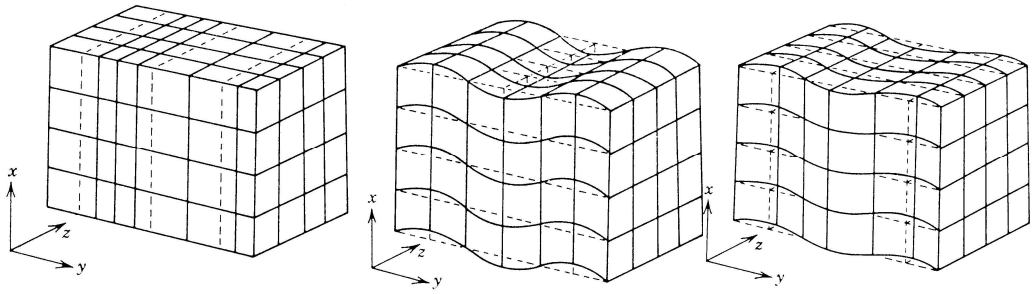

Figure 2.1 Longitudinal, vertical shear and horizontal shear wave examples.

Silicon itself is an anisotropic material and the macroscopic elastic moduli such as the Young's or shear elastic moduli are well known. When pores are introduced into this anisotropic matrix, the new porous material has elastic moduli that are much different to that seen for the non-porous material. Boron-doped wafers are referred to as p-type and for low doping levels are p-, for higher doping p+ and heavily doped wafers p++. The Si wafers used in this investigation are heavily boron doped p++ wafers. The approach used to model the elastic properties of the p++ pSi samples in this study has generally been to look at the propagation of acoustic waves through the new material and relating the effective elastic constants to the macroscopic properties known for bulk Si. Elasticity is a relation between a stress and a strain in a crystal. In general, when a wave travels through a material an inertial and elastic restoring force exerted upon each particle within the material causes the oscillations of the wave as it

propagates throughout the medium.[21] For longitudinal waves this particle motion is parallel to the direction in which the wave is propagating. The elastic restoring forces in the medium can be described by 'microscopic spring forces'[22] for which a relation between the elastic restoring forces and the material deformation with stress σ_{kl} and strain ε_{ij} fields can be made by equation (2.1).

$$\begin{aligned} \varepsilon_{ij} &= s_{ijkl}\sigma_{kl} \\ \sigma_{ij} &= c_{ijkl}\varepsilon_{kl} \end{aligned} \qquad (2.1)$$

The 'microscopic spring constants' are known as the elastic stiffness constant c_{ijkl} and the elastic compliance constant s_{ijkl} where the subscripts are related to directions in the crystal structure. For easily deformed materials the values of c_{ijkl} will be low and for materials that are hard to deform they will have high values, typically expressed in units of Gigapascals (GPa). The crystal property of elasticity is described by the elastic compliance s or elastic stiffness c, where s and c are coefficients that describe a physical property. The elastic stiffness c is the reciprocal of the elastic compliance s and both are described using tensor notation. A fourth-rank tensor relates two second-rank tensors, where a second-rank tensor relates two vectors.[23] In this case, the fourth-rank tensor describing the crystal property of elastic compliance s_{ijkl} relates the two second-rank tensors ε_{ij} and σ_{kl}. The general relation between the s components described above is $s_{ijkl}=s_{jikl}=s_{ijlk}=s_{klij}$ and the same general relation also applies for the c components.[24]

Equation (2.1) is Hooke's law which states that the strain ε_{ij} is linearly proportional to the stress σ_{kl} and vice-versa, this means that if a homogeneous stress is applied to a crystal the result will be a homogeneous strain. Applying a uniform tension to a block of crystal will not only cause it to stretch in the direction of the applied tension but it will also shear so as to deform the original shape of the block. By applying one component of stress σ_{11} to a material then all of the strain components may be non-zero and not just ε_{11} i.e. $\varepsilon_{11}=s_{1111}\sigma_{11}+ s_{1112}\sigma_{12}+ s_{1113}\sigma_{13}+ s_{1121}\sigma_{21}+ s_{1122}\sigma_{22}+ s_{1123}\sigma_{23}+ s_{1131}\sigma_{31}+ s_{1132}\sigma_{32}+ s_{1133}\sigma_{33}$, where there are nine equations that relate stress to strain in a crystal. Therefore there are 81 tensor coefficients c_{ijkl} (or s_{ijkl}) of the stress-strain relation collectively, only 21 of which are independent from one another since

$s_{ijkl}=s_{ijlk}$ and $s_{ijkl}=s_{jikl}$, and similarly for the c_{ijkl} constants. The number of independent tensor coefficients that are needed to describe the elastic properties of a material will depend upon the crystal symmetry of the material of interest as some coefficients become equal to one another due to the symmetry. For example, an isotropic material will have two independent elastic constants c_{1111} and c_{4444} whereas an anisotropic material with tetragonal symmetry will have six independent elastic constants, c_{1111}, c_{1122}, c_{4444}, c_{1133}, c_{3333} and c_{6666}.[22] The symmetry of a crystal is related to the symmetry of its physical properties due to Neumann's Principle: The symmetry elements of any physical property of a crystal must include the symmetry elements of the point group of the crystal.[24] A crystal system will contain elements with the same structure and there are seven crystal systems. These are the triclinic, monoclinic, orthorhombic, tetragonal, trigonal (also known as rhombohedral), hexagonal and cubic crystal systems (figure 2.2). For example, within the cubic system exists elements such as silicon which has a diamond structure, and aluminium which has a face-centred cubic structure. Both silicon and aluminium possess cubic lattices therefore both reside within the same crystal system. Within the cubic system are crystals possessing the simple cubic (P), body-centred cubic (I), face-centred cubic (F) and diamond lattices. With the exception of the diamond lattice, these cubic lattices are referred to as the three cubic Bravais lattices. A lattice is an infinite array of points in which each point has surroundings identical to those of all the other points.[25] For a primitive unit cell there is only one atom as for each corner of the square there is one quarter of an atom contribution per unit which is repeated in space. Cubic Bravais lattices have the highest degree of symmetry of any of the Bravais lattices and it will be shown later that symmetry simplifies the tensors used to describe physical properties of such systems.

For each of the crystal classes the following length scales apply for the sides of the unit cell describing the crystal and the angles between the sides are shown, where the sides a, b and c with the angles α, β and γ are shown on the right of figure 2.2. For Triclinic $a\neq b\neq c$ and $\alpha\neq\beta\neq\gamma$, Monoclinic $a\neq b\neq c$ and $\alpha=\gamma=90°\neq\beta$, Orthorhombic $a\neq b\neq c$ and $\alpha=\beta=\gamma=90°$, Tetragonal $a=b\neq c$ and $\alpha=\beta=\gamma=90°$, Cubic $a=b=c$ and $\alpha=\beta=\gamma=90°$, Hexagonal $a=b\neq c$ and $\alpha=\beta=90°$ with $\gamma=120°$, and finally Trigonal (or rhombohedral) $a=b=c$ and $\alpha=\beta=\gamma\neq90°$.

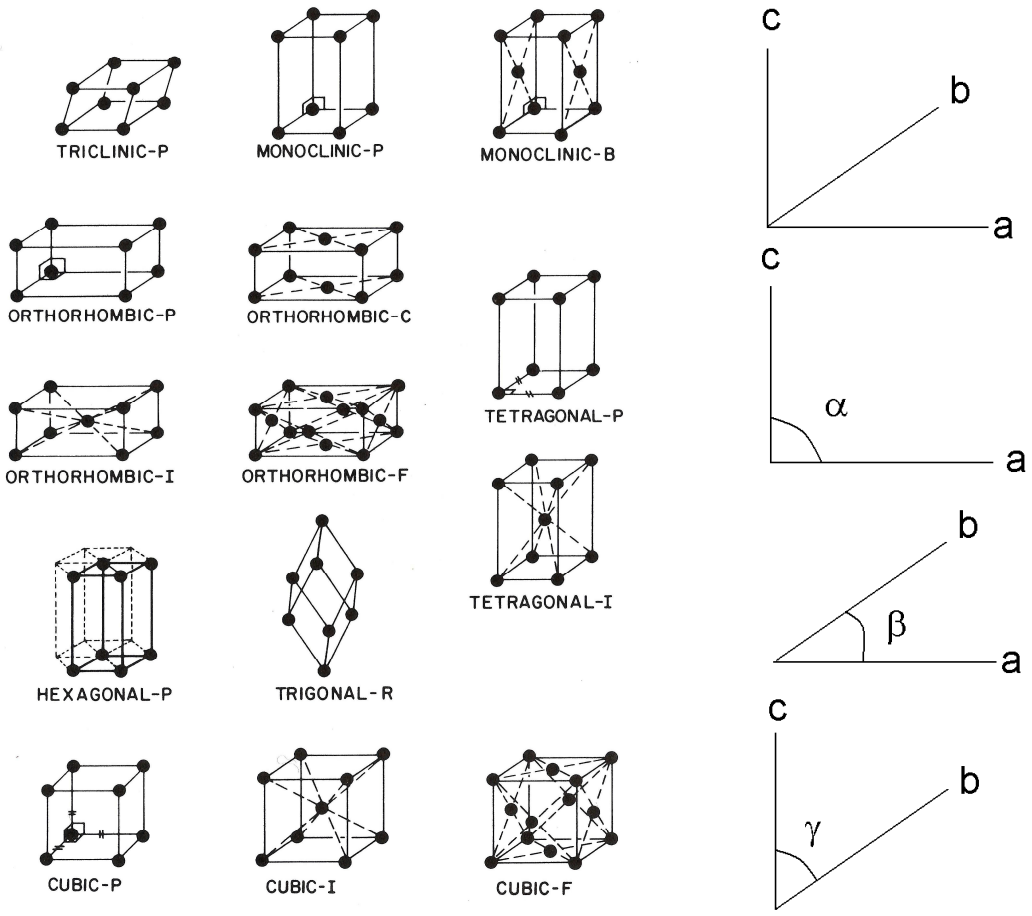

Figure 2.2 The seven crystal systems showing the unit cell for each of the fourteen Bravais lattices.[25]

2.1 Directional Dependence of the Elastic Properties of a Cubic Crystal System

The following will focus on cubic systems because the material in this study is silicon which has a cubic-diamond structure and the initial assumption is that pSi retains this cubic structure since Brillouin scattering on p+ pSi has previously shown that pSi retains the crystalline properties of the parent wafer.[26] In addition to the study of pSi with cubic structure, a description of pSi having a tetragonal structure is given toward the end of this chapter.[27] In particular the physical property of elasticity will be

discussed and in chapter 8 the relation of elasticity to longitudinal acoustic velocity measurements performed on p++ pSi etched from a [100] substrate is discussed.

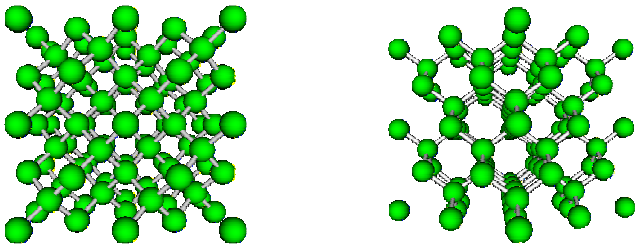

Figure 2.3 Model of a Silicon crystal seen along the [100] (left) and [110] (right) crystallographic directions.

There are 21 independent elastic constants s_{ijkl} that are needed to uniquely determine the elasticity tensor for an anisotropic material and this number of independent constants is reduced depending on the crystal symmetry of the material. For a material with cubic symmetry there are three elastic constants c_{1111}, c_{1122} and c_{4444} that exist that generally describe the elastic properties of a cubic material; two of these elastic constants are independent from each other for the diamond cubic case. Silicon is anisotropic and the elastic properties will differ in each crystallographic direction (figure 2.3).

If the tensor symmetry has the same symmetry as the crystal property that it represents, then the s_{ijkl} constants will possess the same symmetry properties as the c_{ijkl} constants. For a cubic material,

$$\begin{aligned} s_{11} &= s_{1111} = s_{2222} = s_{3333} \\ s_{12} &= s_{1122} = s_{1133} = s_{2233} \\ s_{44} &= 4s_{2323} = 4s_{3131} = 4s_{1212} \end{aligned} \qquad (2.2)$$

The elastic coefficients describe the physical property of elasticity and the suffixes are abbreviated with matrix notation where the elastic compliance constants s_{ijkl} of the compliance tensor has been assigned Voigt's original notation[28] shown in equation (2.3).

$$\varepsilon_i = s_{ij}\sigma_j$$
$$\sigma_i = c_{ij}\varepsilon_j \tag{2.3}$$

The elastic compliance s_{ij} (i, j = 1, 2, 4) for the cubic crystal system is shown by the (6 x 6) elastic compliance matrix in equation (2.4).

$$\begin{pmatrix} \varepsilon_1 \\ \varepsilon_2 \\ \varepsilon_3 \\ \varepsilon_4 \\ \varepsilon_5 \\ \varepsilon_6 \end{pmatrix} = \begin{bmatrix} s_{11} & s_{12} & s_{12} & 0 & 0 & 0 \\ s_{12} & s_{11} & s_{12} & 0 & 0 & 0 \\ s_{12} & s_{12} & s_{11} & 0 & 0 & 0 \\ 0 & 0 & 0 & s_{44} & 0 & 0 \\ 0 & 0 & 0 & 0 & s_{44} & 0 \\ 0 & 0 & 0 & 0 & 0 & s_{44} \end{bmatrix} \begin{pmatrix} \sigma_1 \\ \sigma_2 \\ \sigma_3 \\ \sigma_4 \\ \sigma_5 \\ \sigma_6 \end{pmatrix} \tag{2.4}$$

Young's modulus E is an elastic property of solids and is defined by the ratio of tensile stress σ to tensile strain ε by equation (2.5). The tensile stress is the ratio of the applied force per unit area in equation (2.6) and the tensile strain is the deformation over a unit length described by equation (2.7).

$$E = \frac{\sigma}{\varepsilon} \tag{2.5}$$

$$\sigma = \frac{AppliedForce}{Area} \tag{2.6}$$

$$\varepsilon = \frac{dx}{x} \tag{2.7}$$

The reciprocal of Young's modulus E_{ijk} for a cubic crystal is given by equation (2.8) where s_{ij} are once again the elements of the elastic compliance tensor and l, m and n being the cosine of the angle between the direction of interest and the x, y, z axes i.e. $l=cos(\alpha)$, $m=cos(\beta)$ and $n=cos(\gamma)$ (figure 2.4).

$$\frac{1}{E_{ijk}} = s_{11} - 2\left[(s_{11} - s_{12}) - \frac{1}{2}s_{44}\right]\left(l^2m^2 + m^2n^2 + l^2n^2\right) \tag{2.8}$$

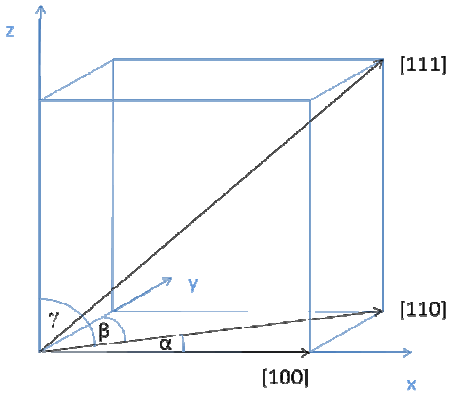

Figure 2.4 Cubic crystal with [100], [110] and [111] directions showing α, β, γ with respect to x, y, z axes shown for the [110] direction only.

Due to the anisotropy of silicon, in the cubic case there is a directional dependence of Young's modulus described by the elastic constants c_{11}, c_{12} and c_{44}. The directional dependence is represented by the $\left(l^2m^2 + m^2n^2 + l^2n^2\right)$ term of equation (2.8) and has zero value for the [100] direction and a maximum value of $\frac{1}{3}$ in the [111] direction. The Young's modulus is therefore greatest in the [111] direction and lowest in the [100] direction. For pure bulk cSi the values of Young's modulus in each crystal direction are E_{100} = 130 GPa, E_{110} = 170 GPa and E_{111} = 185 GPa.[29] Analysis of equation (2.8) leads to the following dependence on the elastic compliance constant describing the directional dependence of Young's modulus in bulk Si.

$$\frac{1}{E_{100}} = s_{11} \tag{2.8a}$$

$$\frac{1}{E_{110}} = s_{11} - \frac{1}{2}\left[\left(s_{11} - s_{12}\right) - \frac{1}{2}s_{44}\right] \tag{2.8b}$$

$$\frac{1}{E_{111}} = s_{11} - \frac{2}{3}\left[\left(s_{11} - s_{12}\right) - \frac{1}{2}s_{44}\right] \tag{2.8c}$$

For cubic materials a relationship exists between the elastic compliance and elastic stiffness constants,[22] and these are as follows in equations (2.9 - 2.11).

$$s_{11} = \frac{c_{11} + c_{12}}{(c_{11} - c_{12})(c_{11} + 2c_{12})} \tag{2.9}$$

$$s_{12} = \frac{-c_{12}}{(c_{11} - c_{12})(c_{11} + 2c_{12})} \tag{2.10}$$

$$s_{44} = \frac{1}{c_{44}} \tag{2.11}$$

For an anisotropic material with cubic symmetry such as Si (or for another crystal with cubic symmetry) it is possible to express the directional dependence of Young's modulus in terms of the elastic stiffness constants c_{11}, c_{12} and c_{44}. For Si the values of the elastic stiffness constants are c_{11} = 166 GPa, c_{12} = 64 GPa and c_{44} = 79 GPa.[30]

For materials with the cubic-diamond structure there are two independent elastic stiffness constants in the relationship shown in equations (2.12 – 2.14), experimental data supports this theory. This relationship is given by Keating where an expression for energy density is derived based on microscopic force constants that is then compared to a well-known macroscopic expression for energy density in a cubic system.[30] The derivation considers force constants from nearest-neighbour α and second-neighbour β interactions where the force on an atom is calculated using force constants and atomic displacement. The lattice constant is given by a. Strain gradients are used to describe the atomic displacements giving a strain energy that only depends on the positions of the nuclei. The relationship between the elastic coefficients and force constants are shown by equations (2.12 – 2.14) and are found comparing the derived energy density to a macroscopic expression.

$$c_{11} = \frac{(\alpha + 3\beta)}{4a} \tag{2.12}$$

$$c_{12} = \frac{(\alpha - \beta)}{4a} \tag{2.13}$$

$$c_{44} = \frac{\alpha\beta}{a(\alpha + \beta)} \tag{2.14}$$

The combination of these expressions lead to the following relationship of equation (2.15) between the elastic coefficients for a cubic system.

$$c_{44} = \frac{(c_{11} - c_{12})(c_{11} + 3c_{12})}{2(c_{11} + c_{12})} \tag{2.15}$$

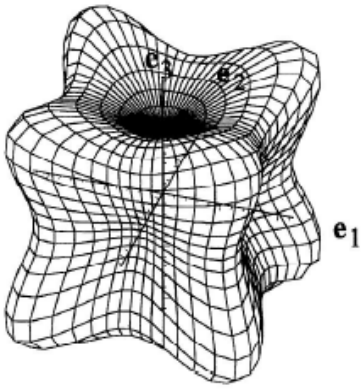

Figure 2.5 Young's modulus of gold (cubic symmetry) where c_{11}=185.0GPa, c_{12}=158.0GPa and c_{44}=39.7GPa.[31]

Figure 2.5 shows the Young's modulus of gold which, like Si, is an anisotropic material with cubic symmetry.[31] The anisotropic linear elastic behaviour of single crystals using a fourth-order elasticity tensor has been modelled by separation into two functions *E(d)* and *K(d)* where these functions represent the Young's modulus

and bulk modulus as functions of the tensile direction *d*. The moduli are separated into isotropic and anisotropic regions that together make up the 21 independent elastic constants needed to define the elasticity tensor for an anisotropic material. The graphical representation of Young's modulus for bulk silicon will be similar to that shown (figure 2.4) for gold. As described by equation (2.8) it is seen that the maximum Young's modulus is found along the [111] crystallographic direction and the minimum Young's modulus is found in the [100] direction; this is highlighted in figure 2.5.

2.1.1 Directional Dependence of Wave Velocity

Waves propagating in any material form a wave-front whose shape depends on the material's properties. The characteristics of the ultrasonic waves will depend upon the mechanical structure and elastic moduli of the medium through which they propagate. In a uniform isotropic medium the waves propagate with the same velocity in all directions (figure 2.6) whereas in an anisotropic material, such as cubic silicon, the wave-front is distorted as the wave propagates at different velocities in different directions through the material (figures 2.7 and 2.8). The wave velocities in each direction of the anisotropic material will be influenced by the degree of anisotropy, or the anisotropic factor *A* which for cubic crystal classes is defined by equation (2.16), for Si the anisotropy factor is A = 1.55.

$$A = \frac{2c_{44}}{c_{11} - c_{12}} \tag{2.16}$$

The simplest case of propagation is along a crystal axis as there will only be a pure longitudinal and shear wave solution. The case highlighted in figure 2.7 shows the propagation through a cube face where there are pure shear, quasi-shear and quasi-longitudinal wave solutions. For propagation in the XZ plane as shown the particle velocity is normal to the XZ plane and gives the pure shear wave solution. The other wave solutions simplify for certain directions such as along the [100] direction. The propagation characteristics of plane waves in an anisotropic solid can be described

using the Christoffel equation that defines a surface in *k*-space that describes the wave vector *k* as a function of direction.[22] The wave vector *k* is always proportional to the angular frequency ω and a 'slowness surface' (which is the inverse of velocity) can be considered where the inverse of the phase velocity V_p is shown in equation (2.17) and is a function of propagation direction. This description is more convenient because a wave vector surface would otherwise scale with ω and the important physical properties such as the velocity of elastic waves in each direction can be described by the slowness surface for isotropic and anisotropic materials that depend upon the crystal properties of the material, such as density ρ.

$$\frac{1}{V_p} = \frac{k}{\omega} \tag{2.17}$$

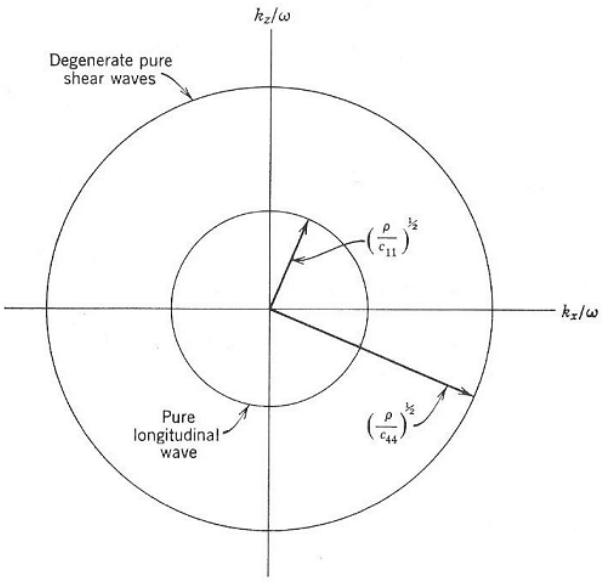

Figure 2.6 Slowness surface for an isotropic solid for propagation in an arbitrary plane.[22]

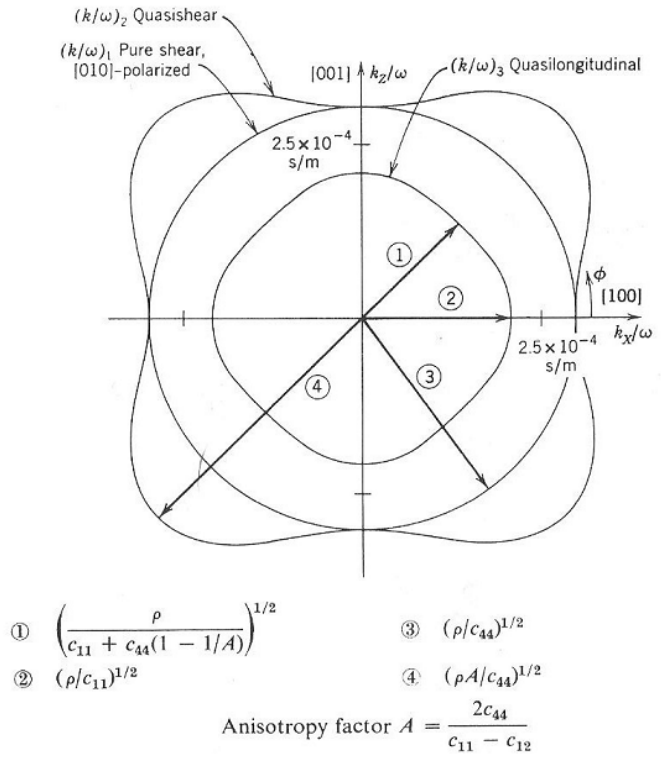

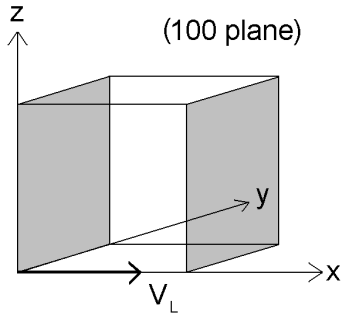

Figure 2.7 (Above) Slowness surface for an anisotropic solid with cubic symmetry for propagation in a cube face (GaAs)[22] and (Below) longitudinal velocity V_L shown for travel in the [100] direction along the x-axis for wave propagation through (100) plane.

Using the slowness surface shown in figure 2.7 and the elastic constant dependence for other crystal directions, the longitudinal and transverse velocities in each crystallographic direction of interest for Si have been summarised in table 2.1 where the square velocities relate to the quasi-longitudinal wave V_L^2, the quasi-shear wave V_{T1}^2 and the pure shear wave polarised in the $[1\bar{1}0]$ direction V_{TL}^2. It can be observed that for different directions there are different combinations of the elastic constants

describing the velocities and the simplest case is for the [100] direction which only depends on one of these elastic constants c_{11} for the longitudinal velocity. The material density is given by ρ.

Direction	V_L^2	$V_{T_\parallel}^2$	$V_{T_\perp}^2$
100	$\frac{c_{11}}{\rho}$	$\frac{c_{44}}{\rho}$	$\frac{c_{44}}{\rho}$
110	$\frac{c_{11}+c_{12}+2c_{44}}{2\rho}$	$\frac{c_{44}}{\rho}$	$\frac{c_{11}-c_{12}}{2\rho}$
111	$\frac{c_{11}+2c_{12}+4c_{44}}{3\rho}$	$\frac{c_{11}-c_{12}+c_{44}}{3\rho}$	$\frac{c_{11}-c_{12}+c_{44}}{3\rho}$

Table 2.1 Acoustic velocities through Si in each crystallographic direction.

2.2 Elastic Properties of a Tetragonal Crystal System

For the velocity measurements performed on the pSi samples presented in this thesis, the acoustic transmission measurements have been done along the [100] direction for wave propagation in the (100) plane or in the cube face such as the longitudinal velocity described in figure 2.7. However, since there is some possibility that pSi material has weak tetragonal symmetry a brief description is given here of tetragonal crystal systems. It is worth noting that despite the cubic or tetragonal symmetry of the pSi material, the longitudinal wave velocity in the [100] direction of interest does not change and will depend only upon the c_{11} elastic constant. It is only when other wave propagation directions are considered that the crystal symmetry becomes important.

For a crystal with tetragonal symmetry there will be six elastic constants that together describe the elastic properties of the crystal. Three of these constants are the same as those used to describe the cubic crystal system s_{11}, s_{12} and s_{44} but there are also three new constants s_{13}, s_{33} and s_{66}. There are more constants needed to describe a tetragonal system than the cubic system because there is less symmetry in the crystal and the sides of the unit cell a = b ≠ c. The tetragonal crystal can be described as a cubic crystal with an extension δ to the length of the cube sides in one direction so

that for the elastic constants $s_{13} = (s_{12} + \delta s_{12})$, $s_{33} = (s_{11} + \delta s_{11})$ and $s_{66} = (s_{44} + \delta s_{44})$. The elastic compliance matrix is given below in equation (2.18).

$$\begin{pmatrix} \varepsilon_1 \\ \varepsilon_2 \\ \varepsilon_3 \\ \varepsilon_4 \\ \varepsilon_5 \\ \varepsilon_6 \end{pmatrix} = \begin{bmatrix} s_{11} & s_{12} & s_{13} & 0 & 0 & 0 \\ s_{12} & s_{11} & s_{13} & 0 & 0 & 0 \\ s_{13} & s_{13} & s_{33} & 0 & 0 & 0 \\ 0 & 0 & 0 & s_{44} & 0 & 0 \\ 0 & 0 & 0 & 0 & s_{44} & 0 \\ 0 & 0 & 0 & 0 & 0 & s_{66} \end{bmatrix} \begin{pmatrix} \sigma_1 \\ \sigma_2 \\ \sigma_3 \\ \sigma_4 \\ \sigma_5 \\ \sigma_6 \end{pmatrix} \tag{2.18}$$

Since the multilayered pSi may have a weak tetragonal symmetry this is briefly described in this section, however pSi has been treated with cubic symmetry throughout the rest of this investigation. The tetragonal elastic constants are as follows in equations (2.19 – 2.24).

$$c_{11} + c_{12} = \frac{s_{33}}{s} \tag{2.19}$$

$$c_{11} - c_{12} = \frac{1}{s_{11} - s_{12}} \tag{2.20}$$

$$c_{13} = -\frac{s_{13}}{s} \tag{2.21}$$

$$c_{33} = \frac{s_{11} + s_{12}}{s} \tag{2.22}$$

$$c_{44} = \frac{1}{s_{44}} \tag{2.23}$$

$$c_{66} = \frac{1}{s_{66}} \tag{2.24}$$

where $s = s_{33}(s_{11} + s_{12}) - 2s_{13}^2$.

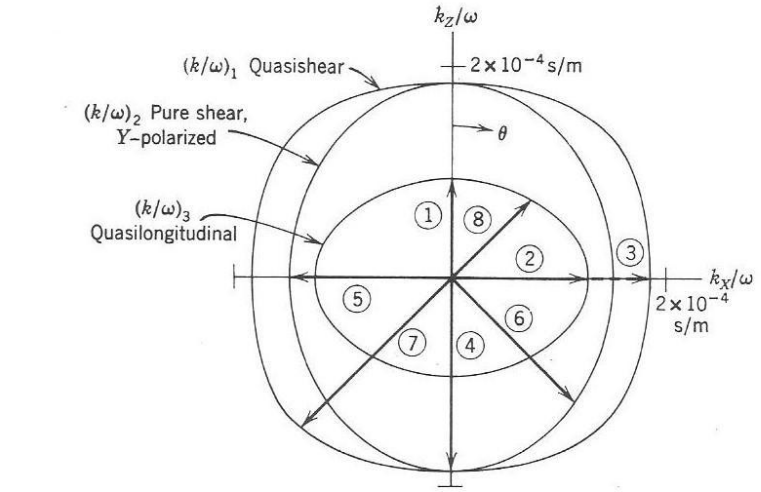

① $(\rho/c_{33})^{1/2}$

② $(\rho/c_{11})^{1/2}$

③④ $(\rho/c_{44})^{1/2}$

⑤ $(\rho/c_{66})^{1/2}$

⑥ $\left(\dfrac{2\rho}{c_{66}+c_{44}}\right)^{1/2}$

⑦ $\dfrac{(4\rho)^{1/2}}{\left\{c_{11}+c_{33}+2c_{44}-\sqrt{(c_{11}-c_{33})^2+4(c_{13}+c_{44})^2}\right\}^{1/2}}$

⑧ $\dfrac{(4\rho)^{1/2}}{\left\{c_{11}+c_{33}+2c_{44}+\sqrt{(c_{11}-c_{33})^2+4(c_{13}+c_{44})^2}\right\}^{1/2}}$

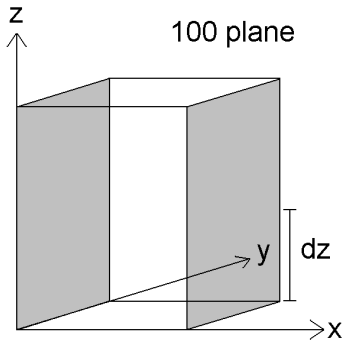

Figure 2.8 Slowness surface for an anisotropic solid with tetragonal symmetry for propagation in a 'cube' face (rutile).[22]

This chapter has discussed some of the elastic properties that a material possesses and how anisotropy affects the way that waves propagate through the material in different crystallographic directions. Si has cubic symmetry and the elastic stiffness constants describe the behaviour of the material for each crystallographic direction. PSi has been assumed to possess the same cubic symmetry of the parent Si wafer, however, tetragonal symmetry has briefly been introduced as pSi may possess weak tetragonal symmetry. For acoustic studies using longitudinal waves in the [100] direction modelling the pSi with cubic symmetry is the same as with tetragonal symmetry because only the c_{11} elastic stiffness constant is relevant. The acoustic impedance of the Si and pSi materials will depend on the elastic properties and will be discussed in the next chapter. It is important to understand the acoustic impedance dependence of pSi material because multilayered stacks based on pSi will be fabricated for acoustic filtering. The pSi filters can be designed to have desired acoustic responses and control of the acoustic impedance through the pSi multilayers is needed.

3. Properties of Multilayered Structures

Elastic waves travelling through any material will be modified depending on the structure of the material. Non-porous materials undergo deformation when a force is applied so that the material will yield slightly unless the material is perfectly rigid. Porous materials allow air to penetrate below their surface which modifies the effective motion of the material when under stress or strain. The reaction of the material can be expressed in terms of a specific acoustic impedance which generally depends upon the nature of the material, and on the frequency and angle of the incident waves. For acoustic waves travelling through a material the acoustic impedance, Z depends on the material density, ρ and the particle (or wave) phase velocity which itself is related to the elastic constant of the material c.

When a propagating acoustic wave encounters an interface with an impedance mismatch, a proportion of the wave is reflected and a proportion transmitted through the boundary. Depending on the surface roughness of the interface there is also a proportion of the wave that is scattered. Assuming that each plane interface is smooth for a perfect material without defects or attenuation, there will only be an impedance mismatch existing between each boundary. The amplitude of the reflected and transmitted wave depends upon the impedance ratio between the two media either side of the boundary.

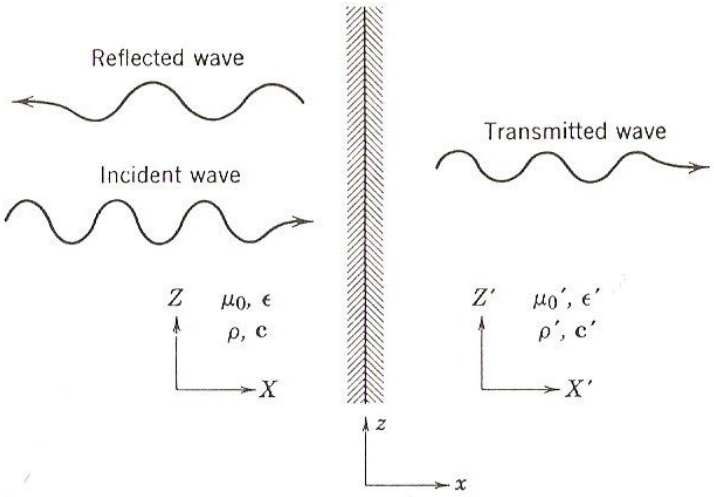

Figure 3.1 Reflection of a normally incident wave at a plane boundary.[32]

There are a few boundary conditions that need to be applied between regions with different material properties (figure 3.1). For acoustic fields across discontinuities it is assumed that the interfaces between different solid media are firmly bonded together

(such as for the pSi-cSi interface discussed later), so that the particle displacement velocity, v_x will be continuous across the interface. Motion of the boundary itself is ignored such that $v_x(0) = v_x'(0)$. There will be a traction force, T_x across the boundary at $x=0$ that must be continuous[32] such that $T_x(0) = T_x'(0)$. It will be assumed that the pSi layer and the cSi substrate both have an interface which is always normal to the [100] crystallographic direction. If a uniform plane wave is incident on the plane pSi surface then at least one reflected and transmitted wave will be detected. For a longitudinal wave propagating in the positive x-direction incident I upon the plane boundary (figure 3.1) the particle displacement velocity $(v_x)_I$ and the traction force $(T_x)_I$ at the boundary are given by equations (3.1) and (3.2) respectively where t is time. The specific impedance $(\rho c_{11})^{1/2}$ describes the ratio of the traction force to the particle displacement velocity.

$$(v_x)_I = Ae^{i(\omega t - kx)} \tag{3.1}$$

$$(T_x)_I = -(\rho c_{11})^{1/2} Ae^{i(\omega t - kx)} \tag{3.2}$$

Similarly, for the reflected R and transmitted T waves,

$$(v_x)_R = Be^{i(\omega t + kx)} \tag{3.3}$$

$$(T_x)_R = (\rho c_{11})^{1/2} Be^{i(\omega t + kx)} \tag{3.4}$$

$$(v_x')_T = B'e^{i(\omega t - k'x)} \tag{3.5}$$

$$(T_x')_T = -(\rho' c_{11}')^{1/2} B'e^{i(\omega t - k'x)} \tag{3.6}$$

Applying the boundary conditions,

$$v_x(0)_I + v_x(0)_R = v_x'(0)_T \tag{3.7}$$

$$T_x(0)_I + T_x(0)_R = T_x'(0)_T \tag{3.8}$$

and substituting for the particle velocity and traction force gives the simultaneous equations,

$$A + B = B' \tag{3.9}$$

$$-(\rho c_{11})^{1/2}(A-B) = -(\rho' c_{11}')^{1/2} B' \tag{3.10}$$

The particle velocity reflection r_v and transmission t_v coefficients are given by

$$r_v(0) = \frac{v_x(0)_R}{v_x(0)_I} = \frac{B}{A} \tag{3.11}$$

and

$$t_v(0) = \frac{v_x'(0)_T}{v_x(0)_I} = \frac{B'}{A} \tag{3.12}$$

Solving the simultaneous equations for B and B' gives the particle velocity reflection and transmission coefficients,

$$\frac{B}{A} = -\left[\frac{(\rho' c_{11}')^{1/2} - (\rho c_{11})^{1/2}}{(\rho c_{11})^{1/2} + (\rho' c_{11}')^{1/2}}\right] = r_v(0) \tag{3.13}$$

and

$$\frac{B'}{A} = \frac{2(\rho c_{11})^{1/2}}{(\rho c_{11})^{1/2} + (\rho' c_{11}')^{1/2}} = t_v(0) \tag{3.14}$$

The stress reflection and transmission coefficients can also be derived for $r_T(0)$ and $t_T(0)$ using a similar approach with the traction force and this gives,

$$r_T(0) = \frac{(\rho' c_{11}')^{1/2} - (\rho c_{11})^{1/2}}{(\rho c_{11})^{1/2} + (\rho' c_{11}')^{1/2}} \tag{3.15}$$

and

$$t_T(0) = \frac{2(\rho' c_{11}')^{1/2}}{(\rho c_{11})^{1/2} + (\rho' c_{11}')^{1/2}} \tag{3.16}$$

The acoustic reflectance and transmittance at a boundary are usually expressed in terms of the ratio of impedances either side of the boundary where reflectance $R = |r|^2$ and transmittance $T = \left|\frac{\rho_1}{\rho_2} t\right|^2$ and the impedance expressed in terms of the

material density and elastic constant is given by $Z=(\rho c_{11})^{1/2}$. Therefore the proportion of the propagating elastic waves through a material that are incident on a plane boundary with an impedance mismatch that are reflected and transmitted will be given by equations (3.17) and (3.18).

$$R_T(0) = \left| \frac{Z_2 - Z_1}{Z_2 + Z_1} \right|^2 \tag{3.17}$$

and

$$T_T(0) = \left| \frac{\rho_1}{\rho_2} \frac{2Z_2}{Z_2 + Z_1} \right|^2 \tag{3.18}$$

This can be extended to a structure with many boundaries such as for a multilayered stack where the introduction of the periodic structure of layers gives a set of reflections at certain frequencies which is determined by the properties of the stack.

3.1 Bragg Mirrors

Distributed acoustic Bragg reflectors consist of periodic layers of alternating high and low acoustic impedances (figure 3.2) and display a plateau of high reflectivity centred at a fundamental Bragg frequency. Acoustic Bragg reflectors manufactured from pSi have not been extensively studied within the literature despite being easily fabricated using electrochemical etching. Essentially, Bragg mirrors display a one dimensional (1-D) phononic band-gap and the width of this band-gap is called the acoustic bandwidth of the Bragg reflector. Propagation of sound through a lattice or periodic structure of scattering centers gives rise to a range of frequencies at which propagation is forbidden and are known as band-gaps. These band-gaps cut selected frequencies from the transmission spectrum, for example to filter and remove noise.

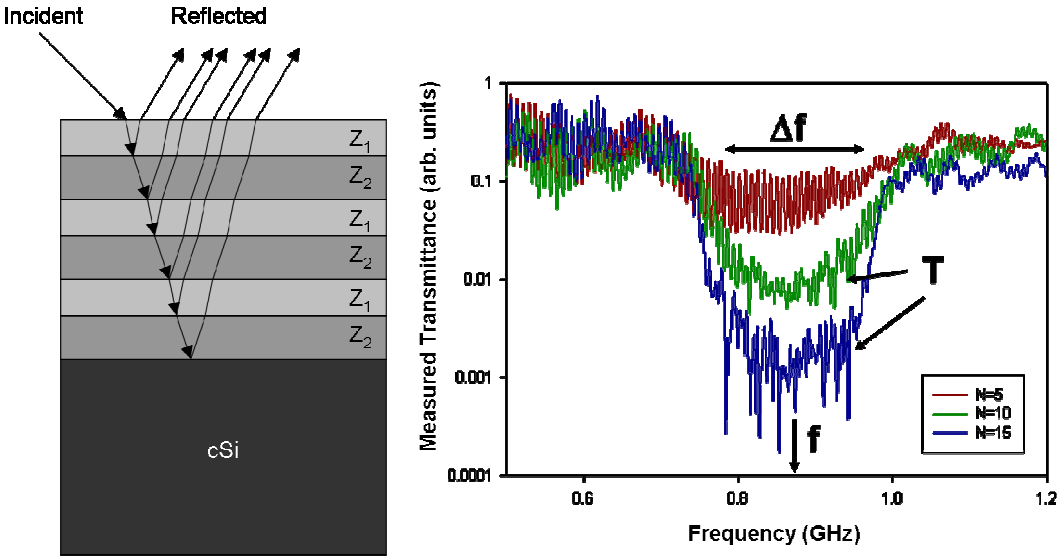

Figure 3.2 (Left) Bragg reflector consisting of a stack of multilayers of high Z_1 and low Z_2 acoustic impedance layers of thickness $d_1=1.3\mu m$ and $d_2=1.2\mu m$ on a cSi substrate and (Right) increasing reflectivity of the stopband with an increasing number of layers.

The properties of single pSi layers are important to aid the understanding of how this material will behave in a multilayered stack when incorporated into the acoustic devices mentioned in chapter 1. Acoustic waves incident on a single layer of pSi will be partially reflected, transmitted and undergo scattering at each boundary where there is an acoustic impedance mismatch, such as between the first medium with the pSi layer and also the pSi layer boundary with the cSi substrate. When the number of pSi layers is increased then the number of boundaries with an acoustic impedance mismatch is increased and there will be additional reflections and transmissions across the multilayered stack compared to that seen for a single layer of pSi. It is possible to make a multilayered stack so that the reflected waves interfere constructively so as to create a strong reflected signal at a chosen fundamental frequency which primarily depends upon the thicknesses of the individual layers that make up the multilayer. The summation of reflections from the multilayer gives rise to a highly reflective band of frequencies.

For BAW devices, the multilayer or Bragg mirror can be designed to control the range of frequencies reflected or transmitted by changing the acoustic impedance (Z_1 and

Z_2) properties and layer thicknesses (d_1 and d_2) of the individual layers making up each pair of layers repeated in the multilayer, shown in figure 3.2. If the transmission properties of the acoustic Bragg mirror are studied there will be a range of frequencies that are not transmitted because they have been reflected i.e. the stopband which consists of a set of frequencies that are forbidden. In chapter 7 acoustic transmission measurements have been performed on fabricated pSi Bragg mirrors and the properties of the stopbands seen are discussed, for this reason it will be necessary to focus on discussing stopbands emerging from the Bragg mirrors where the deeper the stopband seen, the higher the reflectivity of the mirror.

For optical applications, Bragg gratings can be made with photosensitive fibre for uses in fibre lasers, pump stabilisers (of diodes) and dispersion compensators with a chirped Bragg grating to reflect different wavelengths of light at each point along the grating. AlGaN/GaN Bragg mirrrors have been grown by metal organic CVD (MOCVD)[33] for applications such as vertical cavity lasers and Bragg mirrors have also been implemented into resonator devices.[34] Existing Si-based optical Bragg mirrors use alternating layers of amorphous Si and SiO_2 where the major advantage of using Si as the fabrication material is the realisation with integrated circuitry. The parameters defining existing photonic structures fabricated from pSi can be modified to fabricate structures with determined phononic responses. Bragg mirrors fabricated from pSi can be further modified to shift the fundamental Bragg frequency by filling the pores with different liquids to change the effective refractive indices or effective acoustic impedance of the layers.[35, 36]

The equations governing the optical reflectance properties of a multilayered stack are given by Bragg's laws described below by equations (3.19) to (3.21) at normal incidence where the refractive index of the first and second layers are n_1 and n_2, the thicknesses of the layers is given by d_1 and d_2, N is the number of repeated bilayers in the stack, M is the mode of the reflectance peak and λ_B is the Bragg wavelength. The fundamental Bragg wavelength is given by λ_B with the stopband width described by $\Delta\lambda$ and the reflectance of the band by R_B.

$$\lambda_B = \frac{2}{M}\left(n_1 d_1 + n_2 d_2\right), \quad M = 1,2,3,... \tag{3.19}$$

$$\Delta\lambda = \frac{4}{\pi}\lambda_B \arcsin\left(\frac{n_1 - n_2}{n_1 + n_2}\right) \tag{3.20}$$

$$R_B = \left[\frac{(n_1/n_2)^{2N} - 1}{(n_1/n_2)^{2N} + 1}\right]^2 \tag{3.21}$$

The response from a pSi optical Bragg mirror designed to have an optical reflectivity band around 700nm is given in figure 3.3 below. Refer to the appendix for sample details.

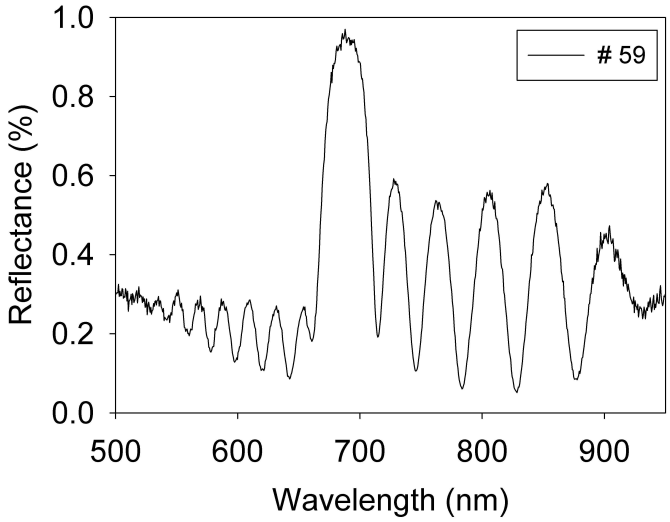

Figure 3.3 Optical Bragg mirror with fundamental stopband at 700 nm.

The derivation of these equations comes from analysing the reflectance of light from a single layer as detailed in chapter 5. The individual layers in a Bragg mirror are usually around a quarter-wavelength thick; $n_1d_1 = n_2d_2 = \frac{\lambda}{4}$. At frequencies of 1 GHz bulk acoustic waves traveling through pSi have wavelengths of similar length to optical waves and Bragg's laws can be applied to multilayers designed for acoustic applications. The following equations (3.22) to (3.24) come directly from the derivation of Bragg's law for optical media where the frequency $f \sim \lambda^{-1}$ and the acoustic impedance $Z \sim n^{-1}$.

$$f_B = \frac{M}{2}\left(\frac{\rho_1 d_1}{Z_1} + \frac{\rho_2 d_2}{Z_2}\right)^{-1} \quad M = 1, 2, 3\ldots \tag{3.22}$$

$$\Delta f = \frac{4}{\pi} f_B \sin^{-1}\left(\frac{Z_2 - Z_1}{Z_2 + Z_1}\right) \tag{3.23}$$

$$T_B = 4\left(\frac{Z_1}{Z_2}\right)^{2N} \Bigg/ \left(\left(\frac{Z_1}{Z_2}\right)^{2N} + 1\right)^2 \tag{3.24}$$

At normal incidence, the Bragg frequencies f_B of the stopbands of an acoustic filter can be described by equation (3.22) where M is the stopband order number, ρ_1 and ρ_2 are the mass densities of the A and B layers of the different repeating AB layers, d_1 and d_2 are the physical thicknesses of each layer, and Z_1 and Z_2 are the characteristic acoustic impedances of the layers given by the product ρV where V is the velocity of the longitudinal acoustic wave through a layer of a specific porosity. In chapter 5.4 the velocity dependence on porosity is discussed for pSi material. For a balanced Bragg mirror, the bandwidth Δf can be described by equation (3.23) and the Bragg transmittance T_B of the multilayered stack described by equation (3.24) where N is the number of repeats of the AB pairs of layers. Note that $T_B=1-R_B$ for an ideal Bragg mirror without loss where R_B is the Bragg reflectance.

As will be discussed in detail in chapter 4, electrochemical etching is the technique used to produce single layered and multilayered pSi structures. This enables control of the spatial porosity profile through the multilayer which is determined by current modulation with time during fabrication. This porosity profile corresponds to an effective refractive index profile which can be used to produce optical devices, or analogously to the effective acoustic impedance profile used for acoustic devices. Note that reference made to the 'optical thickness' of the mirror does not correspond to the physical thickness but to the product nd; when the 'acoustic thickness' is referred to this corresponds to d/V (or the time of flight τ for acoustic waves to travel through the layer). The optical and acoustic thicknesses determine the symmetry (or asymmetry) of the Bragg mirror. For example, consider an optical Bragg mirror where each individual layer within the pair of layers has $n_1d_1=n_2d_2$. This optical Bragg mirror will be symmetrical and not exhibit even order modes.

Examples of pSi optical devices previously studied include Bragg mirrors, filters, microcavities and devices for sensing.[35,37] Recent sensing work has used optical rugate filters, employing a sine-wave effective refractive index modulation that possesses the same fundamental frequency as the equivalent quarter-wave stack of Bragg mirrors, the difference in the two profiles is seen in the transmission (or reflection) spectrum. Whereas the Bragg mirror gives a number of band-gaps with higher-order harmonics, the rugate filter gives only one strong reflectivity band with heavily suppressed higher-order harmonics.[38] The realization of apodized pSi optical rugate filters,[39,40] with high reflectivity and narrow bandwidth demonstrates the suitability of pSi for a variety of precision engineering applications. A theoretical study of pSi for acoustic Bragg mirrors and rugate filters has previously shown its potential for acoustic devices.[41] Recently the tunability of the physical properties of Si with porosity has been used for hypersonic acoustic structures.[42,43] This relies on the calibration of the effective acoustic impedance by measuring the wave velocities as a function of porosity.[44]

For pSi Bragg mirrors, the mass density ρ of each layer is a function of the porosity and is described by equation (3.25) where ρ_0=2.329 g cm^{-3} is the density of Si and p is the porosity or air-filling fraction. The acoustic velocity dependence on porosity is given empirically by equation (3.26) for heavily doped p++ Si wafers with etching in the [100] crystallographic direction, where V_0=8.436 km s^{-1} is the longitudinal acoustic velocity in Si in the [100] crystallographic direction.

$$\rho=\rho_0(1-p) \tag{3.25}$$

$$V=V_0(1-p)^k \tag{3.26}$$

The empirical exponent k = 0.6 for the pSi samples used in this investigation. Pure longitudinal waves are excited along this direction due to the cubic symmetry of silicon and it is the assumption that pSi retains this cubic symmetry of the parent wafer.[32] Note that if pSi possesses tetragonal symmetry the velocity dependence in the [100] direction is identical to that for cubic symmetry (see chapter 2).

Bragg mirrors based on heavily doped p-type Si wafers have an effective acoustic impedance dependence on porosity as outlined in figure 3.4. This empirical data comes from measuring the longitudinal sound velocity through a range of single-layered pSi films and this is described in chapter 5.4. Following equations (3.25) and (3.26) the effective acoustic impedance dependence on porosity is given by equation (3.27) where the exponent k for samples used in this investigation is 0.6.

$$Z_{pSi} = Z_{cSi}(1-p)^{k+1} \tag{3.27}$$

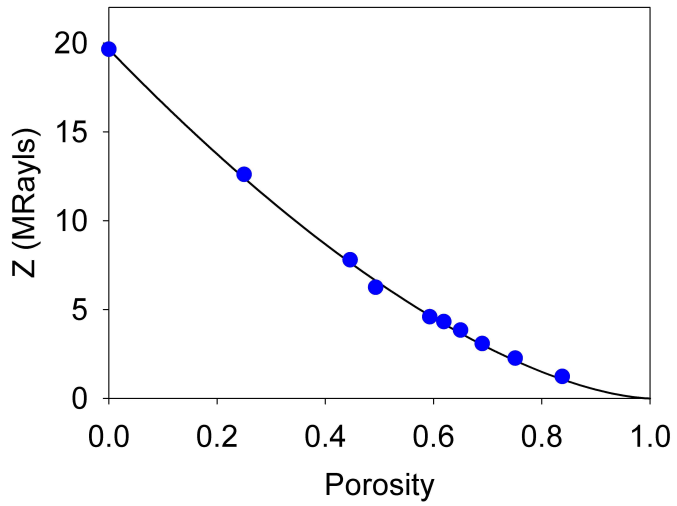

Figure 3.4 The porosity dependence of the effective acoustic impedance profile for p++ Si wafers.

For the Bragg mirror shown in figure 3.2 the increase in the number of bilayers increases the depth of the stopband due to more reflection contributions from the additional interfaces. For the parameters used for the fabrication of this pSi multilayer, the high Z_1 and low Z_2 acoustic impedance layers are 4.2 MRayls and 2.9 MRayls (for layer porosities of 62 % and 70 %) and the thicknesses of the layers d_1 and d_2 are 1.28 μm and 1.23 μm respectively. The pSi stack is on a cSi substrate for which Si has an acoustic impedance of 19.6 MRayls. Figure 3.5 shows the increase in the depth of the stopband as the number of pairs of layers is increased using equation (3.24). For the measured transmittance of the pSi stacks shown in figure 3.2 (right) for numbers of bilayers of N = 5, 10 and 15, theoretical values for the transmittance have been found using the curve of figure 3.5 (left) and are in close agreement with these

experimental observations. Figure 3.5 (right) gives theoretical fits for the transmittance of a Bragg mirror as a function of the pairs of layers in the stack for different degrees of impedance mismatching between the *AB* layers. It can be seen that the depth of the stopband increases with increasing pairs of layers and that the stopband emerges quickest for the largest impedance mismatch *dZ* between the *AB* layers i.e. $dZ = |Z_1 - Z_2|$. This is due to a larger proportion of the acoustic wave being reflected at each boundary which gives rise to a stronger reflectance band, and hence deeper stopband.

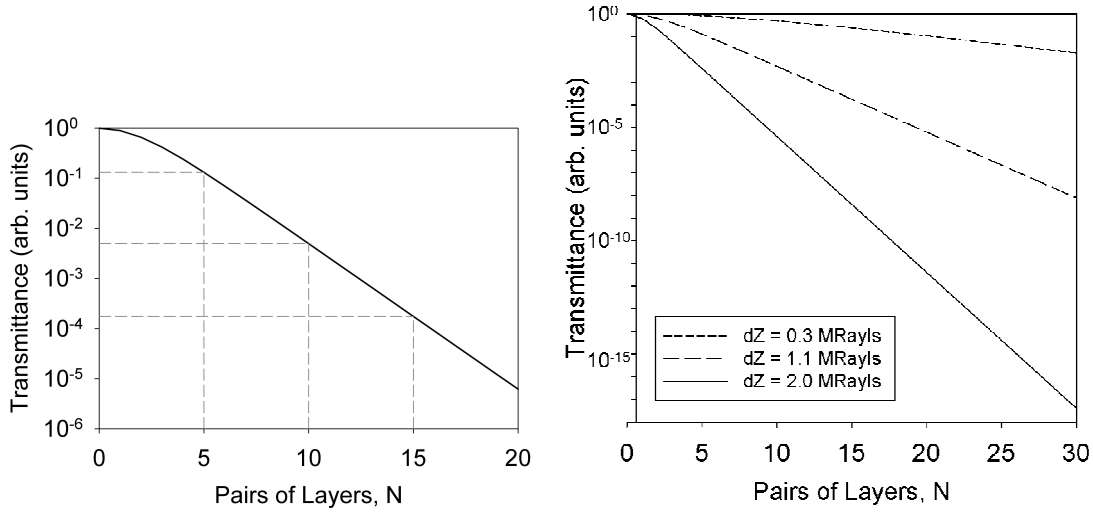

Figure 3.5 (Left) As the number of pairs of layers in the stack *N* is increased, the transmittance of acoustic waves through the stack decreases and (Right) the larger the impedance mismatch between the layer pairs, the less pairs are needed to obtain a deep transmittance stopband.

3.2 Symmetric and Asymmetric Mirrors

The introduction of a periodic multilayer (also known as a superlattice) gives zone-folding of the longitudinal acoustic phonons in the pSi mirror. The dispersion relation for a pSi stack can be described and this will be dependent upon the layer porosities and the morphology of the pSi since this affects the dependence of the velocity of acoustic waves through the material. For example, the phonon dispersion of Si nanocrystals has been found to be close to the phonon dispersion of bulk Si.[45] The

zone-folding also has a dependence on the ratio of the thicknesses of each bilayer. Brillouin scattering measurements can confirm the dispersion relation for a pSi stack[46] and folded phonon branches in multilayered structures are studied to determine device response using the optical generation and transmission of ultrasonic pulses through the superlattices.[47] The acoustic phonon folding in a pSi multilayer is described by the Kronig-Penney like dispersion relation that uses the correct power laws for the measured acoustic velocity of longitudinal waves through pSi.

For an infinite 1-D superlattice with each of the *A* and *B* layers having thicknesses d_1 and d_2 where $d = d_1 + d_2$ and the acoustic impedance of each layer is given by Z_1 and Z_2, the dispersion relation is given by Rytov as follows in equation (3.28). The phonon wavevector is described by k where τ_1 and τ_2 are the time of flights of acoustic waves in layer 1 and 2 respectively and ω is the angular frequency.[48]

$$k = \frac{1}{d}\cos^{-1}\left[\cos\omega\tau_1\cos\omega\tau_2 - \frac{1}{2}\left(\frac{Z_1}{Z_2}+\frac{Z_2}{Z_1}\right)\sin\omega\tau_1\sin\omega\tau_2\right] \quad (3.28)$$

Applying this dispersion relation to pSi can be done using the known acoustic impedance and velocity dependence on porosity as described later in chapter 5. The centre of the Brillouin zone gaps are given at the frequencies f_M in equation (3.29) below where an even value of *M* relates to the centre of the gap and an odd value of *M* relates to the Brillouin zone edge and where *V* is the average acoustic velocity in the two layers.

$$f_M = M\pi\frac{\mathrm{V}}{d} \qquad \mathrm{M}=1,2,3... \qquad (3.29)$$

$$\text{where } V = \frac{d}{(\tau_1+\tau_2)}$$

The gap width Δf at the centre and edge of the Brillouin zone is given by equations (3.30) and (3.31) where the superscripts c and e correspond to the centre and edge of the zones.

$$\Delta f_M^c \approx 4\frac{V}{d}\left|\Delta Z\sin\left(f_M^c\Delta\tau\right)\right| \qquad (3.30)$$

$$\Delta f_M^e \approx 4\frac{V}{d}\left|\Delta Z \cos\left(f_M^e \Delta\tau\right)\right| \qquad (3.31)$$

where the acoustic impedance mismatch $\Delta Z = \frac{Z_1 - Z_2}{Z_1 + Z_2}$ and the difference between the time of flights is $\Delta\tau = \tau_2 - \tau_1$.

The dispersion relation for a pSi multilayer has been modelled using equation (3.28) and is shown below in figure 3.6 where the phonon frequency *f* is a function of the *k*-vector.

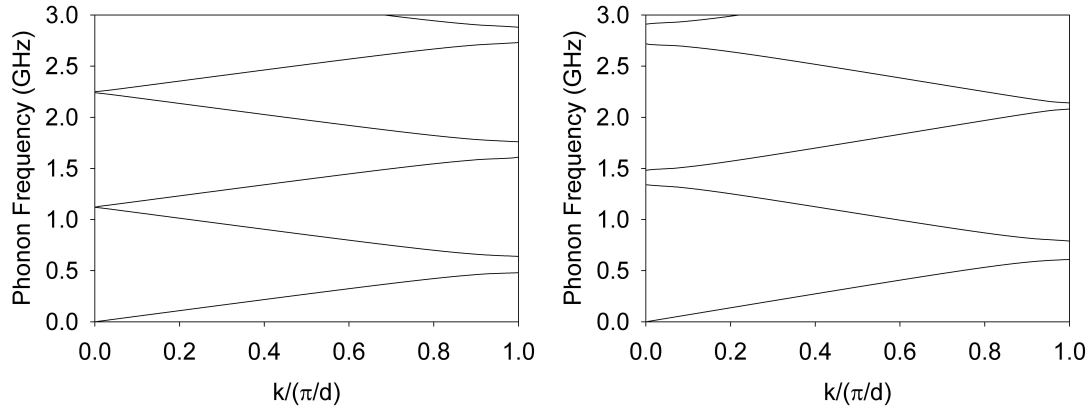

Figure 3.6 Calculated dispersion relations for a (left) symmetrical and (right) asymmetrical multilayered mirror with the parameters stated in figure 3.7.

Balanced or symmetrical Bragg mirrors only exhibit odd modes (for M = 1, 3, 5 …) as shown in figure 3.6 (left) where the dispersion relation shows bandgaps that are open at k/(π/d) = 1 and closed at k/(π/d) = 0. Unbalanced or asymmetrical mirrors display a collection of odd and even higher order modes such as in figure 3.7 (right) where the dispersion relation shows open bandgaps. For the acoustic simulations shown, see chapter 6 for transfer matrix modelling. It is possible to design Bragg mirrors to possess only odd higher order modes by making the acoustic mirror symmetrical using layers for which the acoustic waves travelling though each of the A and B layers have the same time of flight i.e. $\tau_1 = \tau_2$ (balanced optical mirrors would have the same optical thickness) in the stack. For an asymmetrical acoustic mirror the frequency

response seen from the mirror will give a collection of odd and even higher orders for layers with time of flights of $\tau_1 \neq \tau_2$. For any design of acoustic mirror there will always be a fundamental mode of the stopband located at the lowest frequency. The properties of stopbands at higher orders can be described using the dispersion relation, equation (3.28).

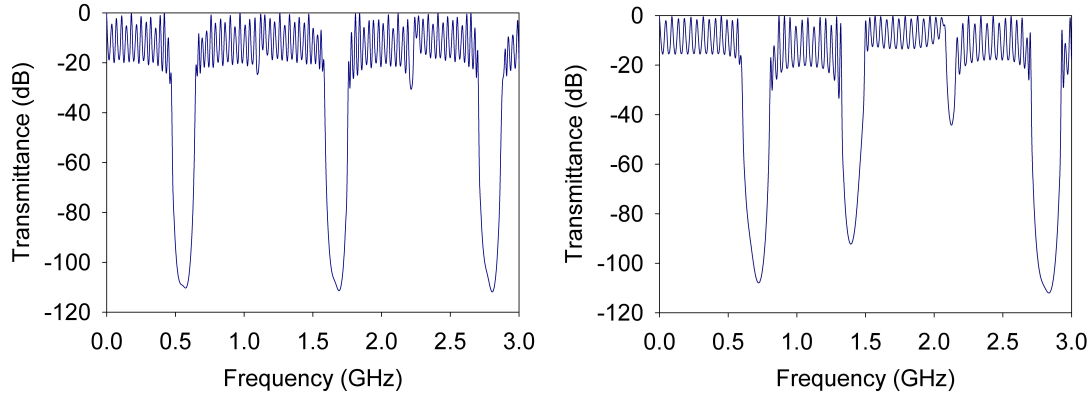

Figure 3.7 Examples of balanced (left) and unbalanced (right) Bragg mirrors. The parameters used for these simulations are as follows, *d1*=2.089μm *d2*=1.677μm *p1*=0.645 *p2*=0.735 (left) and *d1*=2.168μm *d2*=1.05μm *p1*=0.61 *p2*=0.71 (right) where both mirrors have *N*=15 pairs of layers.

For the balanced Bragg mirror shown in figure 3.7 (left) the fundamental mode is seen at a frequency of 0.56 GHz and no even order modes are visible. The higher order modes observed at 1.68 GHz and 2.80 GHz are the third and fifth modes respectively. For the unbalanced Bragg mirror shown in figure 3.7 (right), both odd and even higher orders can be seen at higher frequencies than the fundamental mode at 0.7 GHz. The second order is at a frequency of 1.4 GHz, the third order at 2.1 GHz and the fourth higher order at 2.8 GHz. Figure 3.8 shows another example of the modeled acoustic response of a symmetric and asymmetric Bragg mirror that both have porosities p_1=0.55 and p_2=0.47 in layers *A* and *B* respectively for *N*=15 pairs of layers, but have different layer thicknesses such that the time of flight of acoustic waves through each layer gives $\tau_1 = \tau_2$ and $\tau_1 = 5\,\tau_2$. Note that for the symmetric mirror there are no even ordered modes at frequencies of 2, 4 and 6 GHz whereas for the asymmetric mirror there is no *M*=6 mode at a frequency of 6 GHz.

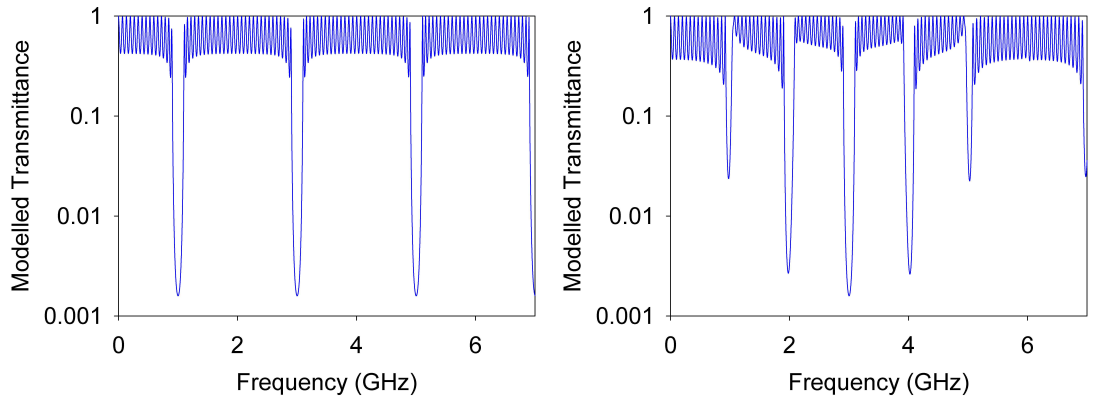

Figure 3.8 (Left) Symmetric Bragg mirror for $\tau_1 = \tau_2$ with parameters d_1=1.31μm and d_2=1.44μm and (Right) asymmetric Bragg mirror for $\tau_1 = 5\tau_2$ with parameters d_1=2.19μm and d_2=0.48μm.

3.3 Impedance Profiling: Bragg Mirrors and Rugate Filters

The acoustic impedance profile *Z(d)* determines the response of the multilayer in the frequency domain. An example of a square-wave profile describing a Bragg mirror and a sinusoidal-wave profile describing a rugate filter is shown in figure 3.9 The profiles both have the same periodicity, number of pairs of layers and the same high and low values of the acoustic impedance between each layer.

The versatile nature of pSi allows the effective acoustic impedance of the layers to be easily manipulated by controlling the porosity. The effective acoustic impedance profile determines the response of the multilayered device. Similarly to the Bragg mirror, a rugate filter is periodic but with a sinusoidal modulation in its profile and produces one reflectivity peak per sine component of the profile. Acoustic rugate filters have a sinusoidal modulation in the acoustic impedance profile as shown in figure 3.9(bottom).

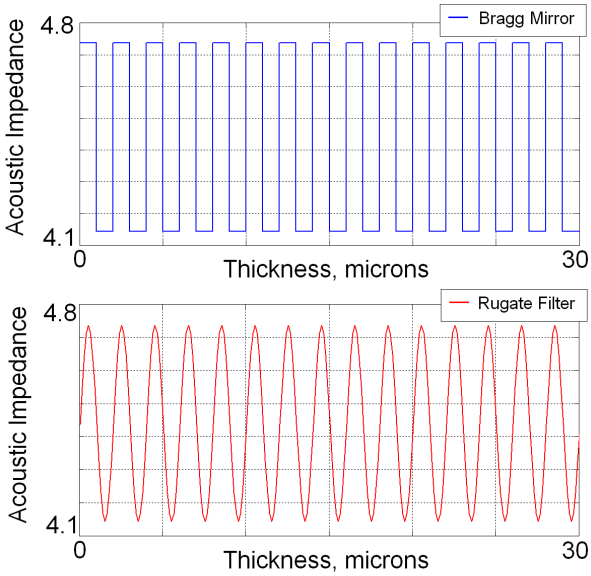

Figure 3.9 Acoustic impedance profile for a Bragg mirror (top) and a rugate filter (bottom).

The response of each acoustic multilayer, each with the same period, is highlighted by the transmittance spectrum of figure 3.10 where the fundamental mode of each mirror is observed at the same fundamental frequency. The higher orders for each mirror are at the same locations in frequency but the transmittance of each stopband is different. The higher orders are heavily suppressed for the rugate filter which shows only the fundamental stopband and a small third order stopband. In contrast the Bragg mirror displays the fundamental mode and four higher-order stopbands for this frequency range. See chapter 6 later for details on the simulations.

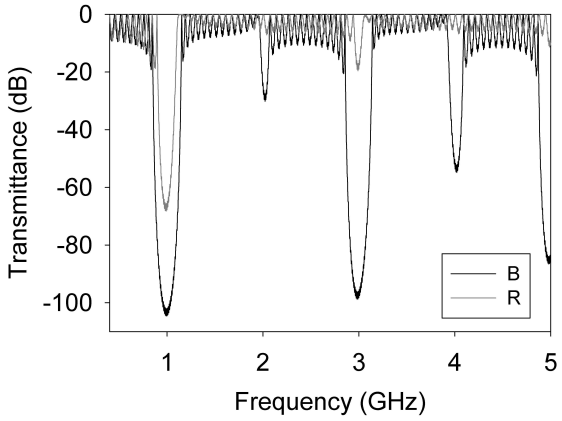

Figure 3.10 Effect of the acoustic impedance profile on the response of the acoustic multilayer designed for *d1*=*d2*=1.4μm *p1*=0.42 *p2*=0.56 and *N*=15.

The transmissivities of dielectric structures using a continuously varying refractive index have been studied and the spectral response of these rugate filters have previously been modeled using coupled-wave theory.[49,50] Due to the tunability of the acoustic impedance profiles it would be possible to combine multiple profiles into one mirror to create a highly controlled acoustic response. For example, very wide stopbands can be created by overlapping the fundamental frequencies of a number of Bragg mirrors.

3.3 Optical Properties of 'Acoustic' Mirrors

The pSi material making up the multilayers in this investigation can be used to produce optical or acoustic Bragg mirrors. The effective refractive index of the pSi depends upon the porosity of the layer as discussed later in chapter 5, as does the effective acoustic impedance. The pSi mirrors fabricated have both optical and acoustic responses which are both determined by the profile of the mirror. For waves at a frequency of 1 GHz the wavelength of the longitudinal acoustic waves in the pSi medium is of the same order as electromagnetic waves in the visible and infra-red regions of the spectrum. Given the thickness of the layers used for 1 GHz frequencies, there will be an equivalent response of the mirror studied optically i.e. for a fundamental band-gap at 1 GHz there will also be a fundamental stopband in the far-

infrared region ~ 7 μm. An example is shown in figure 3.11 where the higher order modes can be seen towards the visible range. It is possible to characterise Bragg mirrors fabricated from pSi using the acoustic and optical responses of the stack to determine the exact thickness and porosity of each layer.

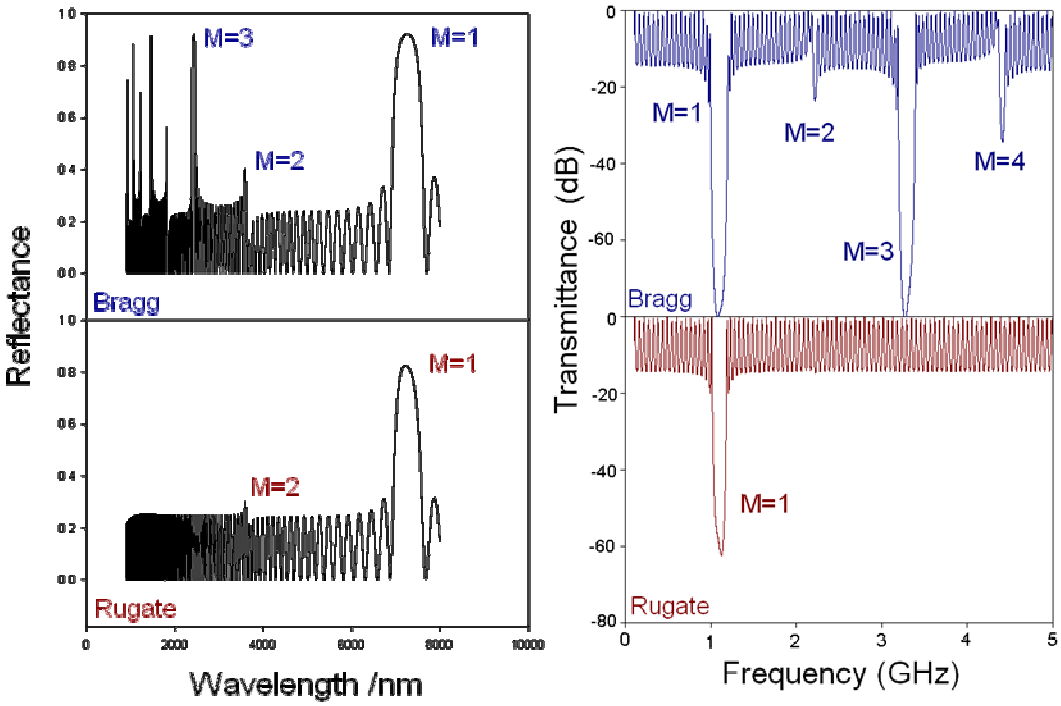

Figure 3.11 Optical (left) and acoustic (right) simulations of a Bragg mirror and rugate filter with *d1*=*d2*=1.05μm *p1*=0.605 *p2*=0.665 *N*=20.

3.4 Fabry-Perot Filters (Microcavities)

Other structures fabricated from pSi include microcavities which involve the insertion of a defect layer between two distributed Bragg reflectors.[51] For optical applications this defect layer will be a half-wave thickness, or the thickness of one *AB* pair of layers in the Bragg stack which allows for a standing wave to form inside the defect layer through resonance. These are useful for laser applications, figure 3.12 gives an example of a pSi microcavity multilayer that has a transmission peak inside the reflectance band with a mirror quality factor (Q-factor) $\lambda/\Delta\lambda$ near 1,450 which is poor

compared to the Q-factor of other semiconductor resonant systems which can have Q-factors of around 34,000.[52]

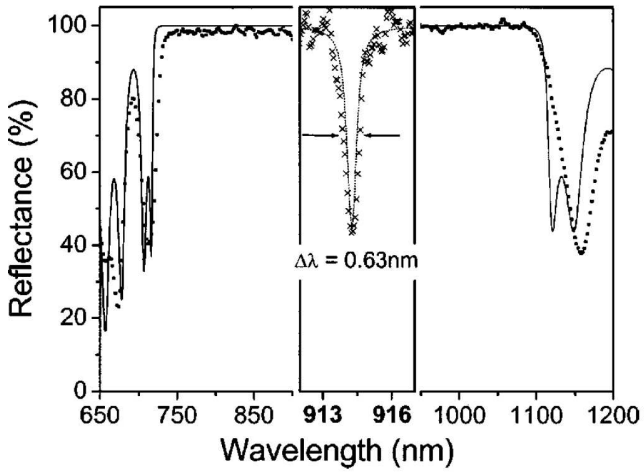

Figure 3.12 Example of a pSi optical Microcavity with Q-factor ~1,450.[53]

In order to fabricate microcavities based on pSi for acoustic applications, the defect layer has to be the thickness of one *AB* pair of layers such that the time of flight in the defect layer is ~2τ. The defect layer, also known as the cavity layer, allows for a small bandwidth of frequencies to be transmitted inside the stopband. Figure 3.13 shows the layer structure for a microcavity where the shaded layers have high acoustic impedance and the light layers have low acoustic impedance. The high acoustic impedance layers have to be thicker to obtain the same time of flight in each layer because the longitudinal waves travel faster through lower porosity layers.

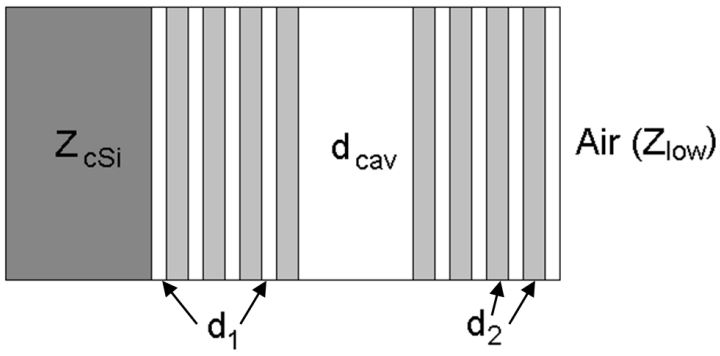

Figure 3.13 Layer structure describing a microcavity which contains a defect cavity layer sandwiched between two Bragg mirrors.

There are many parameters affecting the transmission of the microcavity which include the number of *AB* layers in the Bragg mirrors either side of the defect layer, the shape of the sides of the cavity layer since this affects the coupling coefficients, the thickness of the cavity layer affects the location in frequency of the transmission peak inside the stopband, the porosity profile across the cavity layer and the Bragg mirrors, and the thickness and porosity of the *AB* layers which affects the symmetry of the mirrors. For microcavities based on pSi in this investigation, the desired fundamental frequency is near 1 GHz due to equipment limitations.

If an acoustic microcavity with a high Q-factor can be achieved using pSi it could be possible to trap sound and light together in a pSi resonator for applications with acousto-optic modulators through the acousto-optic interaction.

The properties of multilayered structures have been discussed in this chapter, particularly for the case of pSi multilayers. Regions exist in the dispersion curves of multilayered systems that give rise to bandgaps which are regions where certain frequencies are forbidden. A set of equations are used to design the desired response of the multilayers such as Bragg mirrors, rugate filters and microcavities. The acoustic impedance of pSi depends on the porosity chosen and the acoustic impedance profiles can be tailored for pSi to control the frequency response of the mirrors. The next chapter will look at the fabrication of the pSi multilayers and control of the acoustic impedance profiles of the different types of acoustic mirrors investigated.

4. Electrochemical Etching of Porous Silicon

Si wafers can be manufactured using the Czochralski (CZ) crystal growth method where a seed crystal is pulled from a molten mixture of pure Si and dopant impurity atoms. As the seed crystal grows an ingot of doped Si forms which is later sliced to form the Si wafers. Bulk Si can be stain etched with sodium hydroxide (NaOH) or potassium hydroxide (KOH); this is the main method to produce single layered pSi with fixed porosity. Single pSi layers can also be etched with nitric acid and hydrofluoric acid (HNO_3 + HF),[54,55] with iron chloride ($FeCl_3$ + HF) or with ammonium fluoride (NH_4F) to obtain single layers with fixed porosity. However, there is no dynamic control over the porosity since only single layers of a fixed porosity can be fabricated with these methods. To fabricate pSi multilayers, electrochemical etching of bulk cSi wafers is used as this allows control over the porosity profile with layer thickness. The pSi multilayered structures fabricated for use in this study have all been electrochemically etched from the most commonly used CZ grown Si wafers. These have been heavily doped with boron atoms (p++) and have a typical resistivity of 1-15 mΩ cm. When electrochemically etched using a 1:1 volume of hydrofluoric acid (HF) to ethanol etch solution this produces mesoporous pSi with pores 10-20 nm in diameter.[56] The wafers used here are 4" in diameter before cleaving and the majority are 525 μm ± 25 μm thick although some wafers are thinner.

The Si wafers can be doped with group III atoms such as boron which introduces holes into the Si and is generally referred to as p-type Si. Boron doped Si wafers have been used to fabricate the pSi multilayers. The boron doping level of the Si wafers vary from lightly doped (p-) to heavily doped wafers (p++) for doping densities of ~10^{15} boron atoms per cm^3 to ~10^{19} per cm^3 of Si.[54] Note that for the heaviest doping levels this is approximately one boron atom per thousand Si atoms. The resistivities of the doped wafers are typically in the range of 2-5 Ω cm (microporous Si) for p-, 15-30 mΩ cm for p+ and 1-15 mΩ cm (mesoporous Si) for p++ samples, where microporous Si has pore sizes < 2 nm, 1-5mΩ cm mesoporous Si has pore diameters 2 – 20 nm and macroporous Si > 20 nm.

PSi material has different physical properties to that of the parent Si material and these are dependent upon the initial doping of the Si wafer and the conditions under which the pSi has been fabricated. The size of the pores in the porous material depend upon the dopant and initial doping level of the parent silicon wafer, HF concentration and etching current density.[54] Electrochemical etching requires the control of an etching current density to obtain different levels of porosity. By varying the current during fabrication alternating layers of high and low porosity can be achieved with typical porosities in the range 50 – 70 %. The result is a multilayered structure of pSi on a cSi substrate as shown in the scanning electron microscope (SEM) image of figure 4.1. The thickness of the different porosity layers can be controlled during fabrication with the etch time for each current density. This method of producing multilayered pSi can be used to create filter structures known as Bragg mirrors, Fabry-Perot filters, rugate filters and microcavities, as discussed in chapter 3, the properties of which are determined by parameters during the fabrication process. Typical individual layer thickness is a few microns for ~ 1 GHz samples although thinner layers ~ 100 nm in thickness have been fabricated for the higher frequencies of ~ 20 GHz measured in this particular study.

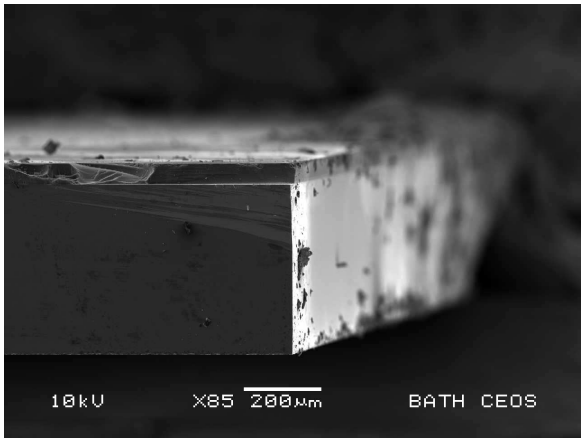

Figure 4.1 PSi multilayer seen on the surface of a Si wafer.

The pore morphologies that can be achieved etching p-type Si wafers are shown in figure 4.2 where the current density and doping level influence the pore growth.

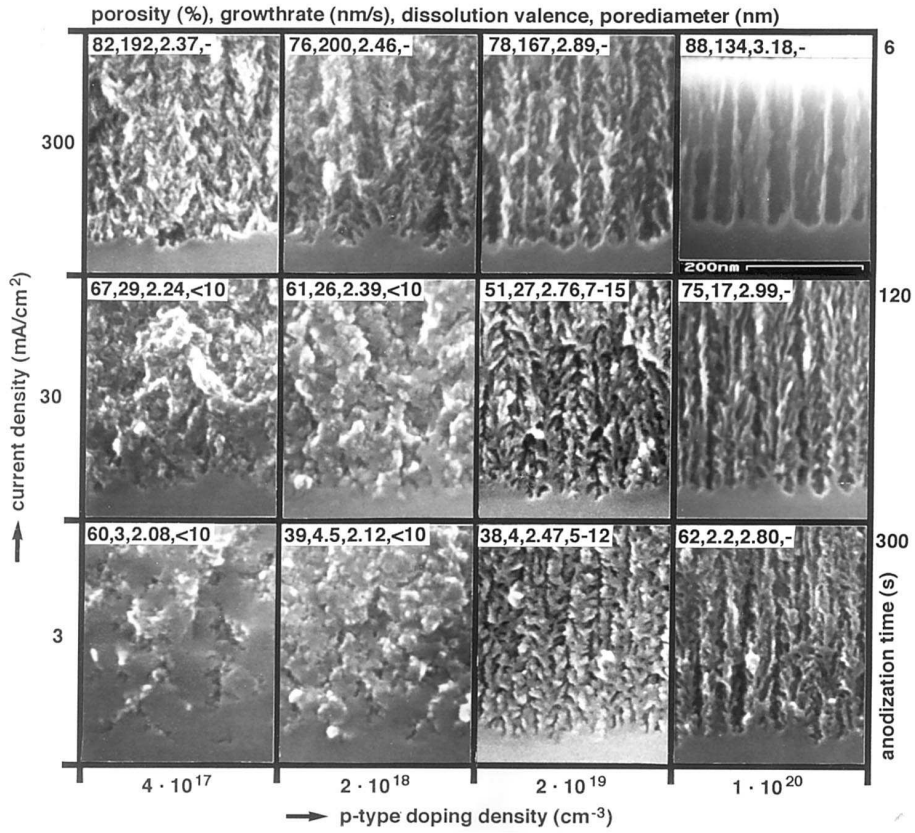

Figure 4.2 SEM images of the interface between bulk and pSi for p-doped <100> silicon electrodes anodized in ethanoic HF.[56]

An advantage of electrochemical etching is the ability to easily control the pSi layer thickness with the etch time, the pore size and morphology with dopant type and doping level, and the porosity with the etch current density and HF concentration. Etching occurs at the pore tip where there exists an active etch front which progresses into the Si substrate. Si is an anisotropic material with cubic symmetry[57] and pore evolution is always in a preferred crystallographic direction.[54] The direction of pore growth through the Si material is dependent on the plane surface that is exposed to the etchant. The direction of etching for the samples used in this study is in the [100] crystallographic direction where the main preferential pore growth is along this direction and side-branching from the main pore occurs along the (100) plane (or [001] and [010] crystallographic directions) as shown in figure 4.3.

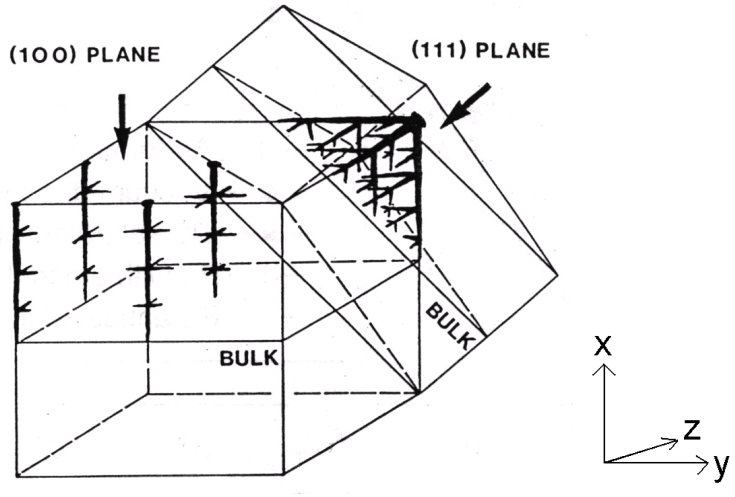

Figure 4.3 Pore morphology in the (100) and (111) planes.[54]

SEM images of pSi multilayers that have been electrochemically fabricated in the [100] direction are shown in figure 4.4 where the layers of different porosities can be distinguished and the higher porosity layers have wider pore diameters than the lower porosity layers.

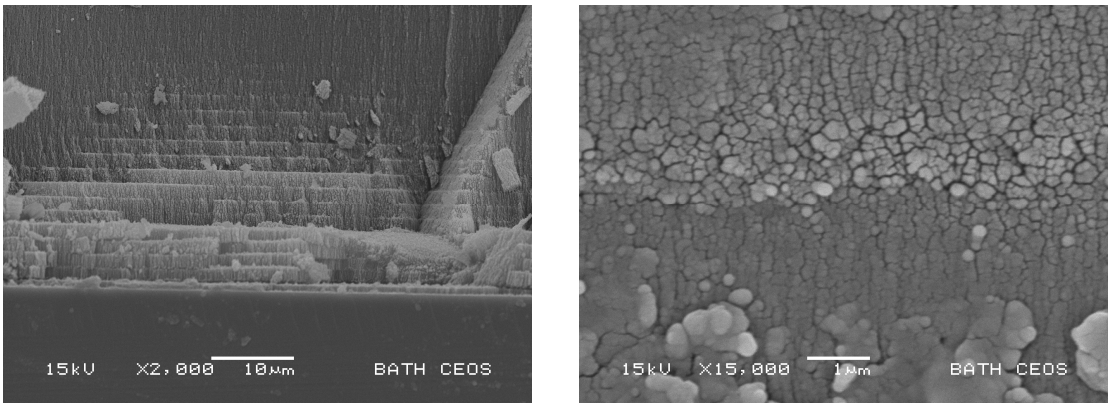

Figure 4.4 SEM images of multilayered pSi without a clean cleave so that a (Left) 3-D view of the layered system is visible and shows the (110) plane at an angle to the substrate for sample #6 and (Right) the wider pore diameter for a higher porosity layer on top of a lower porosity layer for sample #3.

The appearance of the pores etched in the (100) plane are column-like as shown by the SEM image in figure 4.5. The pores are closed at the substrate end and open at the surface of the wafer and all of the Si fragments remaining are interconnected via bridges of Si making a single structure. For higher porosity layers these bridges of Si are thinner. The pSi layers are essentially 1-D structures where the porosity profile through a section of the layers is modulated and can be viewed as a periodic structure; this then introduces phononic band-gaps whose properties are controlled by the porosity modulation.

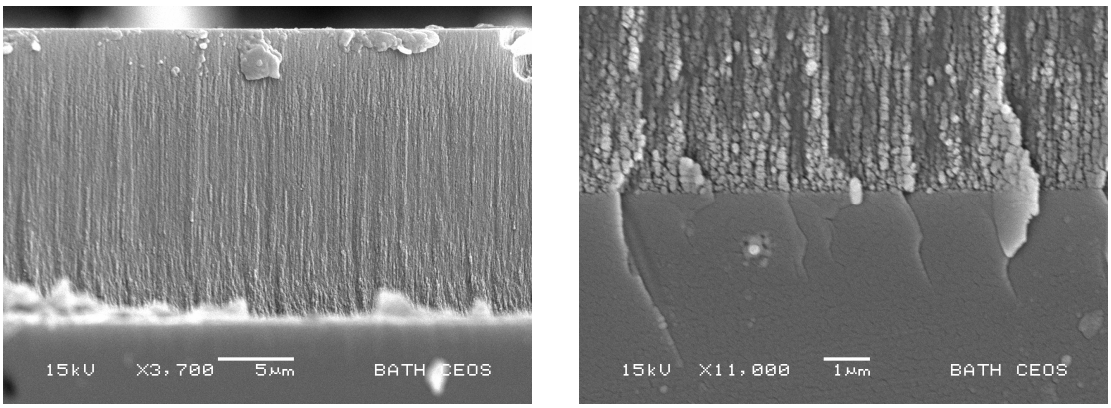

Figure 4.5 SEM images of pSi structures. Column-like appearance of pSi in [100] direction. (Left) PSi multilayer on cSi substrate. (Right) PSi at the cSi interface.

Details on the reaction of the electrochemical etching of Si in HF based solution can be found in the text by Lehmann.[54] The dissolution of Si in HF solution is initiated by the movement of a hole, due to the applied electric field, from the bulk of the Si wafer which approaches the Si - electrolyte interface (Fig 4.6 (a)). The surface of the Si wafer is hydrogenated. The mass transport of holes h^+ in the Si wafer and fluorine ions F^- in the electrolyte are central to the dissolution process where the number of holes moving is dependent upon the current density. When the HF_2^- in the electrolyte solution reaches the surface of the Si it dissociates into HF and F^- ions near to the surface (Fig 4.6 (b)) and excess hydrogen. When one of the Si – F bonds is established the second bond is broken when an electron migrates into the Si wafer. Excess hydrogen H_2 escapes as bubbles through the electrolyte solution (Fig 4.6 (c)). The two ionic Si – F bonds that are formed polarise the Si back-bonds enough to

sufficiently weaken them for further attack by the HF solution (Fig 4.6 (d)). The remaining Si bonds are hydrogen terminated and once all four Si bonds have been broken the Si atom is removed from the pore tip leaving behind an irregularity to the wafer surface that develops into a pore (Fig 4.6 (e)). Pore formation predominantly occurs at the tip of the pore as the electric field density is concentrated in these regions although side branching also occurs.[58] The remaining Si network of nanocrystals are not strongly etched as these regions are depleted of holes. Different pore morphologies occur depending on the doping properties of the wafers.[59] The morphology relates to the shape of the pores such as mesoporous Si where the structure of the pores are all interconnected via side-branching and bridges of nano-crystalline Si regions. Gibson and Ashby[60] describe the structure of cellular solids and foams where each pore or unit is made up of struts of Si and is valid for porosities less than 60%.

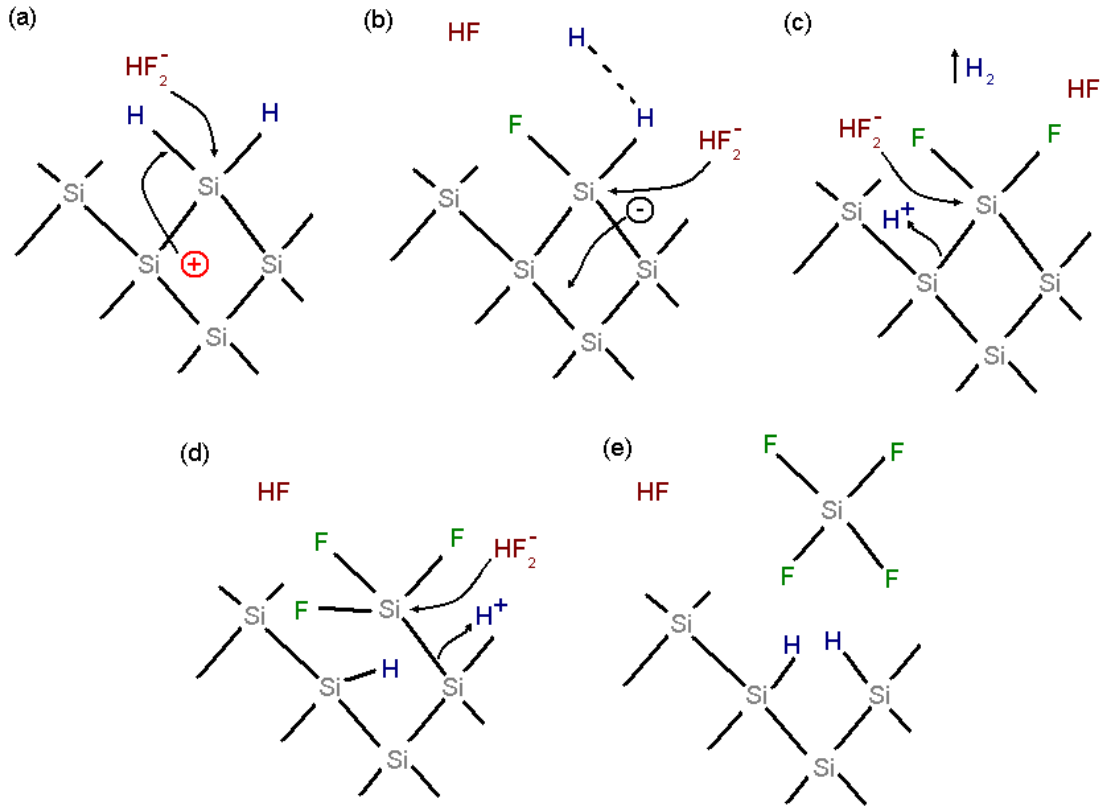

Figure 4.6 Reaction of electrochemical etching of Si in HF based ethanoic solution.[56]

The temperature of the electrolyte solution during the pSi fabrication process influences the etch rate and surface roughness.[61, 62] Previous studies have shown that the initial roughness observed at the Si wafer surface is carried through the pSi layer as the etch front progresses through the substrate.[63] Single-side polished (SSP) and double-side polished (DSP) wafers that have been mechanically and chemically polished have been chosen to minimise the surface roughness of the fabricated pSi and can have very smooth top layers with a roughness value at the atomic scale. For multilayered stacks of pSi layers with alternating high and low porosities there will be an interface between the layers. The roughness of this interface is dependent upon the initial surface roughness of the unetched Si wafer. If the pSi interfaces have features of a similar size or order to that of the acoustic wave incident on them then this could give rise to unwanted scattering effects during optical and acoustic measurements. It has been shown that low temperature etching reduces interface roughness due to the higher viscosity of the electrolyte solution.[61] PSi samples similar to the ones used here have been etched at lower temperatures in the dark to reduce the surface roughness of the pSi layer.[64] However, room temperature etching was used for samples in this investigation as it was found using atomic force microscope (AFM) measurements that the pSi surface roughness is < 5 nm which is much smaller than the wavelength of the acoustic waves (~ 1 μm) that were used to study the samples. The AFM measurements are discussed in chapter 5.

4.1 Etching Procedure

One type of etch cell commonly used is the horizontal etch cell used to fabricate pSi onto large areas of wafer where this cell has electrodes on the walls either side of the cell.[54] A vertical etch cell has electrodes at the top and bottom of the cell with the Si wafer located at the bottom electrode. The pSi layers required for this study needed to be microns in thickness so the release of hydrogen bubbles to avoid the build up of pressure within layers was very important. Excess hydrogen can cause layers to detach from the substrate and break the sample. The vertical etch cell set-up was chosen for the ideal orientation for the release of hydrogen bubbles from the developing pSi layer and as the most convenient method for the pSi fabrication of samples used in this study. During anodisation, the Si wafer acts as the anode and a HF resistant platinum wire which acts as the cathode is immersed in the HF and ethanol (EtOH) based electrolyte. During electrochemical etching, the anode corrodes into the wafer substrate removing silicon material. The use of the horizontal electrode allows for the release of hydrogen bubbles. The current flows perpendicular to the wafer surface creating a homogeneous porous layer.[54] A platinum wire grid served as the cathode and was placed in the electrolyte solution and the Si wafer in contact with a copper plate at the bottom of the etch cell served as the anode (figure 4.7). The platinum wire grid was placed parallel to the surface of the Si wafer to obtain a uniform current density across the etching area and the open grid network (as opposed to using a plate) allowed for adequate release of hydrogen bubbles. The Si wafer is fixed between the Teflon cell and the copper plate via clamping at the top of the etch cell.

One Si wafer is etched each time to produce one pSi single or multilayered sample. Each time a new sample is required the etch cell is dismantled and a new piece of cleaved Si wafer is placed at the base of the etch cell. A rubber O-ring is fixed between the Si wafer and the Teflon cell to prevent leakage and to allow a fixed surface area of the Si wafer in direct contact with the HF solution to be electrochemically etched. The diameter of the circular area in contact with the electrolyte is 25 mm, therefore the pSi samples are 25 mm in diameter with an etch area of 490 mm^2. The vertical etching cell was made from Teflon and used for anodic

etching of the bulk Si wafers using 48 wt% aqueous HF mixed with ethanol in 1:1 ratio. HF mixed with ethanol is used as the etchant so that the pores are completely infiltrated and homogeneous pSi layers are obtained.[65, 66]

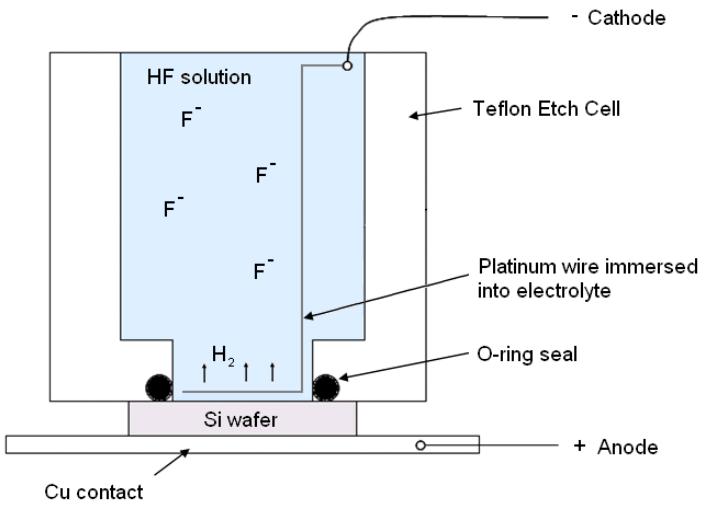

Figure 4.7 Electrochemical etch cell set-up.

The Si wafers are treated before etching to prepare the surface. Prior to etching the Si wafers have been baked in an oven at 300 °C for an hour to remove hydrogen from the top layer of the wafer which remains after wafer production and polishing. If wafers are not baked then a thin (tens of nms) undesired pSi layer of unknown porosity would exist at the surface of the designed pSi structure after etching due to this diffused hydrogen-rich layer.[67] This is evident in the observed Fabry-Perot optical spectrum obtained from pSi layers. The presence of a thin oxide layer on the surface of a pSi sample will be observed as a wider fringe modulation superimposed on the tighter optical fringes seen from the pSi layer itself. Due to oxidation of the wafer surface during baking, the wafer is then dipped in HF to remove any oxide before etching to avoid a poor electrical contact with the electrode.

The etching current was controlled by a Keithley current source run through LabView 8.2.1 where the current profiles were chosen depending on the type of pSi structure desired. The Si wafer has a pre-defined resistivity and the known surface area A of Si in contact with the electrolyte means that in order to control the porosities of the

samples, the voltage is varied to obtain the desired current densities *J* to break more or less Si – Si bonds for the desired porosities i.e. the resistivity of the Si wafer is fixed and the voltage is dynamic to control the current *I*. Equation (4.1) gives the current density values for current and etch area. Note that once etching begins the resistivity of the Si wafer will change due to the presence of the pSi regions. Typical current values were in the range of 500 - 800 mA where increasing the current lead to a larger number of Si –Si bonds broken and a higher resulting porosity and etch rate of the fabricated pSi region. This is due to thinner depletion regions where there is a higher density of holes so the pore walls develop giving rise to denser pore growth. Floating pSi layers can be obtained by detaching the porous layer from the substrate via a large end current above a critical value at ~ 900 mA which is in the electro-polishing regime. Porosities typically in the range of 55 – 75 % have been used in this study as this region gives the greatest mechanical stability of pSi multilayers due the mismatch between layers of high and low porosity. The higher etching rates at these current values also give reasonable etching times for sample fabrication.

$$J\ (\text{mA cm}^{-2}) = I\ (\text{mA}) / A\ (\text{cm}^2) \quad (4.1)$$

In order to etch the desired porosities an etch calibration must be performed. This involved etching single pSi layers onto single-side polished (SSP) Si wafers with a resistivity of 1 - 5 mΩ cm (p++). Current values from 500 – 800 mA were run to produce twelve different calibration samples between 30 and 70 microns in thickness. The single pSi layers were cleaved to obtain a cross-section of the layer for characterisation by SEM which gave a layer thickness measurement. Knowing the time of the etch run combined with the thickness measurement enables the etch rate as a function of current to be obtained. The etch rate calibration curve is shown in figure 4.8 (a). This is needed to etch layers of a specific thickness. The etch rate increases with the current value used and the time resolution for etching is 0.5 ns. Note that for the fabrication of pSi multilayers there was the inclusion of ‘etch stops’ or ‘etch breaks’ where the current is stopped to stop the etching of the Si wafer and to allow for the HF to be refreshed.[68] This is discussed in more detail later in this chapter since etch breaks are important to prevent porosity and thickness drift through the layers.[69]

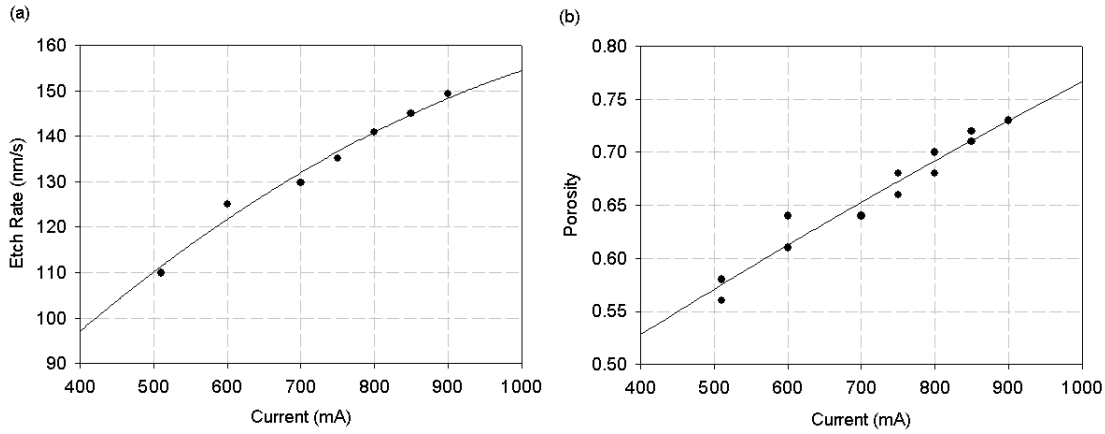

Figure 4.8 Calibration curves for heavily boron doped SSP Si wafers etched in the [100] crystallographic direction for wafers with resistivity of 1 – 5 mΩ cm with best fit through data for (a) etch rate and (b) porosity as a function of the current.

The R^2 fit values for the above calibration curves are above 0.95. In the normal etching regime there should be 2 charge carriers exchanged per dissolved Si atom (valence). Using the calibration curves this can be checked and indeed this is found to be the case.[70] The error introduced to these calibration curves will depend on a few factors such as the HF concentration, the temperature at which the etch is performed and on the resistivity of the Si wafers used. For the pSi etched in this fabrication it was possible to obtain a porosity of the layer within ± 5 % of the desired porosity and the layer thickness well within ± 100 nm of the desired layer thickness. These error values are based on experience using the set-up described; however, if a tighter control on the porosity and layer thickness was required then more stringent fabrication conditions can be used. For example, the temperature of the etch could be controlled to avoid temperature fluctuations throughout the year between winter and summer and also higher specification Si wafers could be used to avoid deviations in the resistivity between the doped wafers. The HF concentration could also be kept more stable by using a fresh HF mix on every single sample instead of each batch of samples during one fabrication session.

Also performed on each single pSi calibration layer was an optical characterisation by means of an interferometer measurement as described in section 5.2. This was used in

conjunction with an effective medium approximation (EMA), discussed in chapter 5, to calculate the porosity of the pSi layer etched. The current-porosity calibration curve is shown in figure 4.8 (b) where the porosity obtained increases with current value. For thicker samples and high porosity samples > 85 % the interlinked silicon nano-bridges between pores can crack during the drying process due to the large capillary stresses as HF solution evaporates from the pores. In order to prevent the structural change of the fabricated network of silicon, pentane drying can be used as it has a lower surface tension and this helps to avoid cracking.

Depending on the conditions under which samples are stored after etching, aging of samples caused by oxidation within the pores and on the nanocrystal surface have been observed in some studies where the presence of SiO_2 modifies the surface chemistry of the pSi and leads to changes in the optical response of the samples, for example with the refractive index becoming modified or the intensity of luminescence changing.[71] Aging effects seen in pSi samples can be reduced by dipping the pSi into HF to refresh the samples by reducing the oxidised layers. In terms of optical applications, the effective refractive index controls the optical response of the samples but for acoustic applications it is the acoustic impedance that controls the acoustic response. The effective refractive index ratio (at 1 μm wavelength) of Si (3.5) to SiO_2 (1.5) is 2.3. However, for acoustic applications the acoustic impedance is important and the acoustic impedance of oxidised Si (SiO_2) compared to Si does not change much despite being slightly modified where the ratio of the acoustic impedance of Si (19.64 MRayl) to fused quartz SiO_2 (13.13 MRayl)[72] is 1.5. Aging effects of pSi layers have not been observed during acoustic transmission measurement with the samples in this investigation.

4.2 Fabrication of Porous Silicon Multilayers

Many types of all-Si multilayers for optical applications have previously been studied by many groups where pSi Bragg mirrors and rugate filter[73, 74] multilayers have been used in dichroic filters and interference filters, chemical sensors[75, 76, 77] and optical switches among others. As mentioned in chapter 1, some methods of production of multilayered structures involve fabrication by gradually building up the layers using two separate materials in alternating layers. For example, making Bragg mirrors using Si/Ge layers or GaAs/AlAs alternating layers.[78, 79] For the deposition production method the Bragg mirror fabrication technique is simpler compared to the fabrication of rugate filters. For a Bragg mirror the two materials can easily be deposited separately but for a rugate filter a mix of the two materials is needed where the ratio of one material to another changes with the deposition time. A Bragg mirror consists of alternating layers of material as previously described in chapter 1 and if a cross-section through the mirror is taken there is a stepped material profile such as that shown in chapter 1, figure 1.1 (right). The two materials are chosen so that their acoustic impedances are mismatched and this gives a stepped acoustic impedance profile through the layers (like a square-wave profile). The acoustic impedance profile is very important when designing multilayers for acoustic applications because the acoustic impedance profile determines the acoustic response of the multilayer. A rugate filter is a multilayered structure similar to a Bragg mirror but instead of a square-wave acoustic impedance profile it has a sinusoidal acoustic impedance profile. The effect of this is to modify the transmission stopbands seen in the frequency domain in comparison to that seen for a Bragg mirror. Fabricating a rugate filter using deposition techniques will require a feedback system to continually monitor and modify the proportions of each material deposited so as to construct a multilayer with a sinusoidal acoustic impedance profile. Optical rugate filters based on pSi have been fabricated using electrochemical etching by sinusoidally varying the etch current during fabrication.[80]

The main advantage of pSi material is that there is no fixed acoustic impedance. The acoustic impedance mismatch between layers is governed by the porosity step variation. The acoustic impedance mismatch affects the number of layers required for

pSi material because the reflectance (or transmittance) of the multilayer is dependent on the acoustic impedance of the individual layers. For example, for a CVD multilayer using a Mo layer with impedance 63.1 MRayls and a SiO_2 layer with impedance 13.1 MRayls, the reflectance value is 0.43. For a pSi multilayer with a layer of porosity 30% with impedance 11 MRayls and a layer of porosity 75% with impedance 2 MRayls, the reflectance value is 0.48. The pSi based multilayers can be tailored to have a desired reflectance value which is perhaps more flexible given the range of porosities and impedances available than the multilayers made by CVD using two fixed materials.

Optical rugate filters based on pSi have already been modelled by Southwell and fabricated[81, 82] but acoustic rugate filters based on pSi have not previously been studied and fabricated. A theoretical investigation into rugate filters based on pSi for acoustic applications was done by Reinhardt and Snow.[83] The first acoustic rugate filters using a sinusoidal acoustic impedance profile have been made in this study. The electrochemical etching method allows for easy modifications to the material density profile, and hence acoustic impedance profile of the multilayers.

4.2.1 Bragg Mirrors

The multilayered structures fabricated for this acoustic study are Bragg mirrors, rugate filters and microcavities. For the fabrication of pSi Bragg mirrors and microcavities a square-wave current density profile was used where the etch current was alternated between a minimum J_A and maximum J_B current density value to create AB pairs of layers. The AB pairs of layers will have a porosity p_1 and thickness d_1 in layer A and a porosity p_2 and thickness d_2 in layer B. A cross-section through an all-Si Bragg mirror is shown in figure 4.9 where the step in material density is achieved using layers of different porosity of Si to obtain a different material density of Si in each layer. The higher current density leads to the fabrication of a higher porosity layer than that obtained when the lower current density is used so that the pSi etched under the maximum current regimes correspond to the high porosity layers and vice versa. The stepped square-wave current profiles give rise to a stepped porosity profile with a porosity change across each AB layer interface. The thickness of the

interface across which the porosity will change is negligible in comparison to the layer thickness. See section 6.4 for discussions of the interface quality. It is noted that the transition of porosity seen in the SEM image of figure 4.9 is sharper on one side of the dark layer of high porosity. The etch direction as seen here is from the bottom left corner into the substrate at the top right corner and layers were etched starting with low porosity (light layer) then high porosity (dark layer) layers so that the Bragg mirror terminates on a high porosity layer at the substrate. Going from a high porosity layer to a lower porosity layer seems to give a higher quality interface than vice versa. The interface between the layers of high and low porosity is the transition region where the step in porosity level occurs. The pore diameter will increase for higher porosities and the side-branching longways will increase.

The acoustic impedance is a function of the porosity of the layer so a square-wave current density used to create a square-wave porosity profile leads to a square-wave acoustic impedance profile. The etching time run at each current density determines the thickness of each porosity layer and the current density profile as a function of etching time as shown in figure 4.9 determines the overall multilayer appearance. This creates pairs of AB layers for a set number of repeats *N*.

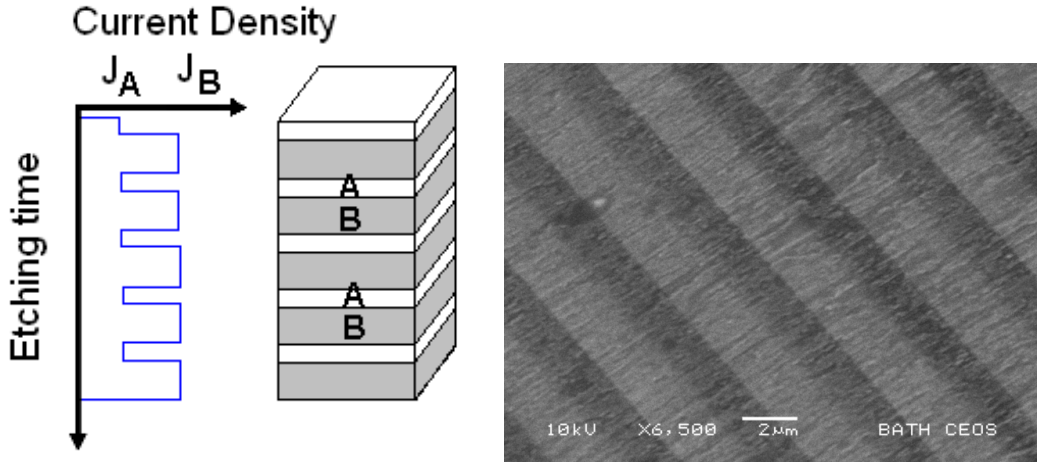

Figure 4.9 Current density profile used to fabricate Bragg mirrors alongside an SEM contrast image of the alternating layers of high (dark) and low (light) porosity. The SEM scale shown is for 2 µm for sample #50. Lower porosity layers have higher electron density and so show up as lighter regions.

4.2.2 Rugate Filters

In contrast to the square-wave porosity profiles of the Bragg mirrors, the pSi rugate filters have sinusoidally varying porosity profiles. The rugate filters have been fabricated using stepped current-time profiles that is close to that of a smoothly varying function as described by figure 4.10 (a). This shows one cycle corresponding to one AB layer in the stack for *N=1*. Each half-sinusoidal cycle corresponds to layer A or B and was split into 8 more individual sub-layers where the physical thickness of the overall layer A or B was controlled by the etch time in the eight sub-layers.[73] Modelling showed this to be a sufficient number of steps in current density to fabricate a sinusoidal variation in impedance such that a rugate mirror response equivalent to a sine profile was achieved. For an optical rugate filter the sinusoidal modulation is performed on the refractive index profile of the layers as $n=n_{av}+\Delta n sin(4\pi OT/\lambda)$ where n_{av} is the average refactive index of the mirror, Δn is the difference between the high and low refractive index layers and OT is the optical thickness at a wavelength λ.[84] A similar approach is used for the sinusoidal modulation for acoustic rugate filters where the modulation is performed on the acoustic impedance profile of the layers. This was shown previously in figure 3.9 and will be described in detail in chapter 6. Increasing the number of sub-layers makes the mirror more 'rugate-like' but 8 sub-layers is a good approximation.

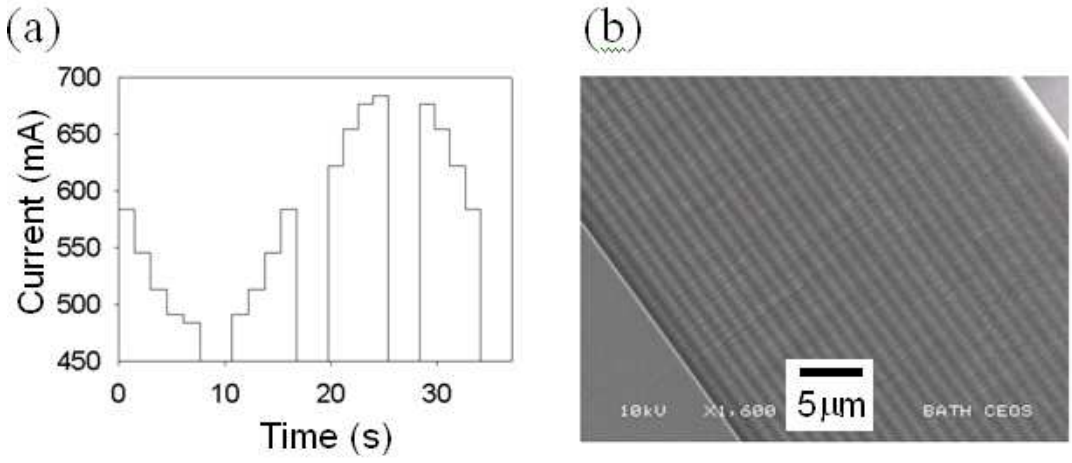

Figure 4.10 (a) Current-time etch profile of one cycle used for sample #52 and (b) SEM image of pSi rugate filter sample #52.

The gaps in the cycle are where etch breaks of 3 s were added every $\pi/2$ in the sinusoidal modulation for this particular rugate sample shown by the SEM in figure 4.10 (b). Note that one sinusoidal cycle used in the rugate 'version' of a Bragg mirror corresponds one AB layer of the Bragg mirror. Looking at the sinusoidal cycle in figure 4.10 (a) the first half from 0 up to π corresponds to the A layer and the second half of one cycle from π to 2π corresponds to the B layer.

The following SEM image of figure 4.11 shows an enlarged section of sample #52 for five full etch cycles of 'AB' layers at the substrate side of the rugate filter and it can be seen that each cycle appears to be split into a further four layers where the etch breaks have been used. The overall appearance of the rugate filter is similar to that seen for the Bragg mirrors however the porosity change through one cycle is gradual.

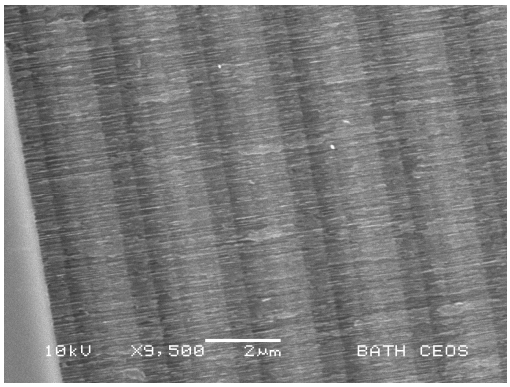

Figure 4.11 Enlarged section of layers next to the substrate for rugate sample #52.

4.2.3 Fabry-Pérot Filters (Microcavities)

Fabry-Perot filters or microcavities are multilayered mirrors that allow a transmission peak within a stopband. They are based on a Bragg mirror located either side of a defect layer. For optical microcavities the thickness of this defect layer is $\sim\lambda/2$ thick and gives rise to the transmission peak inside the stopband. For acoustic microcavities the defect layer is $\sim 2\tau$ where it takes the waves twice as long to traverse the defect layer as it does each single layer in the Bragg mirror. An example of a microcavity is

shown in figure 4.12 where the Bragg mirror layers of alternating high and low porosities can be seen either side of the defect layer in between the two Bragg mirrors.

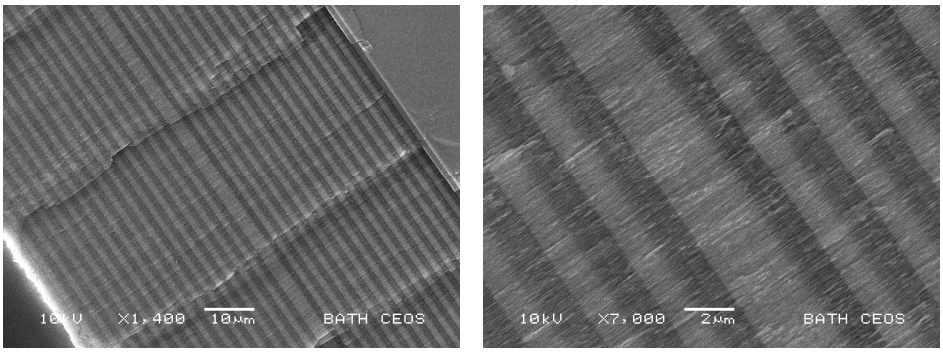

Figure 4.12 SEM image of (left) pSi microcavity on bulk Si substrate and (right) defect layer in pSi microcavity for sample # 41.

4.3 Effect of the Inclusion of Etch Breaks

In contrast to pSi layers used for optical applications in the 400 – 1600 nm range where the pSi layers are typically of the order of nanometers in thickness,[85] the pSi layers fabricated for the acoustic investigations in the 1 GHz region performed in this study are typically of the order of microns thick. For thicker pSi layers care needs to be taken during fabrication as the likelihood of the pSi layer detaching due to the build up of hydrogen within the pores increases with layer thickness. To prevent this build up of hydrogen within the pSi layer, etching breaks can be used where no current is applied and electrochemical etching of the Si wafer stops, allowing the excess hydrogen to escape the pores at the surface. The inclusion of etching breaks is also important in maintaining the desired HF concentration at the etch front to avoid HF depletion at the pore tips.[54] With HF depletion there is a slower etch rate leading to a thinner layer with higher porosity as shown by the Bragg mirror in figure 4.13 where thinner layers towards the substrate side of the mirror are visible. The etch rate will change as the HF concentration drops so that the thickness of the pSi layer is smaller than desired and the drop in HF concentration therefore also results in porosity drift to higher porosities. For the Bragg mirror shown in figure 4.13, the high porosity layers (dark) at the top of the mirror are 1.41 μm and chirped at the bottom of

the mirror with 0.95 μm. This is a 33 % change across the entire Bragg mirror. The low porosity layers (light) at the top of the mirror are 1.54 μm and at the bottom of the mirror are 1.42 μm giving an 8 % change in thickness across the Bragg mirror. The inclusion of etch breaks are important when fabricating multilayers based on pSi.

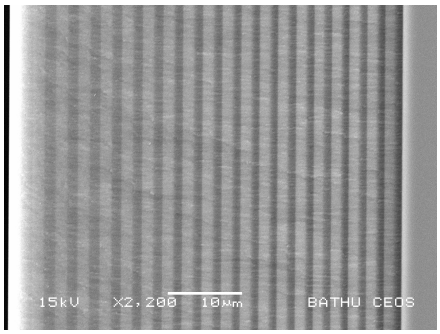

Figure 4.13 Bragg mirror sample #1 etched without etch breaks showing HF depletion throughout the layers. Layers become thinner towards the substrate (right hand side) and darker (due to lower electron density) as the porosity increases and the mirror becomes chirped.

Maintaining the desired porosity and etch rate is important to thicker specimens as the deeper the layer the stronger the effect of the HF concentration change because the HF is consumed in the pores and takes longer to refresh. Studies of the change in etch rate and microstructure with depth have been done by Thonissen et al.[69] on pSi layers formed on p+ substrates in the [100] direction. It was found that the change in HF concentration for p+ and p++ Si is the dominant effect on gradient change and that gradients are not caused by chemical etching at locations away from the etch front. Thonissen et al. give a solution to porosity gradient changes (and morphology) by modifying the current density and etch time with depth accordingly to obtain homogeneous layers. Since there are so many varying parameters with etch conditions and resulting morphology and porosity, etching breaks were used in this study to prevent the depletion of HF and therefore keep the porosity as constant as possible with depth.

The length of the etch breaks is important to the post etching of the walls and etch breaks of 3 s were found to be sufficient to minimise chirp on the layers. The effect of

the inclusion of etch breaks is studied later on in section 7.5 since the location of the etch break in the etch run can affect the overall balance of the mirrors and therefore the frequency response. Since the porosity of the layers in pSi multilayers depend upon the etching conditions and HF concentration, when etch breaks are included there is a slight change in the porosity at the etch break locations which have been shown to affect the stopbands measured in chapter 7.

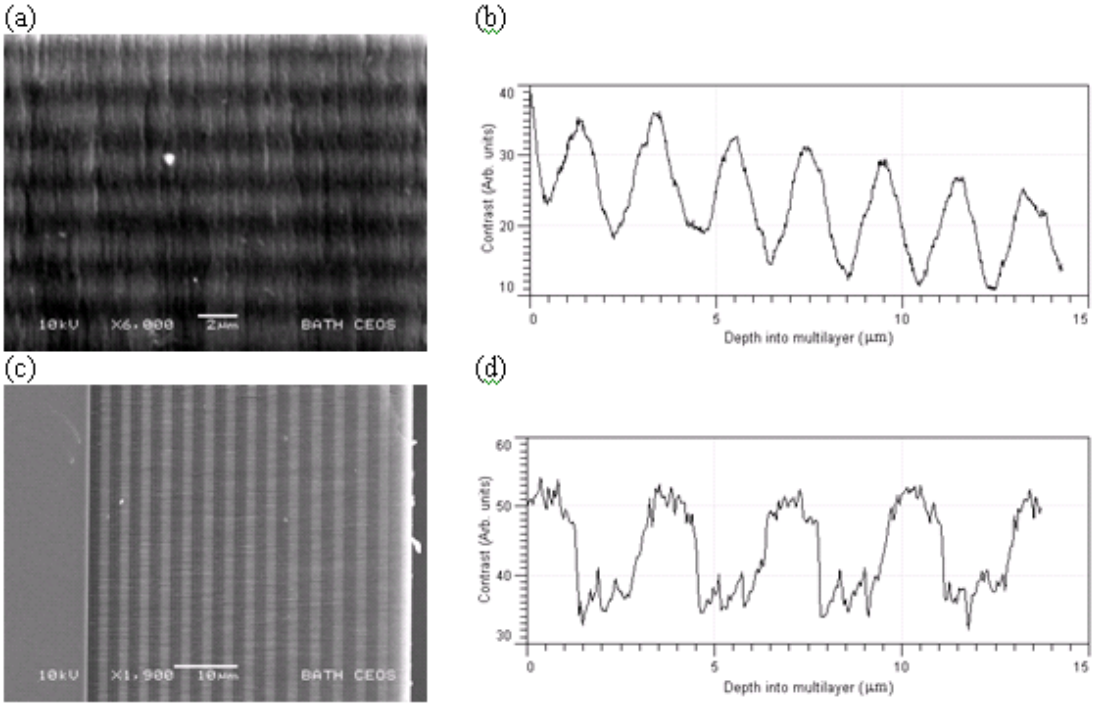

Figure 4.14 (a) SEM image of a pSi rugate filter sample #23 etched with 32 sub-layers and (c) pSi Bragg mirror sample #42 (b) SEM contrast profile of the pSi rugate filter of (a) showing filter period thickness of 2.14 μm and (d) Bragg mirror of (c) sample #42.

The multilayered Bragg mirrors and rugate filters have been characterised by SEM imaging as shown in figure 4.14 (a) and (c) to determine layer thicknesses. It can be seen that the contrast of the SEM images change from light to dark for different porosity layers. This is due to the electron density of the varying porosity material within the multilayers and this can be used to extract a contrast profile analogous to the porosity profile as shown in figures 4.14 (b) and (d). Note that the rugate sample in (a) was fabricated without etch breaks and there is a gradient on the profile in (b).

The Bragg mirror in (c) was etched using two 3 s etch stops within each layer A and B, in addition to a 3 s etch stop each time the current density stepped the porosity up or down. The profile shown in (d) is not chirped. The effect of the etch stops in the etch cycle of the Bragg mirror are evident from the small peaks seen in the SEM contrast profile of 4.14 (d). The darker regions of the SEM image relate to lower numbers on the contrast scale and vice versa. The dark regions correspond to layers with high porosity and appear to be more influenced by the inclusion of etch breaks compared to the layers with low porosity because larger peaks can be seen in the contrast profile for the dark layers This is consistent with the 33 % chirp for high porosity layers for the Bragg mirror shown in figure 4.13 compared with only an 8 % chirp for the lower porosity layers. The larger etch break peaks for the high porosity layers in figure 4.14 (d) may be due to a heavier weighting of chirp on higher porosities when etch breaks are omitted so when etch breaks are included the porosity change is more noticeable. Note that the contrast cross-section of the pSi multilayer was taken from left to right of the SEM image and since the pSi mirrors are etched top-down the right hand side of the 'etch peaks' displayed in the high porosity layers in the contrast profile are the 3 s etch breaks. When the etch breaks end the porosity is lower (higher points of the contrast scale) indicating that they are needed to prevent porosity chirp. When the etch is resumed the porosity again drifts. Despite being aware of the porosity drift without etch breaks the rate of the porosity drift is not known and will vary depending on how porous each layer is. However, it is important to be aware of this effect as it does influence the acoustic response of mirrors with thicker layers. There is an overall gradient to the contrast profile of 4.14 (b) but it is difficult to say whether this gradient could be due to a porosity gradient across the multilayer from chirping since etch breaks were not included. This is because the surface of this particular wafer shown in 4.14 (a) had some charging with respect to the conductive substrate which would introduce an artificial gradient to the top layers of the contrast profile.

The following SEM image of figure 4.15 (a) of a Bragg mirror shows the evidence of etch breaks included during the fabrication process and can be seen in each of the layers within the multilayers where the etch breaks are more prominent in the dark layers. Figure 4.15 (b) shows the top four AB layers where there is less evidence of a

porosity chirp than the bottom layers; this is highlighted in the figure 4.15 (c) where the etch peaks appear larger for the AB layers next to the substrate.

(a) (b)

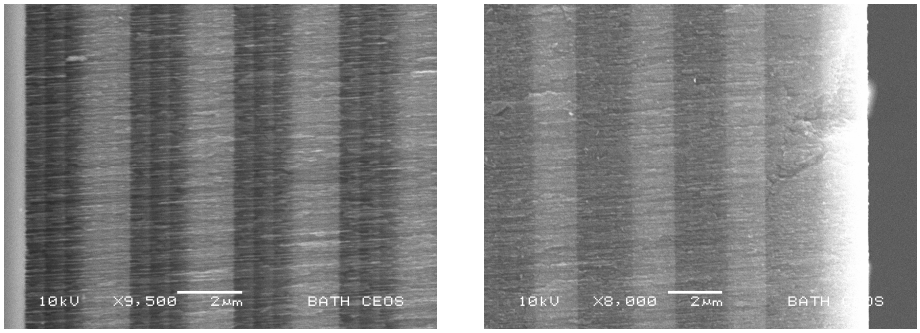

(c)

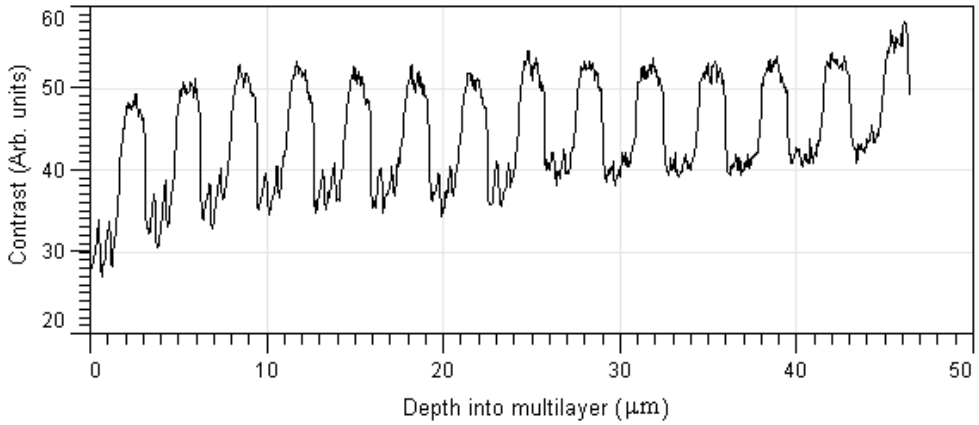

Figure 4.15 (a) Bottom and (b) top 4 pairs of AB layers of sample #42 and (c) contrast profile taken through the Bragg mirror sample #42 also shown in figure 4.14(c).

This chapter has discussed the fabrication of pSi multilayers in detail. The electrochemical etching technique has been used to fabricate pSi Bragg mirrors, rugate filters and microcavities in the [100] Si wafer direction. Etching calibration curves for etch rate and porosity are given for the p++ doped Si wafers used in this investigation. A study on the effect of the inclusion of etching breaks has been discussed, particularly the effect that etch breaks have on minimising chirp in a pSi Bragg mirror designed for acoustic applications which have layers that are typically one micron thick. The next chapter will discuss the techniques used to characterise the pSi samples that have been fabricated.

5 Characterisation of Porous Silicon Layers

This chapter mainly focuses on the characterisation of single pSi layers and this is later extended to characterise multilayered pSi. The single layer pSi samples that have been fabricated are characterised by optical and acoustic measurements to deduce the porosity and thickness of the pSi layer fabricated. SEM imaging has been used for accurate layer thickness measurements and the AFM was used to give surface roughness measurements of the pSi. The multilayers were also characterised using optical and acoustic measurements with SEM imaging giving layer thicknesses. PSi is a dielectric material and using the refractive index obtained from optical measurements it is possible to determine the porosity from EMA theories. Acoustic measurements are then used to find the acoustic velocity through single porous layers so that the acoustic impedance dependence on porosity can be known. This information then enables multilayered pSi to be fabricated with desired acoustic responses such as fabrication of a pSi multilayer with a stopband located at 1 GHz.

5.1 Layer Thickness and Porosity

The porosity of single layers of pSi can be determined by the gravimetric method or via optical interference measurements. For both methods the thickness of the porous layer must be known. The gravimetric method is simple and not very precise because it relies on knowing the mass of the Si wafer before, m_1 and after, m_2 etching and also the volume V_{total} of the etched region. Due to the small mass of thinner pSi layers this method is not very accurate and works best for very thick layers etched over a large surface area although it does give a rough estimate of the porosity for thinner layers.

An accurate method used to measure the thickness of the pSi layers is using SEM imaging but this is a destructive technique as the sample needs to be cleaved in order to measure the thickness of the layer viewing the cross-section through the sample. An optical microscope can be used to see the layer thickness against a length scale however SEM imaging is the method chosen during this study to obtain an accurate measurement of layer thickness. The porosity of the porous layer p is defined as the volume fraction of air V_{air} to Si within the layer volume and is given by equation (5.1)

below and can also be expressed as (5.2) where $V_{c\text{-}Si}$ is the volume of Si within the layer. The air-filled pores are surrounded by the remaining Si matrix and the pores can be infiltrated with another medium such as ethanol.

$$p = \frac{V_{air}}{V_{total}} \tag{5.1}$$

$$(1-p) = \frac{V_{c-Si}}{V_{total}} \tag{5.2}$$

$$p_{grav} = \frac{4(m_1 - m_2)}{\rho_0 \pi D^2 d} \tag{5.3}$$

The gravimetric porosity p_{grav} is shown in equation (5.3) where ρ_0 is the density of bulk Si and has a value of 2.329 g cm^{-3}, D is the diameter of the etched area and d is the thickness of the etched layer that is measured by SEM. Whereas this method is fine for single layers it is impossible to separate the porosities of each layer within a multilayered stack and so optical interference measurements have been chosen to characterise single and multilayered pSi.

5.2 Effective Refractive Index of Single Porous Silicon Layers

The pores of the pSi filled with air surrounded by a matrix of Si are described as an effective medium. The refractive indices of air and Si are known for each separate material but the effective refractive index of the new effective medium must be found to describe the porous nature of the material. The shape and size of the voids in the Si matrix determine its optical properties, the filling medium inside the pores also affects the effective refractive index. The pSi samples fabricated have pores with ~ 20 nm diameter and make up the photonic or phononic crystal which is the periodic structure. For pSi layers used in this investigation the pores appear to be column-like

along the [100] crystallographic direction and this is seen in SEM imaging. When viewed from above this periodic structure looks different from when viewed from the side and hence is anisotropic. The most accurate method of obtaining the effective refractive index of the [100] pSi single layers is from optical measurements using a Fabry-Perot set-up as shown in figure 5.1.

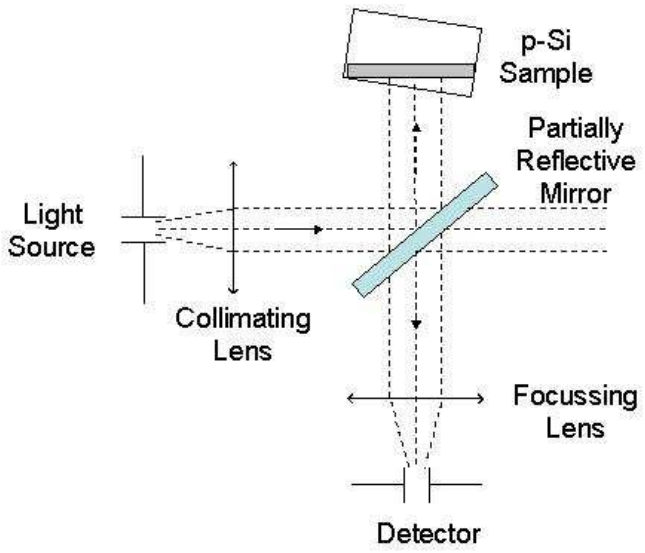

Figure 5.1 Optical Fabry-Perot set-up for measuring the effective refractive index of the porous layer.

The optical properties of the fabricated porous layers are determined by free-space optical interferometry (figure 5.1). White light from a tungsten filament lamp is collimated using a lens with focal length of 20 cm and passed through a 50% reflective mirror before the light is incident upon the porous layer on the bulk Si wafer. Interference takes place within the porous silicon layer and reflected light is focused using another 20cm lens onto the nitrogen-cooled CCD detector within the spectrometer. The wavelengths reflected from the sample that are measured range between 900-1600nm.

The reflected interference pattern observed (figure 5.2) gives the reflectance at each wavelength and shows a series of peaks and troughs that can be studied with the spacing between the Fabry-Perot fringes used to determine the product *nd* where *n* is

the effective refractive index of the porous layer and *d* is the physical layer thickness or the physical distance between the two reflecting interfaces. Since *d* is known, then the effective refractive index can be deduced.

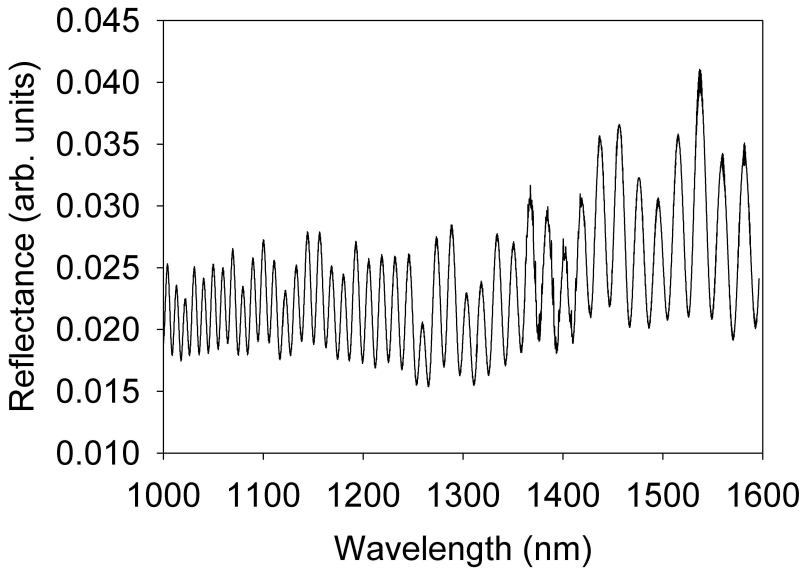

Figure 5.2 Fabry-Perot interference pattern seen from a single layered pSi sample with a porosity of 70%.

The porous layer of the sample acts as a Fabry-Perot etalon with light reflected from the air/pSi and pSi/cSi interfaces (figure 5.3). The reflectivity response of the porous layer depends upon the difference in the refractive index at the layer interfaces. Independently measuring the layer thickness *d* by SEM enables the refractive index of the porous layer to be determined. The porous layer on the bulk cSi substrate acts as an etalon since light incident through air on the surface of the porous layer is reflected at this boundary and also at the second boundary with the bulk cSi substrate. The refractive index of air and Si is known, as is the thickness of the porous layer through SEM measurements so the only unknown parameter is the effective refractive index of the porous layer itself.

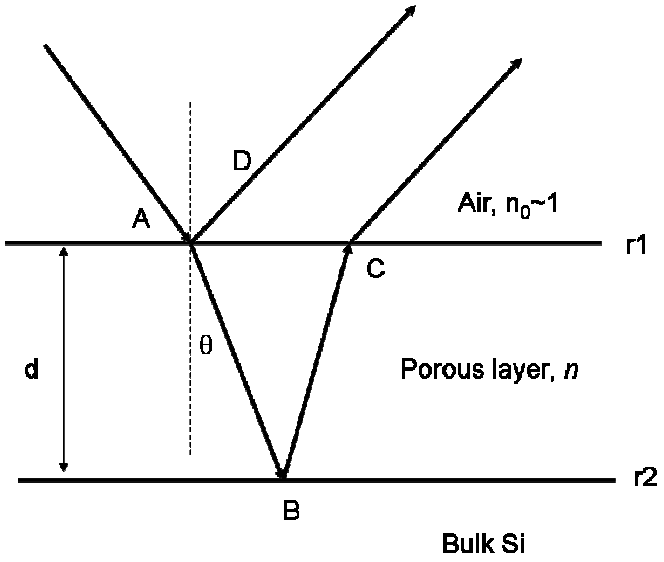

Figure 5.3 Single pSi layer on bulk cSi substrate acting as a Fabry-Perot interferometer.

A Fabry-Perot etalon creates an interference pattern by the division of the amplitude of an incident beam by multiple reflections between two highly reflective mirrors, these being the boundary of the porous layer with air and the substrate. In order to study the interference effects the optical path difference between reflected waves must be known. The reflection coefficient of a Fabry-Perot etalon is given by equation (5.4) where r_1 is the reflection coefficient of the optical waves at the air/pSi interface, r_2 is the reflection coefficient at the pSi/cSi substrate interface and δ is the phase difference between the reflected waves. The reflectance of the etalon is given by the square of the reflection coefficient modulus of equation (5.5). For a single pSi layer with around 70 % porosity the reflectance R ~ 30 %.

$$r = \frac{r_1 + r_2 e^{-2i\delta}}{1 + r_1 r_2 e^{-2i\delta}} \tag{5.4}$$

$$R = \frac{r_1^2 + r_2^2 + 2r_1 r_2 \cos 2\delta}{1 + r_1^2 r_2^2 + 2r_1 r_2 \cos 2\delta} \tag{5.5}$$

The optical path difference d_{opt} for light at the angle of incidence θ upon the layer of thickness d (note that θ=0° for our case) is given by (5.6) and the phase difference δ is given by (5.7) where n is the optical effective refractive index of the porous layer, d is the thickness of the layer and λ is the optical wavelength of the incident light. The path delay in figure 5.3 is given by $\Delta l=2nAB-n_0AD$ which is equal to $2ndcos\theta$.

$$d_{opt}=2ndcos\theta \qquad (5.6)$$

$$\delta=(4\pi ndcos\theta/\lambda) \qquad (5.7)$$

For maxima, $\delta=2m\pi$

For minima, $\delta=(2m-1)\pi$

If the incident wave is normal to the Fabry-Perot etalon then equating these expressions for the phase difference gives the positions of the maxima and minima in the interference spectrum. There is constructive interference λ_c at the maxima and destructive interference λ_d at the minima.

maxima at λ_c $\lambda_c=4nd/(2m-1)$ (5.8)

minima at λ_d $\lambda_d=2nd/m$ for integer m=0, 1, 2, ... (5.9)

Therefore the optical path difference nd can be obtained from the position of two closest extrema using (5.10) or equivalently from two consecutive maxima or minima using (5.11), the optical path length for samples in this investigation are found with (5.11).

$$nd=\frac{1}{4}\frac{\lambda_c\lambda_d}{\lambda_d-\lambda_c} \qquad (5.10)$$

$$nd=\frac{1}{2}\frac{\lambda_c\lambda_{c+1}}{\lambda_c-\lambda_{c+1}} \qquad (5.11)$$

Once the reflected interference pattern has been studied and *nd* has been found for the porous layer, the SEM measurement of the layer thickness *d* enables the effective refractive index of the porous layer to be determined. An effective medium approximation (EMA) can then be used to find the porosity of the porous layer and compared to the porosity found using the gravimetric measurement approach if necessary. Experimental measurements are compared against simulated results to help deduce the porosity of the porous layer based on the effective refractive index found and is described later in section 5.3.

Dispersion describes a material property which causes different wavelengths to travel at different velocities through the material. Si shows normal dispersion in the infra-red region of the spectra (red light travels faster than blue through the material). The optical measurements that have been taken for the pSi multilayers on the Si substrate are in the infra-red region and are obviously inclusive of dispersion. Therefore the programs used to model the pSi multilayers must also include dispersion properties. The Herzberger-Salzberg (H-S) dispersion equation (5.12) has been used to model this effect.

$$n = a + bL + cL^2 + d\lambda^2 + e\lambda^4 \tag{5.12}$$

$$L = 1 \Big/ \left(\lambda^2 - \lambda_0^2\right) \tag{5.13}$$

The H-S dispersion equation is for glass and other optical materials extended into the far infra-red[86] where λ is the wavelength and *a, b, c, d* and *e* are the H-S coefficients which are constant for each material. These constants for Si are a=3.41696, b=0.138497, c=0.013924, d=-0.0000209 and e=0.000000148.[87] The mean value of the position of the absorption band in the ultraviolet (UV) is given by λ_0 and is different for different glasses. It has been found that a value of λ_0^2=0.028μm^2 gives a good agreement of the dispersion relation over the range of 430nm < λ < 1700 nm. The dispersion relation is only applicable to wavelengths above ~400 nm due to the high level of absorption of optical materials in the UV region. For any glass the dispersion curve can be calculated using the dispersion relation for the real refractive index of

the material using the five H-S coefficients *a*, *b*, *c*, *d* and *e*. The refractive index of the cSi substrate is n=3.5 at a wavelength of 1 μm.

In a model without dispersion the refractive index would be expected to be constant, however in the infra-red region the refractive index is relatively constant as the incident wavelength is far from the absorption peaks of the material. The dispersion, or change in refractive index with energy becomes more significant towards higher energies approaching the visible region of the spectrum where the material has loss due to resonances within the material. This can be seen from the curve k(E) for the imaginary part of refractive index in figure 5.4 below. The graph shows the complex refractive index where n(E) is the real part of the index and k(E) is the imaginary part of the index as a function of photon energy.

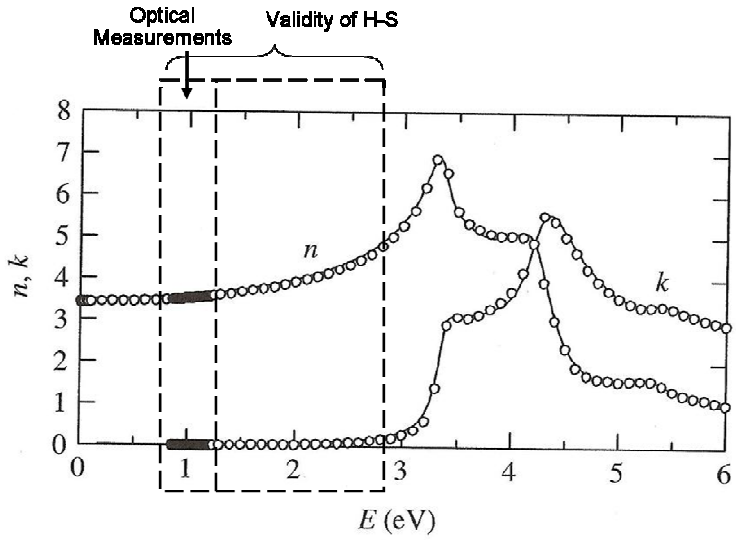

Figure 5.4 Real n(E) and imaginary k(E) parts of the refractive index of Si showing the dispersion curves for this material.[88]

5.3 Effective Medium Approximations

Effective medium approximation (EMA) theories give an effective refractive index for a porous medium that has features smaller than the wavelength of light.[89] It is useful to obtain the porosity of the pSi layers to know the density of the layer and hence the acoustic impedance Z for designing acoustic filters based on pSi. The EMAs use the dielectric constant of the two or more materials to determine the effective dielectric constant and from this the effective refractive index and porosity.

The dielectric constants of the two separate materials must be known to find the effective dielectric constant of the materials together. The dielectric constants ε are real since $\varepsilon = n^2 - k_{ex}^2$ where n is the refractive index of the material and where k_{ex} is the extinction coefficient, defined as the fraction of light lost due to scattering and absorbtion (the conversion of light to heat within a semi-transparent substance) per unit distance through the participating material. The refractive index is complex so that $\tilde{n} = n - ik_{ex}$ and the dielectric constant is simply the square of this complex refractive index. For wavelengths in the infra-red region of the spectrum the extinction coefficient is negligible compared to n for $\lambda < 800$ nm, $k_{ex} \approx 0$ and $n^2 >> k_{ex}^2$ so that ε can be approximated to $\varepsilon \approx n^2$ for pure Si. Doping of a dielectric material with impurities will modify its relative dielectric constant so as to control the refractive index of the material. The Hertzberger-Salzberg coefficients for pure Si for n and k_{ex} have been used to compute the effective dielectric constant of pSi using the relation shown below where the extinction coefficient for pSi k_{ex}^{pSi} has a linear relationship with porosity.

$$k_{ex}^{pSi} \approx (1-p)k_{ex}^{Si} \tag{5.14}$$

The linear relationship of the pSi extinction coefficient with porosity has been assumed because the extinction coefficient is proportional to the absorption coefficient α due to loss mechanisms such as scattering, which is given at a known wavelength λ through a given length x of material i.e. $I = I_0 e^{-\alpha x}$ where I is intensity.

$$k_{ex} = \frac{\alpha\lambda}{4\pi} \tag{5.15}$$

The Bruggeman, Looyenga and Maxwell-Garnett EMAs describe a composite mixture in terms of a spatially homogeneous dielectric response. Inclusion clustering is neglected as it is assumed that the inclusions are far from each other so can be treated as individual inclusions in the host material. The approaches of using EMAs is to consider the averaging effects of the inclusion in the host material, this is our approach used, or to consider the polarizability effects by ordered lattice calculations. The Bruggeman theory has been chosen over others because this has given the best fit to collected historical data for the dielectric constant of solid mixtures of metal spheres in an insulating host medium. The assumptions are that the inclusions are spherical in nature, that they are mono-dispersed and have equal particle size. Real materials will have inclusions of unequal size. Models taking the range of particle sizes and clustering into account can be used and give better fits up to ~ 40% porosity compared to the symmetric Bruggeman and Maxwell-Garnett approximations but are more complicated and have other limitations such as a maximum filling porosity ~ 60% for randomly placed particles. The asymmetric Bruggeman approximation is best for porosities up to ~ 60% which is close to the practical limit for the filling of a host medium.

The *Bruggeman* model is the only model to deal with more than one filling for the pores, where the volume fraction of material *i* inside the porous medium is defined by f_i and the dielectric function of the embedded material is ε_i and the effective dielectric function ε_{eff} is described by equation (5.16).

$$\sum_i f_i \frac{\varepsilon_i - \varepsilon_{eff}}{\varepsilon_i + 2\varepsilon_{eff}} = 0 \tag{5.16}$$

This EMA is the most widely used in the literature to describe porous silicon and is a well-tested model. For air filling within the pores of the porous silicon-matrix the porosity p and the dielectric constant of air ε_{air} describe the effective medium via

equation (5.17). Note that for ethanol filling of the pores the dielectric constant of air ε_{air} should be replaced by the dielectric constant of ethanol ε_{eth} and that it should be assumed that each of the pores are completely filled.

$$p\frac{\varepsilon_{air}-\varepsilon_{eff}}{\varepsilon_{air}+2\varepsilon_{eff}}+(1-p)\frac{\varepsilon_{Si}-\varepsilon_{eff}}{\varepsilon_{Si}+2\varepsilon_{eff}}=0 \qquad (5.17)$$

For $\varepsilon_{eff} \approx n_{eff}^2$ for Si the Bruggeman model can be used to find the effective refractive index n_{eff} of the porous material as a function of porosity i.e. *n(p)* with $n_{air} \approx 1$.

$$p\frac{1-n_{eff}^2}{1+2n_{eff}^2}+(1-p)\frac{n_{Si}^2-n_{eff}^2}{n_{Si}^2+2n_{eff}^2}=0 \qquad (5.18)$$

There is a modified Bruggeman model that considers a set of rotational ellipsoids aligned in the same direction and parallel to the optical axis of an effectively anisotropic medium.[90] This takes the birefringence of pSi into account using a depolarisation factor *L* which corresponds to the void shape, equation (5.19). For the ordinary refractive index n_0 (for TE polarisation, perpendicular to the axis of the cylindrical pores) where L=0.5, and for the extraordinary refractive index n_e (for TM polarisation, parallel to the axis of the cylindrical pores) where L=0.

$$p\frac{1-n_{eff}^2}{n_{eff}^2+L\left(1-n_{eff}^2\right)}+(1-p)\frac{n_{host}^2-n_{eff}^2}{n_{eff}^2+L\left(n_{host}^2-n_{eff}^2\right)}=0 \qquad (5.19)$$

For the *Looyenga* model the effective dielectric function ε_{eff} described by equation (5.20) depends upon the dielectric function of the embedded material or inclusions ε_i and the dielectric function of the matrix or host material ε_h and where *p* is porosity.

$$\varepsilon_{eff}=\left[\left(\varepsilon_i^{1/3}-\varepsilon_h^{1/3}\right)p+\varepsilon_h^{1/3}\right]^3 \qquad (5.20)$$

For the *Maxwell-Garnett* model the embedded material is spherical in shape and has diameters < 10^{-5} cm with two randomly distributed materials. The Maxwell-Garnett analogy of light in metal films[91] uses the effective dielectric function ε_{eff} which is shown to be dependent upon the dielectric constants of the embedded material ε_p and also dependent on the dielectric constant ε_m of the substrate within which they are embedded (matrix material). This model is therefore based on two materials only. The quantity of embedded material affects the effective dielectric function and there is dependence of the effective dielectric function on the size and distance apart of the embedded spheres with the volume fraction of embedded material defined by the parameter f (or porosity).

$$\frac{\varepsilon_{eff} - \varepsilon_m}{\varepsilon_{eff} + 2\varepsilon_m} = f\frac{\varepsilon_p - \varepsilon_m}{\varepsilon_p + 2\varepsilon_m} \tag{5.21}$$

The *Boundary Condition* model is different to the others described since it is modelled by ordered lattice calculations instead of averaging effects like the other models. It is based on a geometric treatment of the continuity of electric fields between the solid skeleton and the filling medium and it reveals the anisotropic behaviour of pSi as shown in figure 5.5. The porosity dependence on effective refractive index for the boundary condition model is different for pSi treated in each direction for (5.22) and (5.23) where n_o and n_e are the ordinary and extraordinary refractive indices in each pore direction and n_{host} is the refractive index of the host material. This model considers a simple structure consisting of square pores in an ordered square lattice for two directions which have the electric field parallel (n_e) and perpendicular (n_o) to the pore walls. The n_o direction is the same as the TE-polarisation and the n_e is the same as the TM-polarisation. Both the material for the host and the filling medium are considered to be isotropic.

$$n_o = \sqrt{(1 - K\beta)n_{host}^2 + K\beta\frac{n_{host}^2}{\beta n_{host}^2 + (1-\beta)}} \tag{5.22}$$

$$n_e = \sqrt{\beta^2 + (1-\beta^2) n_{host}^2} \tag{5.23}$$

where $\beta = \sqrt{p}$ of the porosity p and K are geometrical parameters. For the 'simple' model, $K=1$ and for the complete model K is described by equation (5.24).

$$K = \beta^{1/8} + \frac{2\left(1-\beta^{1/8}\right)}{n_{host}^2\left(n_{host}^2+1\right)} \tag{5.24}$$

A comparison between the EMA models described in this section are shown in figure 5.5 for pSi, where the effective refractive index of Si as a function of the air filling fraction, or porosity is shown. For each of the EMAs shown the refractive index decreases for higher porosities because the material becomes less dense and merges towards a refractive index of 1 for 100% porosity for air filling. For 0% porosity the refractive index of cSi is 3.5. There is some discrepancy between the EMA models due to the slightly different approach used for each one. The most widely used and accepted EMA for use with pSi is the Bruggeman EMA and this is the one chosen for use in this investigation.

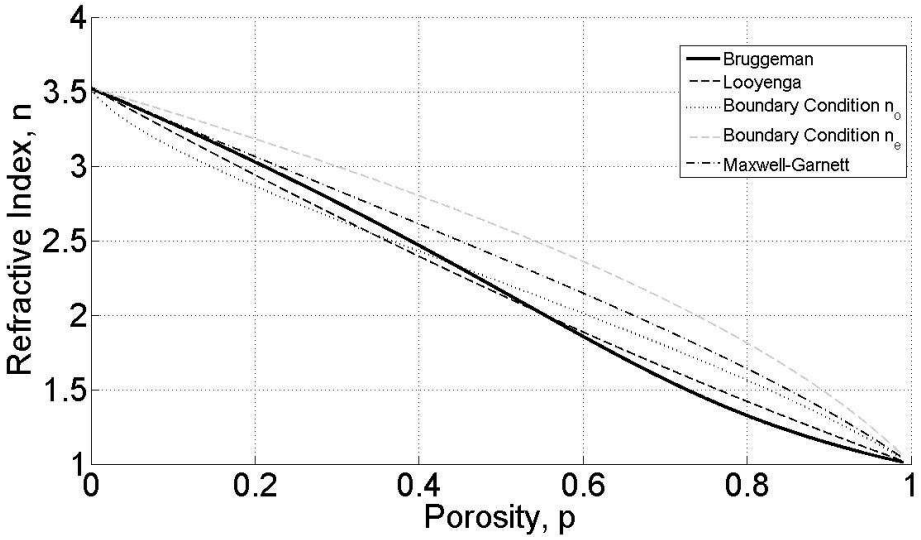

Figure 5.5 Different EMAs for calculating porosity using effective refractive index *n* of layer.

5.4 Acoustic Transmission Measurements through Porous Silicon Layers

Ultrasonic waves are used to non-destructively characterise material properties such as the elastic moduli of an elastic medium. Longitudinal BAWs have been used to study the acoustic properties of the fabricated porous layers. The pSi single and multilayers are sandwiched between two ultrasonic pillar-transducers (figure 5.6) which operate at a frequency of 1GHz with a bandwidth of around 400MHz. Longitudinal acoustic waves are launched into the pSi layers by coupling through a gallium-indium (Ga-In) eutectic liquid. An electrical output from a vector network analyser (VNA) connected to the transmitting piezoelectric transducer converts electrical energy into mechanical energy which sends acoustic waves through the samples. The receiving transducer converts the transmitted acoustic wave energy back from a mechanical motion into electrical form which is picked up by the VNA.

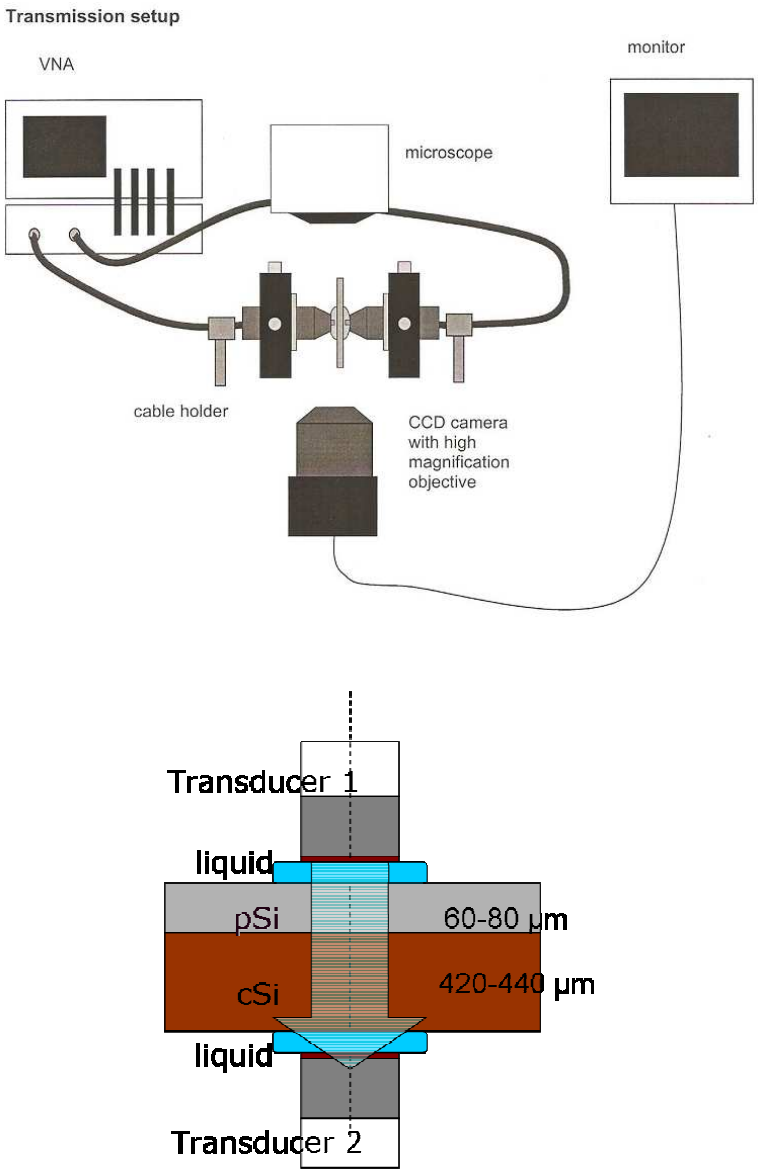

Figure 5.6 (Top) Transducer set-up for S_{21} transmission measurements and (Bottom) close up of transducers with wave propagation through the sample.

The matching pair of pillar transducers are Si-based with a thin ZnO piezoelectric layer and SiO_2 anti-reflection coating (ARC) and operate via the piezoelectric effect generating ultrasonic waves from a square cross-sectional area of 160 μm^2. The surface of the transducers are placed at normal incidence to the pSi sample surface and the typical longitudinal wavelengths excited throughout the pSi are 3 - 7 µm depending on porosity. For acoustic Bragg mirrors using this pSi material at 1 GHz frequencies, this typically requires layers of approximately one micron each. The

frequency range that is measurable using this equipment is up to 3 GHz, since for higher driving powers the transducers produce an overtone. The frequency response spectrum of the transducers is shown in figure 5.7 where a sampling bandwidth of 100 Hz was used for 2001 data points, centred at 1.5 GHz for the 3 GHz span. All sample measurements are normalised to this transducer response and give a transmission measurement in decibels (dB) against frequency. The acoustic wave at large distances from these piezoelectric transducers can be approximated by a uniform plane wave due to the presence of the Si pillar.

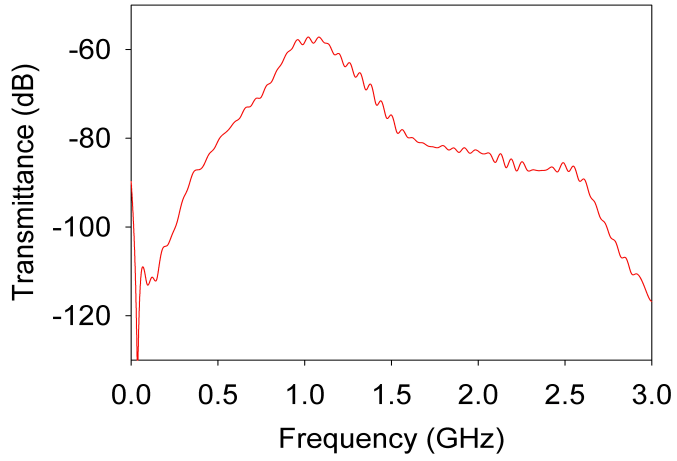

Figure 5.7 Frequency spectrum showing the response of the transducers at a source power of 20dBm.

Acoustic transmission measurements were performed at a central frequency of 1 GHz using the VNA where reflection and transmission parameters as a function of frequency are measured. A cable calibration was performed to compensate for scattering effects due to line impedance mismatches using a scattering-parameter (S-parameter) test set. There are two ports, one that transmits (port 1) and one that receives (port 2) the electrical signal through the system. The transmission parameters are measured at port 2 by receiving the transmitted signal from port 1 (S_{21}). Note that reflection measurements would be performed using only one port (S_{11} or S_{22}). The S-parameters make use of the reflection and transmission coefficients and deviations of expected measurements from their true amplitude can arise from random and systematic errors. Random errors include thermal noise (drift with temperature) introduced by oscillators and the systematic errors from losses and finite-port

matching. Systematic errors can be removed using cable calibrations which are performed under the same conditions that the acoustic measurements are taken, for example, the same frequency range and bandwidth. This is then compensated for in the recorded measurements.

5.4.1 Longitudinal Velocity Dependence upon Porosity

In chapter 3 the fabrication of single layers was described to find the dependence of the longitudinal velocity on porosity of the pSi matrix so that multilayered acoustic mirrors could be fabricated with their response tuned for a particular set of frequencies. The porosity was determined using optical measurements and the velocity dependence on porosity is determined by a similar process using multiple internal reflections of acoustic wave energy within single pSi layers. The multiple internal reflections arise due to impedance mismatches at boundaries within the sample and with the surrounding media. Each time the propagating elastic waves encounter a boundary there is a proportion of the incident wave that is transmitted and reflected so the wave will undergo multiple reflections within each layer of the sample. The group velocity through the porous layer and substrate was measured using ultrasonic transmission measurements with the transducers and VNA. The VNA measures the transmittance and reflectance at each frequency and scans through each of the frequencies to obtain a frequency response spectrum for each sample. This was done for each of the pSi single layers, an example is shown in figure 5.8.

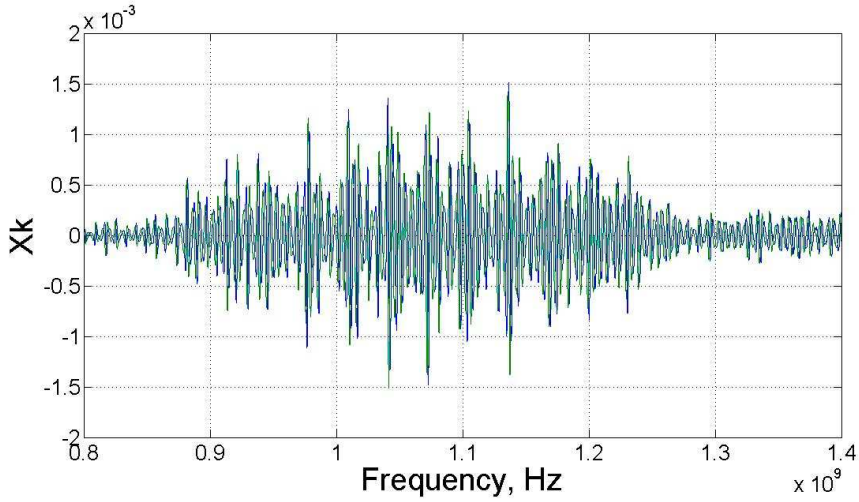

Figure 5.8 The original signal described by the set of X_k complex numbers in the frequency domain.

The frequency data gathered can then be Fourier transformed to obtain a series of reflection peaks in the time domain (figure 5.9). Each reflection peak corresponds to a 'round trip' reflection within a layer which has an impedance mismatch at both boundaries. The original signal in the frequency domain is described by the summation of complex numbers X_k shown in equation (5.25) which represent the amplitude and phase of the different sinusoidal components of the input signal x_n, where k=0,….,(N-1) for N complex numbers $X_0,\ldots,X_{N-1}$.

$$X_k = \sum_{n=0}^{N-1} x_n e^{-\frac{2\pi i}{N} kn} \qquad (5.25)$$

There are 2,401 points describing figure 5.8 that make up the set of complex numbers X_k and each individual frequency has both a real and imaginary part, $X_k=a+ib$. The equation above can also be written as equation (5.26), where ρ is the amplitude of the original signal described by the real and imaginary parts 'a' and 'b' and the phase is represented by ϕ in the frequency domain.

$$X_k=\rho e^{i\phi} \qquad (5.26)$$

where $\rho = \sqrt{a^2 + b^2}$

If the frequency sampling has N equally spaced points (N = 2,401) then to perform the Fourier transform the time scale must be specified using the Nyquist frequency equation (5.27) where Δf is the frequency span.

$$\Delta f = (N-1)\delta f \tag{5.27}$$

with $\delta t = \dfrac{1}{\Delta f}$

and $\Delta T = (N-1)\delta t$

For example, if the Nyquist frequency is 0.6 GHz and N = 2,401 this gives a sampling frequency of δf = 0.25 MHz. For the same frequency span the sampling time δt will therefore be 1.67 ns giving ΔT = 4,000 ns. These parameters determine the resolution of the measured signal. This new data set is represented by the summation of x_n complex numbers given in equation (5.28) where n = 0, …., (N-1) for N complex numbers x_0, …, x_{N-1} for a Fourier transform.

$$x_n = \frac{1}{N}\sum_{k=0}^{N-1} X_k e^{\frac{2\pi i}{N}kn} \tag{5.28}$$

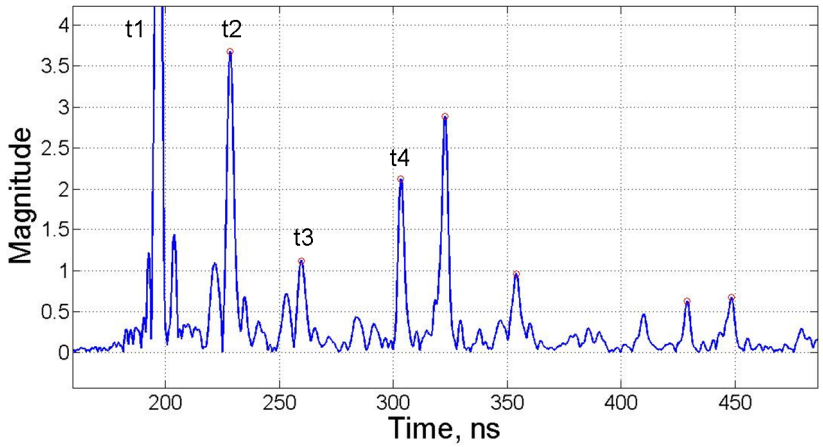

Figure 5.9 The Fourier transform of the original signal from the frequency domain into the time domain for sample *B3* (see table 5.1).

The set of x_n complex numbers can also be written similarly to that for the set of X_k complex numbers described by the equation $x_n = a' + ib'$ and $x_n = \rho' e^{i\phi'}$ where the different amplitude ρ' in the time domain is described by the following equation (5.29) with the phase ϕ' also in the time domain.

$$\rho' = \sqrt{a'^2 + b'^2} \tag{5.29}$$

The amplitude ρ' is analogous to the magnitude of the peaks in the time domain displayed in figure 5.9 with the y-axis displaying the 'abs(Y)' value of the x_n set of complex numbers i.e. the absolute value of the complex number x_n or $abs(Y) = abs(x_n) = |x_n| = \rho'$. Since each peak displayed in the time domain relates to multiple reflections within the measurement system, by identifying the origin of the peaks the time difference between consecutive peaks of the same origin can be used to find the longitudinal wave velocity through each layer. The thickness d of each layer is known so with the time delay Δt (or round trip time for one reflection) between peaks the velocity of longitudinal waves V_L through the porous layer can be found with equation (5.30). The porosity of each sample has already been found using Fabry-Perot interference measurements and the Bruggeman EMA.

$$V_L = \frac{2d}{\Delta t} \tag{5.30}$$

For the set of reflections within each layer shown in figure 5.10 the first peak corresponds to the arrival of the first signal *t1* that has been transmitted throughout the entire pSi layer on the cSi substrate. The subsequent peaks correspond to multiple reflections in one of more of the different layers of the sample *t2* for a single round trip reflection in the porous layer, *t3* a double round trip reflection in the porous layer, *t4* one single round trip reflection in the substrate layer and so on.

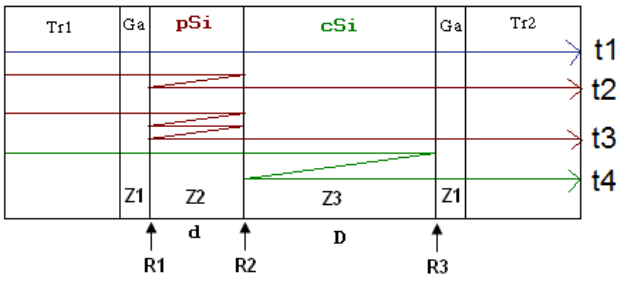

Figure 5.10 Schematic illustration of reflection-dependent paths.

Labelling: Tr1- Transmitting Transducer, Ga- Gallium-Indium eutectic coupling liquid, pSi- porous silicon, cSi- substrate, Tr2- Receiving Transducer, Z- acoustic impedance of layer, R- reflectance at interface, t- time, d- thickness of porous layer, D-thickness of substrate layer.

The parameters of the samples used for measuring the velocity dependence on porosity are shown in table 5.1 where different layer thicknesses have been used for each sample of different porosity.

Sample	Porosity	Velocity (km/s)	d of pSi layer (μm)
B13	0.25	7.2	18
B1	0.45	6.0	69
B2	0.49	5.3	72
B3	0.59	4.8	78
B8	0.62	4.9	77
B6	0.65	4.7	114
B4	0.69	4.3	63
B16	0.75	3.9	61
B17	0.84	3.3	53

Table 5.1 The properties of the samples used to determine the velocity dependence upon porosity *V(p)*.

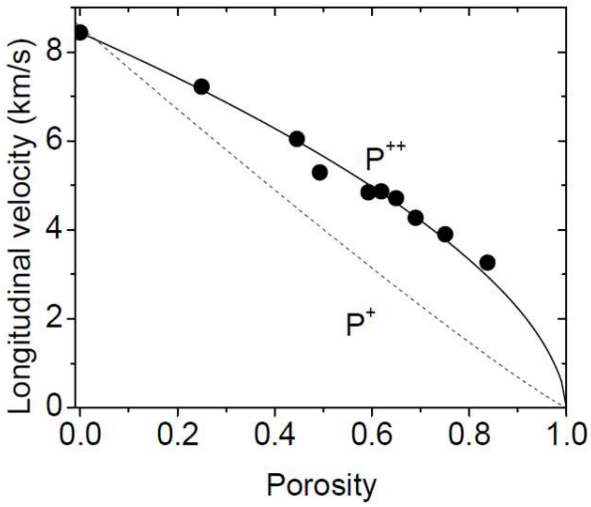

Figure 5.11 Measured longitudinal velocity dependence on porosity for p++ pSi in the [100] crystallographic direction (circles) with theoretical fit[92] and comparison to p+ pSi.[93, 94]

The longitudinal wave velocity propagating in the [100] direction for the p++ pSi was observed to be higher than that for lower doping levels of Si for the p+ samples measured by other groups[93, 94] as shown in figure 5.11. The porosity dependence was found to be described by the empirical formula given in equation (5.31) where the exponent value *k* is related to how well the periodic system is ordered.

$$V_L=8.43(1-p)^k \text{ km/s} \qquad (5.31)$$

The exponent value is k=0.6 for the measured p++ samples and k=1.095 for the p+ samples. The ordering of the pore structure of the p++ pSi is thought to be relatively well-ordered given the low experimentally measured k-value.

The error in the velocity measurements will be based on the error in the thickness measurement of the layers using the SEM and on the error in the Fourier transform measurements. The SEM measurements are accurate within 5 %, however the measurement of the time delay between peaks used to calculate the velocity through the porous layer is dependent on the ability to accurately distinguish between consecutive peaks in the Fourier transform. As seen in figure 5.9 the times at which reflection peaks are recorded are taken from the top of the peak. The *t2* peak shown in

figure 5.9 is located at 228.3 ns with the FWHM value of 3.6 ns. The mean distance of the p++ data points given in figure 5.11 from the theoretical fit curve is ±0.2 km/s.

5.4.2 Acoustic Transmission Measurements through Multilayered Porous Silicon

The transmission properties of the pSi multilayers are measured using the experimental setup described earlier in this section and shown in figure 5.6. The pSi multilayer samples are placed between the transducers and transmission through each sample is recorded. For the multilayers a series of stopbands are observed where certain regions in frequency are reflected by the multilayer mirrors. Additional characterisation of the multilayers is done via the acoustic transmission measurements where the agreement with SEM thickness measurements and optical measurements deducing porosity are checked when experimental and simulated acoustic data are compared. The acoustic transmission measurements on the pSi multilayers are normalised to the response of the transducers as shown in figure 5.12 below.

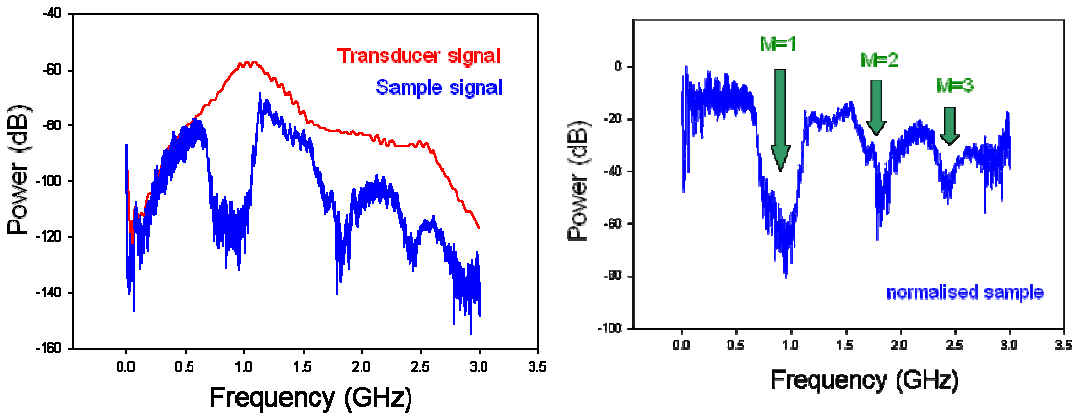

Figure 5.12 (Left) Sample measurement of Bragg mirror sample #1 showing three stopbands without normalisation to the transducer response which is also shown and (Right) normalised sample measurement showing the first three stopband modes.

5.5 Atomic Force Microscopy Imaging of Porous Silicon

Studying pSi using the atomic force microscope (AFM) allows imaging of the surface of the areas at which propagating acoustic waves are reflected, scattered or transmitted due to the impedance mismatches at the boundaries so it is useful to know the quality of the interfaces between different impedance layers to know how this affects acoustic energy incident on them. It has previously been shown that a thicker film of pSi leads to a rougher interface with the substrate and so using more pairs of layers in a Bragg stack could potentially lead to lower quality interfaces.[95] There is an interface between the different porosity layers within the multilayer and there is an interface between the pSi mirror and the bulk Si substrate. If the pSi mirror were to be removed from the substrate this would expose the bulk Si surface. It is this surface that has been studied for which surface roughness measurements using the AFM have been taken for a number of samples of removed pSi single layer films having different thicknesses.

The surface roughness and appearance of each sample was investigated and the image root mean square (rms) value for the scan area obtained from the surface of the sample. This rms value gives a roughness value for the exposed surface. It was expected that for thicker pSi layers removed, there would be a rougher surface exposed at the bulk Si substrate. The rms value $rms = \sqrt{\frac{\Sigma(Z_i)^2}{N}}$ is defined as the root mean square of the height deviations Z_i taken from the mean image data plane for a set number of pixels, or sample points N. The scan area and number of pixels determines the resolution of the AFM images. Scan areas of 10 μm^2 were used to study the pSi – cSi interface and larger scans of 75 μm^2 to capture the larger features of the back-side of the wafer were used. This is a destructive technique due to dissolution of the porous layer prior to placement within the AFM. Samples were prepared for the AFM by removing the porous layer from the bulk cSi substrate by dissolution in 3:1 ratio of 0.1M NaOH to ethanol solution after submersion into HF to remove the native oxide layer on the pSi surface. The samples were placed in an ultrasonic water bath at 29 °C for dissolution times up to 13 mins to remove layer thicknesses up to 124 μm. AFM surface images using contact mode were obtained

for the pSi - cSi surface using (10 µm x 10 µm), (40 µm x 40 µm) and (75 µm x 75 µm) scans and for the back-side of the Si wafer using (75 µm x 75 µm) scans.

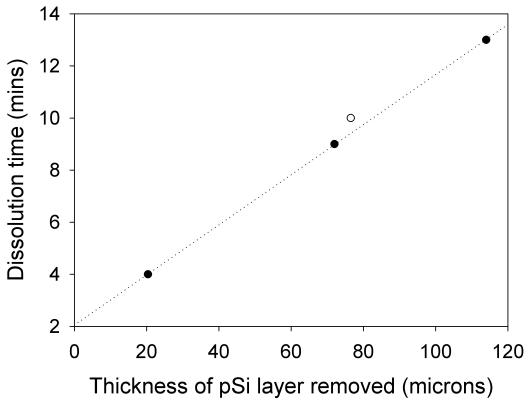

Figure 5.13 Dissolution of four pSi single layers in NaOH solution placed in an ultrasonic bath at 29 °C (filled circles) and at 34 °C (unfilled circle).

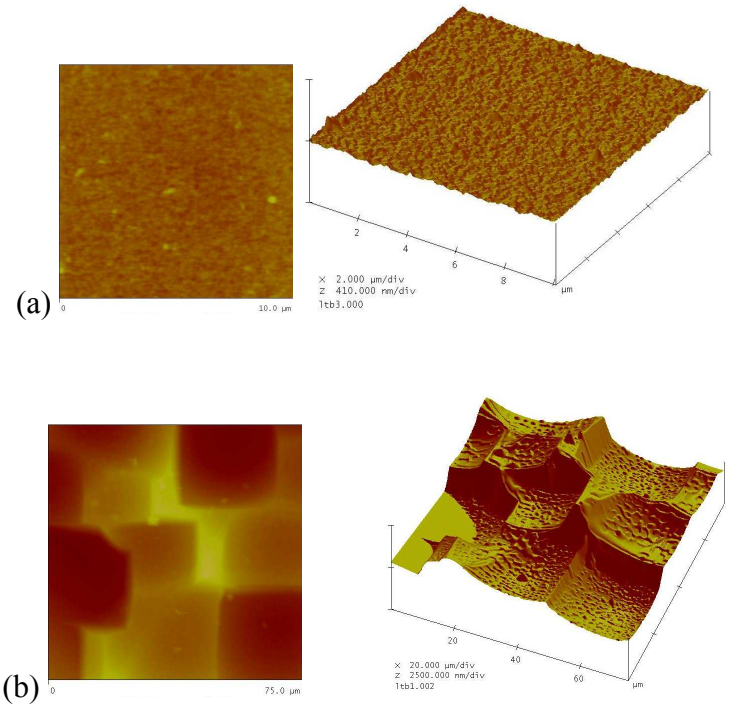

Figure 5.14 AFM contact mode height scans for the (a) pSi - cSi surface (10 µm x 10 µm) and (b) the back-side surface of a p++ Si wafer (75 µm x 75 µm).

The p++ Si wafers used to fabricate pSi are polished on the top surface so have a smooth surface before etching and the back-side of the SSP wafers have rougher surfaces (figure 5.14). In order to obtain statistical properties of each surface a height histogram was plotted for the pSi - cSi surface as shown in figure 5.15.

For each sample the pSi - cSi surface was studied using three separate scan areas and the three separate height histograms were plotted. The height distributions were found to be Gaussian and using the best Gaussian fit to the height histograms for each sample (figure 5.15) it is possible to use the Gaussian parameters to determine the surface roughness.[96,97]

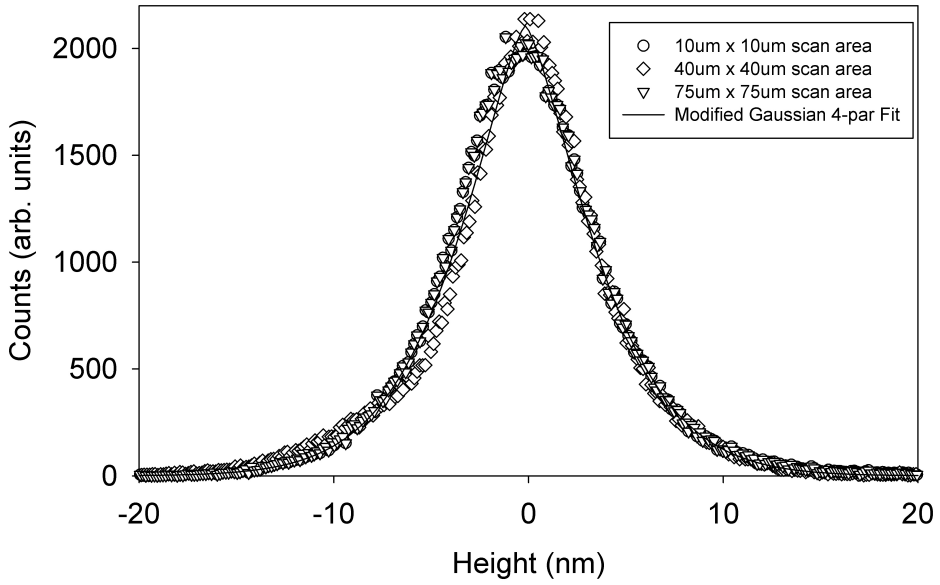

Figure 5.15 Height histograms for the three scan areas for the pSi - cSi surface of p++[100] pSi sample after removal of a 73 μm porous layer (sample *D*).

The Gaussian parameters shown in equation (5.32) are the height of the curve's peak a, the position of the centre of the peak x_0 and the standard deviation of the height distribution or rms value b. The coefficient b controls the width of the height distribution and this value is the rms surface roughness.

$$f(x) = a\exp\left[-\frac{(x-x_0)^2}{2b^2}\right] \tag{5.32}$$

The thicknesses of the single porous layers removed from each of the five samples used for this surface roughness study are shown in table 5.2 where the pSi removed ranges between 20 μm and 120 μm.

Sample	d removed (μm)	rms (nm)
A	20	2.7
B	68	3.4
C	71	3.2
D	73	3.7
E	120	4.0

Table 5.2 Surface roughness (rms) values for each porous layer removed.

The pSi - cSi surface has been observed to have a surface roughness between 2 – 4 nm for porous layer thicknesses between 20 – 120 μm (table 5.2). Generally, the thicker the porous layer then the rougher the surface with the bulk Si substrate.[98, 99, 100] However, the increase in roughness for layer thicknesses of this magnitude is almost non-existent. The surface roughness of the pSi - cSi interface is similar to that for the smooth top surface and since these nano-scale features are much smaller than the incident wavelengths (of the order of μm) there is only a small amount of scattering at this boundary.[101] The dependence of the incident wavelength on surface roughness is shown below where R_0 is the reflection from a perfectly smooth surface, R_s is the specular reflection from the rough surface of a material with surface roughness σ at an incident wavelength of λ.[101]

$$R_s = R_0\exp\left[-\frac{(4\pi\sigma)^2}{\lambda^2}\right] \tag{5.33}$$

Figure 5.16 shows the Gaussian fits to each of the five samples, the thicker the porous layer removed then the larger the standard deviation of the height distribution fit (wider curve) and higher rms value.

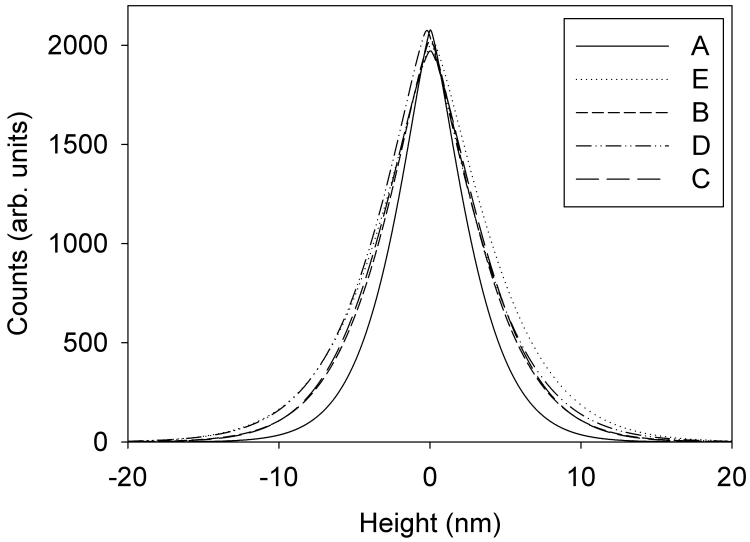

Figure 5.16 Gaussian Height distributions of the pSi - cSi interface for samples of varying thicknesses.

In addition to the samples shown above, the surface roughness of the back-sides of two different SSP Si wafers were also studied using a scan area of (75 μm x 75 μm) and found to have a mean rms of 713 nm. Note that the top surface is polished and the back surface is unpolished. The unpolished side was used for these surface roughness measurements. The rms measured is close to that measured by Zhao et al [96, 97] for a Si wafer similar to that shown in figure 5.14 (b). The height histograms of the back-sides of the p++[100] Si wafers are shown in figure 5.17 (Si samples F and G) and are not Gaussian in shape like the pSi – cSi surface. The features are large and show a stepped profile. There will be a larger degree of scattering at the back-surface of the Si wafers compared to minimal scattering at the top surface. At a frequency of 1 GHz, the wavelength of acoustic longitudinal waves through Si is 8.4 μm. If the back surface of the Si wafer is around 0.7 μm in surface roughness, the degree of scattering at this surface using equation (5.33) will be $R_s = 0.33R_0$. To avoid scattering affects in acoustic measurements, DSP wafers can be used.

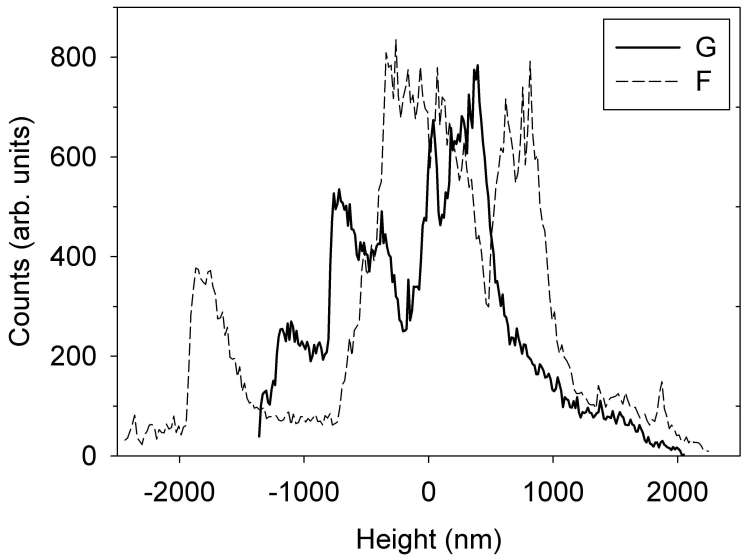

Figure 5.17 Height histograms for the back-sides of two different p++[100] Si wafers.

5.6 Optical Measurements of Porous Silicon Multilayers

The optical spectrum reflected from a multilayered stack of pSi is different to that seen for a single pSi layer. For the multilayer there are more contributing interfaces that the incident electro-magnetic wave sees and there is a reflection and transmission at each boundary. Depending on the effective refractive index profile of the multilayer the reflection from the stack will change. For Bragg mirrors, higher order modes are exhibited in the visible and IR regions of the spectrum due to constructive interference of light at these wavelengths which is reflected. For rugate filters, higher order modes are not necessarily seen since the higher order modes are suppressed. However, fitting parameters as described later in chapter 6 are used to determine the porosities of the layers within the multilayered stack. An example of the optical response of a pSi Bragg mirror is shown in figure 5.18 measured in the IR region of the spectrum where the fundamental stopband can be seen near 1100 nm, the Bragg mirror has individual

layers that are 150 nm thick. A pSi Bragg mirror with these layer thicknesses would be applicable to acoustic applications near 20 GHz.

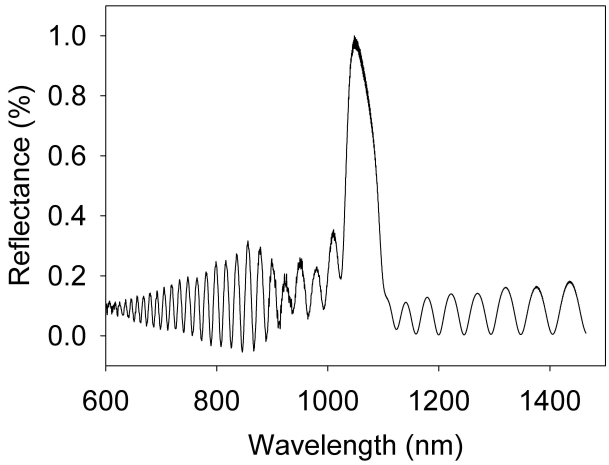

Figure 5.18 Optical stopband seen from a pSi Bragg mirror, sample #9.

For a pSi Bragg mirror with individual layers that are thicker than 150 nm, the fundamental optical stopband will be located at longer wavelengths. This is shown in figure 5.19 below where optical measurements have been made in the visible region for a pSi Bragg mirror with individual layers that are over a micron thick. This particular Bragg mirror was designed for acoustic applications at 0.9 GHz. The high order optical modes shown are for the M=11 to M=16 modes.

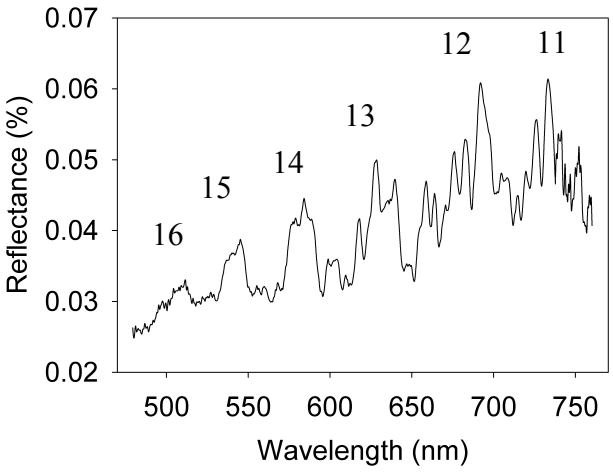

Figure 5.19 Optical spectra for Bragg mirror sample # 1, showing high order modes in the visible region for M=16 at 512nm and other orders at 545nm, 584nm, 629nm, 694nm and 735nm.

The order number of the modes can be determined using equation (3.19) introduced earlier in chapter 3, by looking at two consecutive modes. For example, it can be seen in figure 5.19 that there are modes at 545 nm and 584 nm and substituting these values for M and (M-1) keeping $n_1d_1+n_2d_2$ constant gives the order number M=15 and M=14.

The optical response measured from a pSi rugate filter is shown in figure 5.20 where the simulated data was fit to experimental measurement to find the layer porosities.

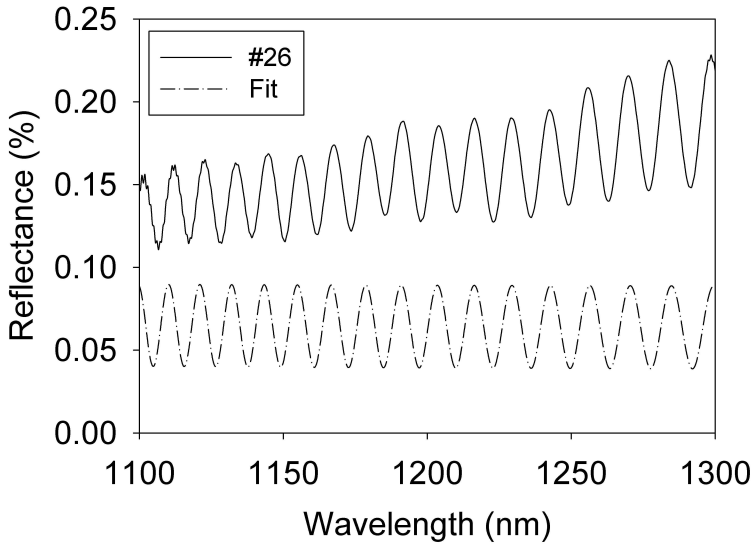

Figure 5.20 Optical response of a pSi rugate filter.

This chapter has discussed the techniques used to characterise the pSi single layers and pSi multilayers using optical interference measurements to deduce the effective refractive index of the porous layers. The Bruggeman EMA gives a porosity value for the known effective refractive index measured for the pSi layers. Acoustic transmission measurements through the pSi samples were made using a pair of transducers. Using the layer thickness measurements from the SEM and the time delays in peak arrival times from reflections within the porous layer, velocity of the longitudinal waves as a function of porosity has been found. Phononic stopbands have been observed in the acoustic transmission measurements performed on the pSi multilayered mirrors. The surface appearance of the pSi-cSi interface and the back surface of the Si wafer have been studied using the AFM and the back surface was found to have the largest surface roughness. After characterising the single pSi layers fabricated, pSi multilayers with desired acoustic responses have been designed and these are discussed in detail in the next chapter.

6. Models of Porous Silicon Multilayers

It is essential to understand the response of potential devices through simulations and modelling by inputting known material properties into the models so that the response of each multilayer can be predicted depending on design parameters. It is important to compare simulated results with real experimental data to confirm the understanding of the devices being studied. Much is known about the characteristics of cSi and its material properties, and these properties are modified for the porous material. In order to accurately predict the response of pSi multilayered structures it is necessary to input known properties of this pSi material based on the optical and acoustic longitudinal wave measurements performed on the single pSi layers. By understanding how a single pSi layer behaves it is possible to predict the behaviour of more than one single layer together. In order for this to be done the transfer matrix method (TMM) has been employed. The TMM has been used to simulate the optical reflectance from the multilayered samples as well as the acoustic response of the multilayers. Matlab has been chosen as the platform to run the simulation programs. The TMM is flexible in that it enables the anti-reflection coating properties of the transducers used in the acoustic measurement system to be included in the modelling. An advantage of the TMM is that there is no limit to the number of individual layers chosen for the repeating period and no limit to the number of layers within the overall multilayered stack. Each individual layer can be defined by its porosity and thickness and the matrix method can build as many layers as is necessary. However, with increasing layers the computational time increases and the simulations can become slower to run, up to 20 minutes in practice. Initially simulations have been run to correspond with the experimental measurements performed on single pSi layers. This includes a Fabry-Perot program to deduce the porosities of the single layers as described in chapter 3.

The acoustic simulations have been modelled using TMM where the reflection coefficients at each interface are found and then segmented together for later interfaces to describe the entire stack. For the TMM the internal reflections within each layer are considered and taken as a series. This is similar to measurements using the VNA since the frequencies are scanned across the entire range and the

transmittance and reflectance is calculated at each frequency. This gives a transmittance or reflectance dependence on frequency.

6.1 Bragg Mirror Model

The dielectric properties of a one-dimensional periodic layered medium have been modelled. The multilayered stack of alternating layers of high and low porosity of pSi is a stratified medium where each of the individual layers are assumed to be homogeneous. The stack can be seen as a collection of parallel layers as shown in figure 6.1 where the optical admittance is given by η and the physical thickness of the layer is given by z.

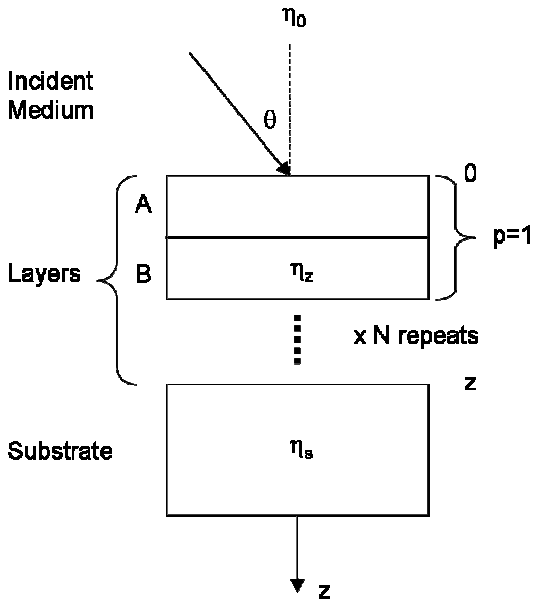

Figure 6.1 The block diagram used for the transfer matrix method of modelling.

For both the optical based and acoustic programs developed the angle of incidence θ of the waves is zero unless otherwise stated i.e. they are incident perpendicular to the surface of the multilayered stack. Initially, it has been assumed that the interface between each of the individual layers is smooth and that there is a direct step from each layer to the next layer. The porosity throughout each individual layer is assumed to be constant and the thickness of each pair of layers (each unit cell) is consistent

throughout the model. It is noted that in reality, this may not the case as there may be a chirp on the porosity or thickness of layers in the mirror and throughout the multilayered stack if etch breaks are not included during the fabrication process. However, for initial simulations this will be ignored for simplicity. Simulation programs have later been developed to include the existence of roughness across the interfaces within the multilayers that will be discussed later in this chapter.

$$\underline{\underline{M}} = \begin{bmatrix} \cos\beta & \frac{i\sin\beta}{\sqrt{\eta_0\eta_s}} \\ i\sqrt{\eta_0\eta_s}\sin\beta & \cos\beta \end{bmatrix} \qquad (6.1)$$

The properties of the dielectric pSi layers can be described using the (2 by 2) characteristic matrix, $\underline{\underline{\boldsymbol{M}}}$ of equation (6.1) which relates the electromagnetic field at one boundary with the field at the next. This matrix therefore describes the effect that a layer has on an electromagnetic wave travelling through it. This will remain unchanged for each sample and enabling flexibility in the model to alter the properties of the surrounding media. For example, the ARC properties of transducers used for acoustic measurements can be added to the simulation for a more accurate results model and the coupling liquid chosen can also be stated in the model. Different multilayered devices can be chosen and modelled, such as Fabry-Perot filters (microcavities).

The quarter wave stack used to describe the Bragg mirrors modelled in this investigation is symmetrical and can be described by a single matrix as shown by equation (6.1) where $\underline{\underline{\boldsymbol{M}}}$ is known as the characteristic matrix.[102] This describes one pair of layers of high and low refractive index where β is the phase thickness, η_0 is the optical admittance (or refractive index) of the incident medium and where η_s is the optical admittance of the substrate material. The equivalent optical admittance of the layers is described by the term $\sqrt{\eta_0\eta_s}$. Since there is a continuous electromagnetic wave incident on the multilayers it is necessary to define the polarisation and angle of incidence of the light. The light is at normal incidence to the pSi surface so the p-polarisation and s-polarisations are the same because both the electric and magnetic fields are within the plane of stratification of the pSi layers.

The phase thickness β is given by equation (6.2) where z is the physical thickness through the layers and $\gamma(z)$ is the optical thickness of the layers,[103]

$$\beta = \frac{2\pi}{\lambda}\int_0^z \gamma(z)dz \qquad (6.2)$$

where $\gamma(z) = n\cos\theta$ with n being the complex refractive index of the layers and θ the angle of incidence. For a balanced optical Bragg mirror for a target fundamental wavelength of λ_0 the integral will be a quarter wavelength in thickness. If the imaginary part of the complex refractive index number is negative then the material absorbs energy whereas if it is positive it is a gain medium. However, if the refractive index is a real number then the material can be said to have no loss. The effective dielectric constant for the pSi layers is a function of the porosity, dielectric constants of Si and air and also the EMA chosen and wavelength. The effective refractive index n_{eff} is found using the real part of the square root of the effective dielectric constant ε_{eff}.

$$n_{eff} = \Re\left(\sqrt{\varepsilon_{eff}}\right)$$

When this one pair of layers (or unit cell) is repeated, the response of a multilayered stack can be considered by summing the effect from one pair of layers (integer p=1) through all repeats N shown in the resulting matrix of equation (6.3) which describes the optical response from a stack of layers on top of a substrate material.

$$\begin{bmatrix} B \\ C \end{bmatrix} = \left\{\prod_{p=1}^{N}\left[\underline{\underline{M}}\right]\right\}\begin{bmatrix} 1 \\ \eta_s \end{bmatrix} \qquad (6.3)$$

The optical admittance of the stack and substrate is given by Y=C/B and the total reflectance R of the stack and substrate by equation (6.4) as follows.

$$R = \left(\frac{\eta_0 - Y}{\eta_0 + Y} \right)^2 \qquad (6.4)$$

In the program, each unit cell is described by one *AB* pair of high and low porosity layers where p_1 and p_2 are the porosities of the *A* and *B* layers and d_1 and d_2 are the thicknesses of the layers. The period of the structure, Λ is defined as $\Lambda = (d_1+d_2)$ and the total thickness, *D* of the multilayered stack is $D=N\Lambda$ where *N* is the number of repeats of the pairs of layers. The standard variables used in the program are *N*, d_1, d_2, p_1 and p_2.

The transmittance of the wave through the structure can be modelled as can the reflectance response. Additional parameters added to the model include the existence of an etching slope which occurs from the depletion of HF concentration during fabrication of the structures. This introduces a gradient across the porosity and thickness of the layers within the stack to modify the response of the stack accordingly. Note that the thickness of the layers within the multilayered stack are parameters input into the simulations but the thicknesses have been determined using SEM measurements and so are not major variables in the simulations when fitting to measured data. The optical model is important in calculating the porosities of the grown structures based on fitting parameters to experimental measurements using optical interferometry. The measured data is fitted to the simulated data and the porosity deduced using the Bruggeman EMA described in chapter 5. The effective refractive index of each porous layer in the stack is calculated using this EMA and the optical admittance is used to find the optical response of the layers with the TMM. For the optic response program the TMM models a continuous electromagnetic wave incident at a defined angle to the surface of the stack. For the acoustic model, a plane wave propagates throughout the structure perpendicular to the direction of stratification.

An optical model and an acoustic model has been designed to study the response of the pSi multilayers. The method with parameters detailed so far describes the optical response of a pSi Bragg mirror. The same method has been used to model the acoustic properties of the pSi multilayers. For the acoustic model, equation (6.1) was used

where $\eta_0=\rho_0/Z_0$ describes the acoustic impedance of the incident medium and the acoustic impedance of the substrate is given by $\eta_s=\rho_s/Z_s$. The phase thickness term is given by

$$\beta = 2\pi f \int_0^D \gamma(D)dD ,$$

where D is the physical thickness through the layers, f is the frequency and $\gamma(D)=\rho\cos\theta/Z$ with ρ the density of the layers and Z the acoustic impedance of the layers. The wave transmission properties of each sample (or stack) have been found and band-diagrams such as those shown in chapter 3 are obtained which give information about the reflectance and transmittance of multilayers having specific porosities and thicknessses.

6.2 Rugate Filter Model

Depending on the design of the multilayer stack that is to be modelled it is necessary to state whether the overall stack will be a Bragg mirror, rugate filter or a Fabry-Perot filter (microcavity); this is important in building the matrix. For example, for the Bragg mirror modelling the arrays are based on a repeating block of two layers as already described, whereas for the Fabry-Perot filters there is the addition of a defect cavity layer between two Bragg mirrors. The shape of the defect layer will influence the transmission peak in the stopband i.e. constant or varying porosity in the cavity layer. The thickness of the cavity layer is generally designed to be of half-wavelength thickness and this has some flexibility to modify the location of the transmission peak within the stopband but with a trade off with the amplitude of the peak. The thickness will be approximately equal to the sum of the thickness of the AB layer (d_1+d_2).

In contrast to the Bragg mirrors and microcavities which have homogeneous layers of alternating high and low porosities, the rugate filters have a continuous variation in their refractive index or acoustic impedance. The porosity profile therefore oscillates between a maximum and minimum porosity. The shape of the porosity profile

determines the properties of the rugate filter's response in terms of stopband location, bandwidth and depth. The characteristic matrix used to simulate the response of Bragg mirrors can also be used to closely simulate an inhomogeneous porosity profile such as that which describes a rugate filter. The overall rugate structure is a periodic stack of layers with varying porosities so it can be defined as a collection of much smaller sub-layers within the AB layers used to previously describe the Bragg mirror stack. This is shown in figure 6.2 where the sub-layers represent a smaller porosity variation.

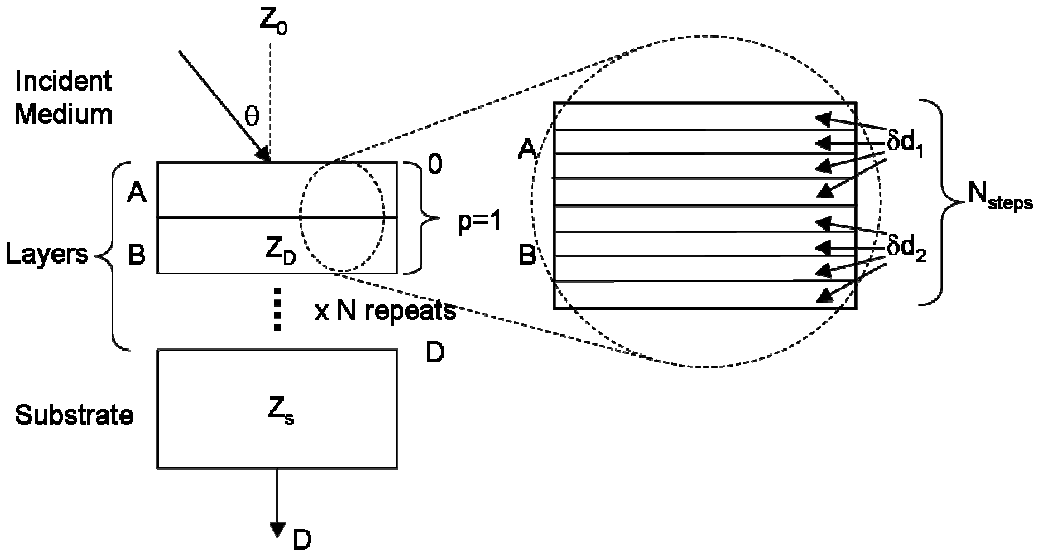

Figure 6.2 Modelling the rugate filter using the TMM.

In order to model a smoothly varying porosity profile it is necessary to split up each of the AB pairs of layers into a number of sub-layers where each sub-layer possesses a set porosity and thickness but together create the appearance of a smooth profile. The number of sub-layers in the unit cell, N_{steps} or 'Steps' used to model a rugate filter must be sufficient enough to simulate a smooth variation of porosity throughout the multilayered structure. Each sub-layer is assumed to be homogenous in nature with a set porosity and thickness. In the 'A' layer the porosity is different for each sub-layer in the range δp_m for $1<m<(N_{steps}/2)$ and the sub-layer thickness is δd_1 for all sub-layers in 'A'. Similarly the sub-layers in the 'B' layer have porosity δp_n for $(N_{steps}/2)+1<n<N_{steps}$ and thickness δd_2. The porosity of each sub-layer changes according to the pre-defined porosity profile chosen for each different rugate filter.

Generally, sinusoidal porosity profiles have been used for the fabricated samples although other shapes of porosity profile have been studied during the modelling stage. Steps of N_{steps} = 16, 32, 64, 128 were used in the model.

$$d_1 = \sum_{1}^{N_{steps}/2} \delta d_1 \tag{6.5}$$

$$d_2 = \sum_{1}^{N_{steps}/2} \delta d_2 \tag{6.6}$$

Due to the need for a reasonable length of time to run the computations, there has to be a limit to the number of sub-layers N_{steps} used to model the rugate filter. It is therefore recognised that a truly smooth variation on porosity profile can never be achieved in the model, however what has been modelled as a rugate filter is sufficient in terms of reducing higher order harmonics and to produce only the fundamental frequency stopband which defines the response of a rugate filter. The *steps* are the number of sub-layers in the *AB* pair of layers within the repeating unit cell. This is chosen to match the number of sub-layers defined in the LabView program during the etching of the pSi rugate structures as shown in figure 6.3.

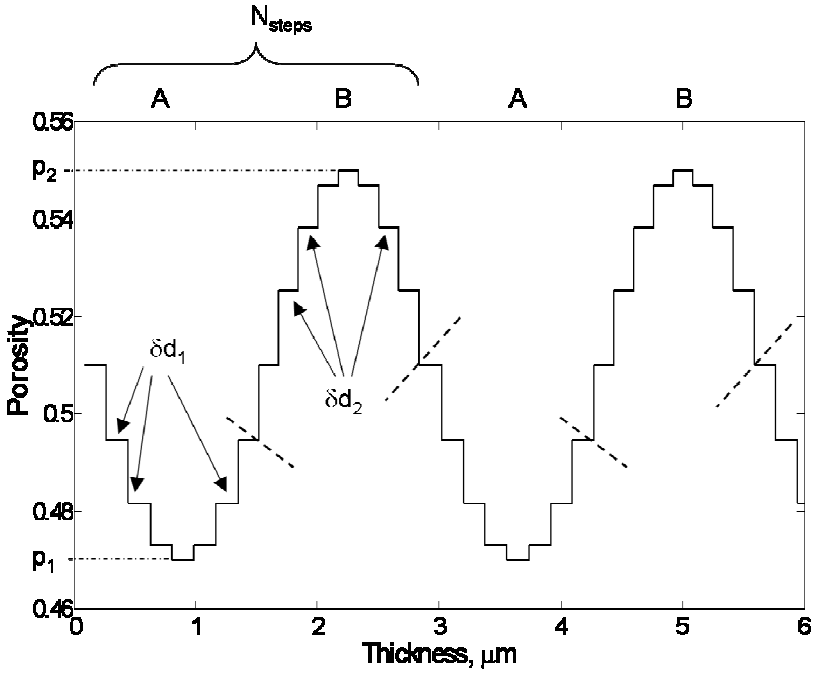

Figure 6.3 Porosity profile of the rugate filter modelled in steps using the TMM.

The sinusoidal variation shown in figure 6.3 above shows p_1 and p_2 which are the minimum and maximum porosities respectively. The sinusoidal variation in the porosity profile p of the rugate filter has been input into the model using the following formula,

$$p=p_{av}+\Delta p sin(\beta) \qquad (6.7)$$

where p_{av} is the mean porosity $p_{av}=p_1+(p_2-p_1)/2$, Δp is the difference between the high and low porosities as $\Delta p=(p_2-p_1)/2$ and β is the phase thickness.

The simulated acoustic data shown in figure 6.4 was modeled using the TMM as described in the previous section.[104] The effect of having a continuously varying acoustic impedance profile has been investigated by taking a Bragg mirror design and smoothing the square-wave impedance profile. A single dominant stopband is observed due to the half-period sine wave excursions from the average impedance. The profile shown in the inset of figure 6.4 has alternating spatial half-periods of 1.31 μm and 1.44 μm which would give a balanced Bragg mirror using porosities of 0.55 and 0.47 with a time of flight of τ = 25 ns in each layer *A* and *B*.

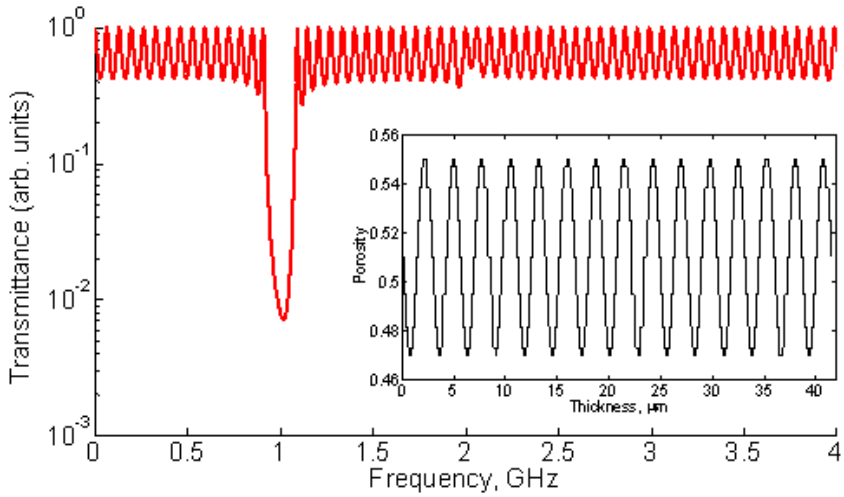

Figure 6.4 Simulation of transmission through pSi acoustic rugate filter with stepped porosity profile shown in inset with p_{high}=0.55 p_{low}=0.47, half-cycle thicknesses of d_1=1.31 μm d_2=1.44 μm and N=15 repeats based on smoothing a quarter-wave Bragg mirror.

6.3 Effect of Symmetry on the Modes of a Bragg Mirror with the Fundamental Mode at 20 GHz

A Bragg mirror with the fundamental mode located at 20 GHz has been chosen to study the effect that the symmetry of the Bragg mirror has on the stopband modes. This frequency was chosen so that this model could be extended in the next section to investigate the effects of interface roughness on the stopband modes. For a Bragg mirror with this fundamental frequency, the layers are typically < 100 nm and so are likely to be heavily affected by interface roughness. In this initial section, no losses have been included in the modelling. For the comparatively lower frequency Bragg mirrors fabricated for use at 1 GHz there was no observed porosity gradient across the layer thickness due to the inclusion of etch breaks. A porosity gradient is less likely in Bragg mirrors designed for higher frequencies above 20 GHz as the layers would be much thinner. The model assumes a uniform porosity across the layer thickness.

Running the acoustic Bragg mirror model for a pSi stack with a finite number of layers gives the transmission spectra of the acoustic multilayer in the frequency domain, displaying the positions, depth and bandwidths of stopbands. The finite number of layers in the Bragg mirror gives rise to a finite stopband depth. The position of the stopband modes for each calculation was recorded as was the bandwidth of each stopband. The thickness of each pair of layers within the stack was constant so that (d_1+d_2)=140nm. The ratio of thickness for layers *A* and *B* was varied for ratio values described by Γ for $0.1<\Gamma<0.9$. The number of pairs of layers is N=35 and the porosity of layer *A* is p_1=56% and layer *B* is p_2=46%. For each calculation the layer thicknesses in nanometers are given in the ratios $d_1=140\Gamma$ and $d_2=140(1-\Gamma)$. Note that for a porosity of 56% the longitudinal wave velocity through the pSi layer is 5.176 km/s and for a porosity of 46% it is 5.847 km/s.

The time that the longitudinal waves spend in each layer *A* or *B* of the multilayer have been calculated using the velocity relation found for the [100] pSi samples studied and it has been assumed that the velocity dependence on porosity is constant for all frequencies. The effect of dispersion is stronger for higher frequencies > 50 GHz as the acoustic loss will increase. The empirical velocity equation (5.31) found for the p++ pSi samples, based on acoustic longitudinal measurements taken at 1GHz, may change for higher frequencies where the exponent *k* may reduce slightly for higher frequencies.

Γ	**d_1 (nm)**	**d_2 (nm)**	**τ_1 / τ_2**
0.1	14	126	0.1
0.2	28	112	0.3
0.3	42	98	0.5
0.4	56	84	0.8
0.5	70	70	1.1
0.6	84	56	1.7
0.7	98	42	2.6
0.8	112	28	4.5
0.9	126	14	10.2

Table 6.1 Symmetry (τ_1/τ_2) of the Bragg mirror for each value of Γ chosen.

The symmetry (τ_1/τ_2) is noted in table 6.1 with a symmetry of 1 indicating a balanced Bragg mirror which has the same time of flight τ_1 in layer *A* and τ_2 in layer *B*. The balanced Bragg mirror only has odd order modes and the time of flight $\tau = d/V$ which for layers < 100 nm is typically a few picoseconds.

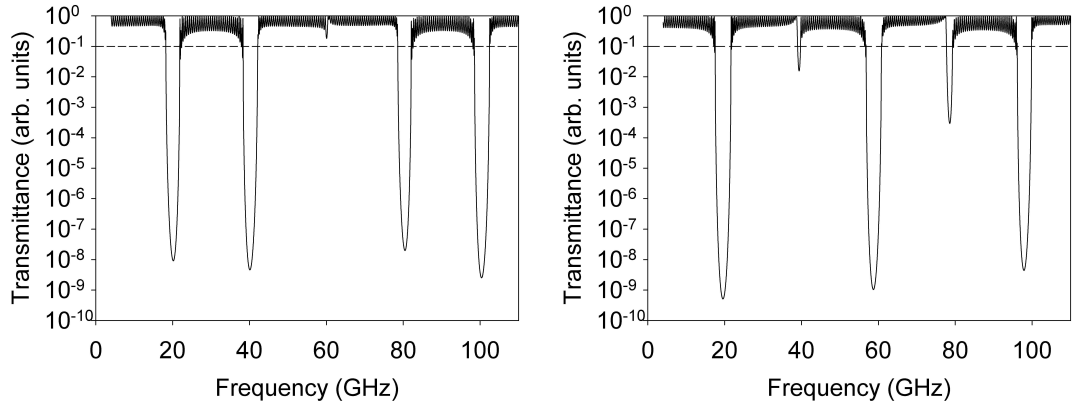

Figure 6.5 Examples of some of the transmission specta of the Bragg multilayers shown for D=140nm with (left) Γ= 0.3 and (right) Γ= 0.5.

Figure 6.5 shows an example of the acoustic transmission properties modelled for two Bragg mirrors with Γ values of 0.3 and 0.5. The frequency at which each stopband is located has been recorded and the bandwidth of the stopbands were found for an arbitrary transmission value of 0.1 (shown by dotted line in figure 6.5). This value was arbitrarily chosen because this typically gave stopbands below the fine transmission mode oscillations and the bandwidth at this point was not influenced by the overall stopband depth. For each stopband edge intersecting this arbitrary point, the frequency for the left side of the stopband (corresponding to the lower of the two frequencies recorded) and the right side of the stopband was noted. These are the data points seen on the graph given in figure 6.6 and the stopband mode is given by *M* seen on the right hand side.

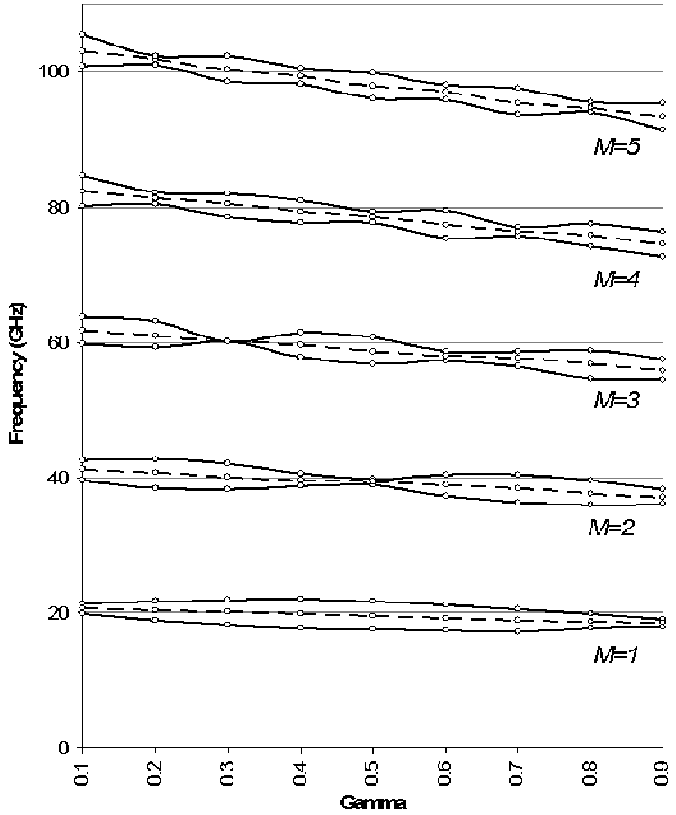

Figure 6.6 Dependence of the stopband widths on Γ for stopband orders M=1 to M=5.

For a Γ value of 0.5 the symmetry of the Bragg mirror is around 1 .i.e. for a balanced mirror. Either side of this Γ=0.5 value the Bragg mirror becomes more and more asymmetrical. This asymmetry has more affect on higher frequencies since for values of the ratio Γ above 0.5 for this particular case there is a higher average porosity which results in lower velocities of the acoustic longitudinal wave through the stack. As seen in figure 6.6 this leads to a lower resulting frequency for higher harmonics and creates the skew to the stopband frequency on Γ. It can be seen that for certain values of Γ higher order stopbands can close up due to the symmetry of the Bragg mirror. For example, for Γ=0.5 (a symmetry around 1) there exists the fundamental mode, and the even order harmonic stopbands close up for M=2, 4 and with open stopbands for M=1, 3, 5 as shown in figure 6.6.

The locations and bandwidths of the stopband modes for a Bragg mirror with the fundamental mode at 20 GHz has been modelled in this section. The next section will consider the effect that interface roughness has on the stopbands calculated for the Bragg mirror centred at 20 GHz.

6.4 Interface Roughness Effects

The programs used for the simulations described above were modified to include the effect of an interface roughness between layers of different porosities within the multilayered stack. Apodisation effects have also been studied using a modification of the programs above and are discussed in chapter 7. An ideal *AB* layered system does not possess interface roughness. However, it is useful to know how interface roughness affects the performance of multilayered devices fabricated from pSi. With increasing interface roughness a Bragg mirror will transform into something more rugate like. For thinner layers this will become more noticeable and higher order modes will start to close.

The effect of interface roughness between each of the layers within the multilayered stack has been studied to evaluate the effect of the porosity change across the interfaces within the multilayered stack on each of the stopband positions, widths and depths. This has been done using the TMM to model the transmission of acoustic longitudinal waves through multilayered samples. The interface roughness between pSi layers has been found to be dependent on the dopant type, doping level, temperature during fabrication, layer thickness and porosity so that the roughness can be minimised to produce higher quality multilayers. Optical Bragg mirrors can have very smooth interfaces < 10 nm and for high frequency applications (tens of GHz) the layer thicknesses of acoustic Bragg mirrors are similar to those used in optical applications. This is useful information when designing Bragg mirrors for higher frequency regimes as it is important to know how the interface roughness affects the performance of the multilayer. For these reasons it is necessary to study the effect of small values of interface roughness on the acoustic response of the stack. Figure 6.7 highlights the interface between a pSi and cSi substrate.[105]

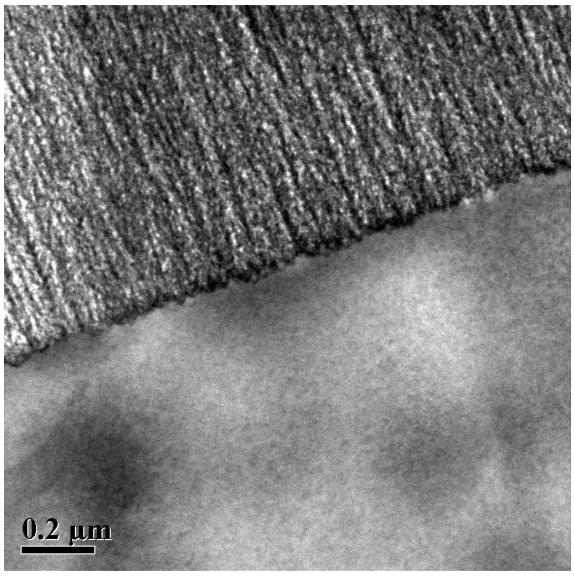

Figure 6.7 Interface between the pSi layer and cSi substrate.[105]

It is proved that the surface roughness of the pSi is Gaussian in nature and it has been assumed that the change from one porosity to another across the layer interface also follows this profile. For this calculation, the interface between layers of two different porosities was smoothed using an erf(x) or erfc(x) function. The error function erf(x) and complimentary error function erfc(x) are linked as erfc(x)=1-erf(x). Erf(x) is an odd function which is found by integrating a normalised Gaussian function so that erf(0)=0 and erf(∞)=1.

$$erf(x) = \frac{2}{\sqrt{\pi}} \int_0^x e^{-t^2}\, dt \qquad (6.8)$$

Where $x = \Delta x / \sigma$

The argument of x is described by equation (6.8) where Δx is the distance from the centre of the interface and σ is the interface roughness. The effect of this smoothing is to reduce the distinction of porosity between each layer so that instead of a direct step across the interface from one porosity to the next, there is a gradual change of porosity across the interface through a given distance. A small value of Δx and σ will

give a more distinct step in porosity change across the interface than large values of Δx and σ which give a less defined interface between the two layers. It has been assumed that if the interface is rough and this is averaged over a large area then a smoothed porosity profile will be realised. The effect of the erf(x) function is shown in figure 6.8 where different smoothing widths and roughness of Δx and σ have been used.

This is a basic model and as such has many limitations. The smoothing effect is valid across every interface within the multilayered stack and each interface has the same smoothing potential across it. This is in contrast to what has been experimentally observed by AFM measurements (chapter 5) where the surface roughness increases with layer thickness. Note that the AFM measurements give values for surface roughness not interface roughness. This would suggest that the deeper layers within the stack will have rougher interfaces between the layers compared to those at the top. The change in interface roughness across the entire stack has not been included in this model.

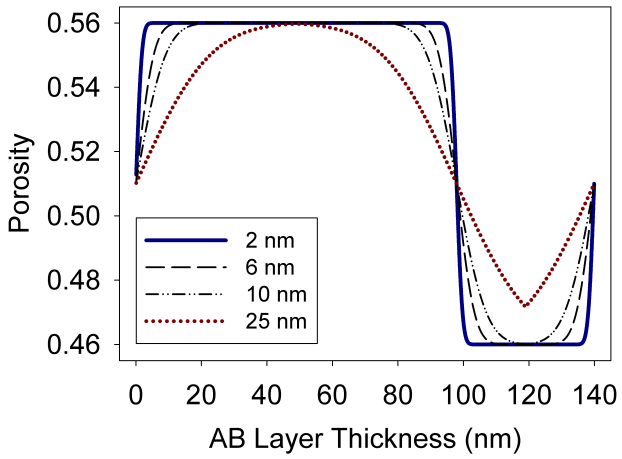

Figure 6.8 Porosity profiles for interface roughnesses of σ = 2nm, 6nm, 10nm, 25nm with p_1=0.56, p_2=0.46, d_1=98nm, d_2=42nm (Γ=0.7) and N=35.

In this basic model, for thin layers within the stack the smoothing function breaks down quicker than for thicker layers because sharper features are created across the interface as shown in figure 6.8. It can be seen that small values of roughness create a smoothing across the interface but for higher roughness values > 25 nm the smoothing

function causes the interfaces to move into one another and create sharper features. For the Bragg mirror example used in this section, the roughness model is only valid for an interface roughness less than 25 nm. By increasing the interface roughness the porosity profile of a Bragg mirror has a closer resemblance to a rugate filter. The interface roughness has been imposed onto a square wave porosity profile describing that of an acoustic Bragg mirror. The layer thicknesses in nanometers are given in the ratios $d_1=140\Gamma$ and $d_2=140(1-\Gamma)$ for $\Gamma=0.2$ and 0.7, the values of which were chosen because open stopbands were obtained across the frequency range of interest so seemed ideal to investigate the effect of interface roughness on the stopbands.

The effect of the interface roughness on the layers is shown in figure 6.9 where the ideal Bragg mirror (without interface roughness for 0 nm) shows deeper and wider stopbands in comparison to the stopband reduction for imposed interface roughness of 25 nm. The initially smaller stopbands are seen to close up completely hence transforming into a more rugate like structure. This is because a gradual change in the porosity profile is introduced at the edges of the square wave profile of the Bragg mirror. The higher frequency stopband modes are more heavily affected by the interface roughness and it can be seen in figure 6.9 that the higher order modes diminish for rough interfaces.

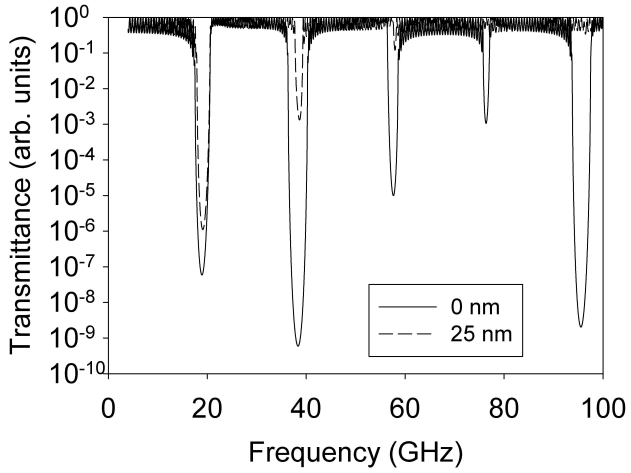

Figure 6.9 Reduction in stopband depth and width for rough interfaces for the case when $\Gamma=0.7$ without interface roughness (0 nm) and roughness applied to porosity profile (25 nm).

The transmission spectra for the cases when Γ=0.2 and 0.7 have been modelled for an interface roughness of 0nm, 2nm, 4nm, 6nm, 10nm, 15nm, 20nm, and 25nm. The stopband depth and width for the M=1,2,3 modes were recorded using the arbitrarily chosen transmission value of 0.1 as described in the last section. The results are shown in figure 6.10 where the data values correspond to the left and right sides of each stopband at the 0.1 transmission value for Γ=0.2 and 0.7 as stated. The fundamental stopband is seen to be the least affected by increasing values of interface roughness and remains open for much higher interface roughness values than for the second and third order harmonics shown. This is despite the fact that the second order stopband has the largest initial bandwidth before interface roughness is applied. This could be due to the fact that higher order modes exist based on more complex interference of the acoustic waves and so are much more easily disrupted by small changes such as interface quality. The third order harmonic bandwidth is heavily dependent on the interface roughness and closes up quickly for relatively small values compared to those needed to close the fundamental stopband.

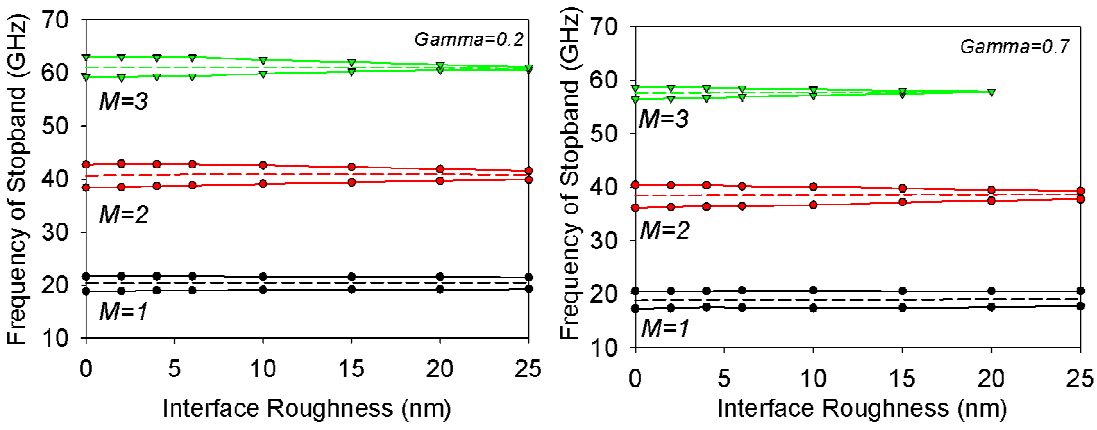

Figure 6.10 Dependence of the first three stopbands on interface roughness for (left) Γ=0.2 and (right) Γ=0.7.

The effect that the interface smoothing has on the bandwidth of the stopbands is similar to that of the rugate structures. The interface is less well defined and causes the higher order stopbands to close up. The overall periodicity of the mulitlayers is not affected by the interface smoothing and the fundamental stopband remains. The bandwidths and stopband positions are not severely affected by interface smoothing

up to 10nm in the regime where the model is reliable. Up to 10nm reduction in bandwidth is seen and this could be as a result of the interface roughness having a larger influence on the depths of the stopbands. To investigate this, the depth of the M=1 to M=5 stopbands were recorded for each value of interface roughness and the dependence of the stopband depths on interface roughness are shown in figure 6.11.

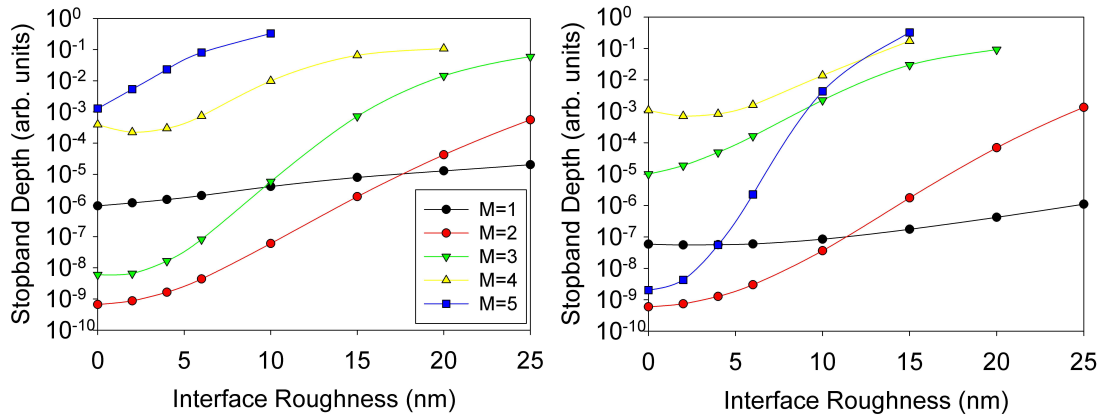

Figure 6.11 The dependence of each stopband depth on interface roughness for (left) Γ=0.2 and (right) 0.7.

Interestingly, the initial depth of the stopband without imposed interface roughness does not affect the order at which the stopbands close when interface roughness is imposed. The highest order modes M=5 close first, with the fundamental mode being least affected by the interface roughness between the layers of the stack. For the case of Γ=0.7 shown in figure 6.11 (right) the M=5 mode is deep and heavily suppressed by the introduction of surface roughness and closes before the M=3 and M=4 modes which initially are not as deep.

This chapter has described the method used to model the acoustic response of multilayered pSi. The TMM enables Bragg mirrors and rugate filters to be modelled by considering the reflection coefficients at each interface so that an overall effect of the multilayer can be found. The acoustic simulations were used to investigate the effect that Bragg mirror symmetry has on the stopband modes. The effect of interface roughness between the layers of the Bragg mirror designed for use at higher frequencies has been studied, where the fundamental mode was located at 20 GHz. It was found that the stopbands close up for increasing interface roughness and that the higher order modes are more heavily affected.

7. Experimental Measurements of Porous Silicon Multilayers

Using the acoustic impedance dependence on porosity found from characterisation measurements, pSi multilayers have been fabricated which have acoustic stopbands with fundamental modes at a frequency of 1 GHz. The higher order modes of the multilayer pSi mirrors depend on the symmetry of the Bragg mirrors and this has been investigated. PSi Bragg mirrors, rugate and Fabry-Perot filters have been fabricated and acoustic transmission measurements through the pSi multilayers have shown stopbands where a select range of frequencies have not been transmitted through the porous layers. Refer to the appendix section for sample details.

7.1 Bragg Mirrors

All experimental measurements presented in this chapter have been normalised by dividing the measured spectra by the response of the transducers unless otherwise stated. As previously discussed in chapter 3, the transmittance properties of a Bragg mirror depends upon the acoustic impedance of each layer in the stack and the number of pairs of layers as in equation (3.6). The more layers used, the stronger the Bragg mirror's reflectance and the lower the transmittance through the multilayer. No stopband will emerge from a Bragg mirror with too few layers and only modulations from impedance mismatching from each side of the mirror will be seen as shown in figure 7.1, where the measurement has not been normalised.

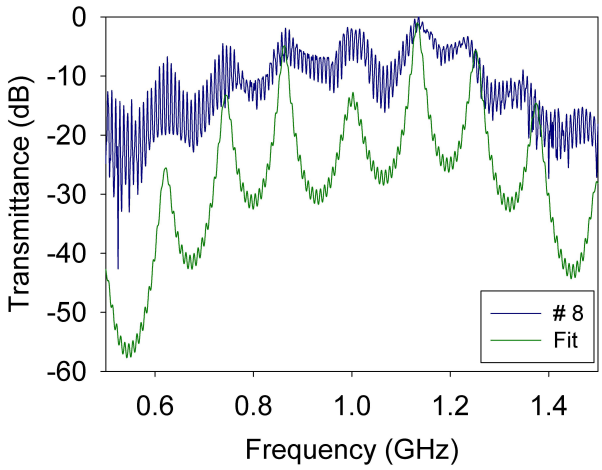

Figure 7.1 Transmission spectrum observed from a Bragg mirror sample without enough layers to produce a stopband at 1 GHz, the mirror has 8 pairs of layers.

As shown in figure 7.2 below, when the number of pairs of layers is increased the reflectivity of the Bragg mirror is improved leading to a deeper stopband seen in a transmission measurement. The samples have the following parameters where p_1~0.63 and p_2~0.70, with thicknesses of d_1=1.19μm, d_2=1.33μm and N=5 for sample #44, d_1=1.28μm, d_2=1.23μm and N=10 for sample #45, d_1=1.28μm, d_2=1.23μm and N=15 for sample #46. SEMs of the Bragg mirrors are shown in figure 7.2. With only 5 pairs of layers, as in sample #44, there are not enough repeats in the cell period for a stopband to emerge but as this is increased to 10 pairs of layers, as in sample #45, the Bragg mirror becomes sufficiently reflective for a stopband to be observed. The Bragg mirror shown with the greatest number of layers (15 pairs) has the deepest stopband, as for sample #46, and it can be seen that the noise floor on the VNA has been reached with the rough nature of the bottom of the stopband in comparison to the smoother oscillations seen for less pairs of layers. The high frequency modulation across the observed spectrum is due to reflections within the transducers and the lower frequency oscillations seen either side of the stopband is due to reflections between the pSi Bragg mirror and the transducers.

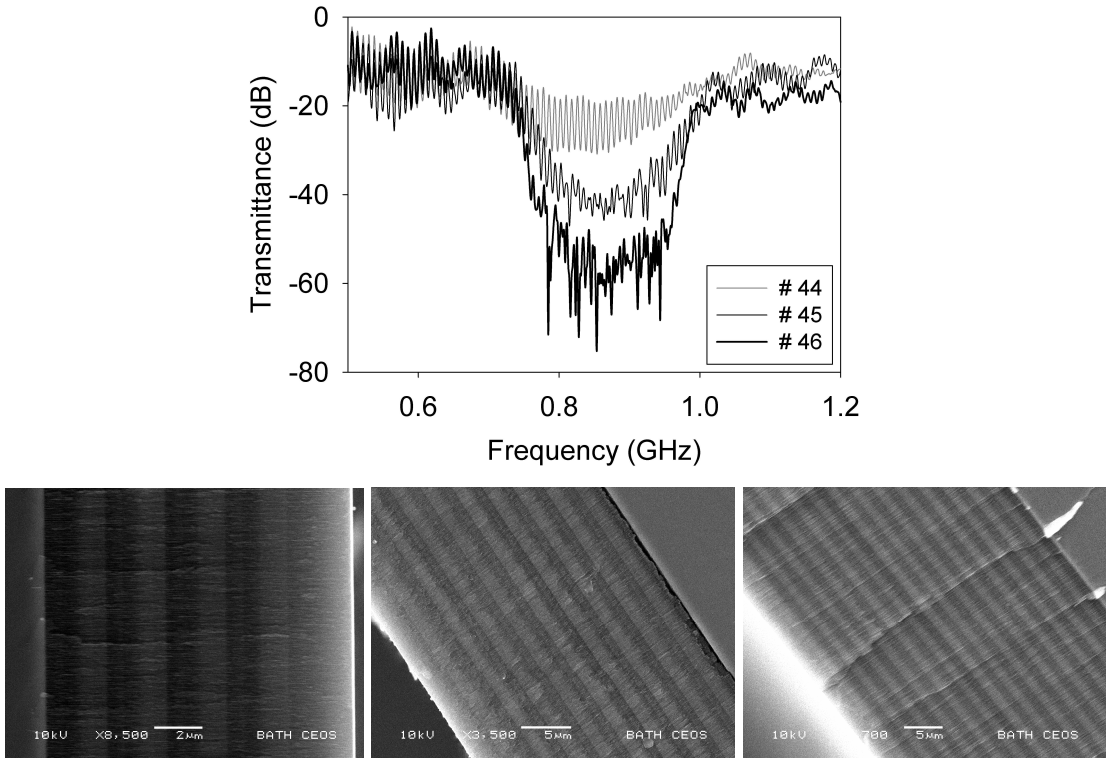

Figure 7.2 (Top) Effect of the number of layers in a Bragg mirror on the stopband depth and (Bottom) SEMs of the Bragg mirror samples (left) #44, (middle) #45 and (right) #46 with N=5, 10 and 15 pairs of layers respectively.

The porosity of the AB layers of the Bragg mirrors fabricated have been chosen to control the width of the stopband observed for each mirror and the thicknesses of the layers were chosen to obtain the fundamental stopband at a specific frequency. Two examples of pSi Bragg mirrors are shown in figure 7.3 where the fundamental frequency of sample #2 is centred at 1.2 GHz with a 0.2 GHz bandwidth, and sample #1 is centred at 0.9 GHz with a bandwidth of 0.36 GHz which gives a fractional bandwidth of 40%. This fractional bandwidth is large and for pSi Bragg mirrors, this is easily obtainable. The stopband shown for sample #1 is also very deep with a measured 50 dB rejection, this is the limit of band rejection that can be measured using the VNA equipment as the noise floor was reached. The depth of the Bragg mirrors shown in the acoustic measurements given in figure 7.2 are in good agreement with the theoretical stopband depth calculated for this particular Bragg mirror previously given in figure 3.5 (left).

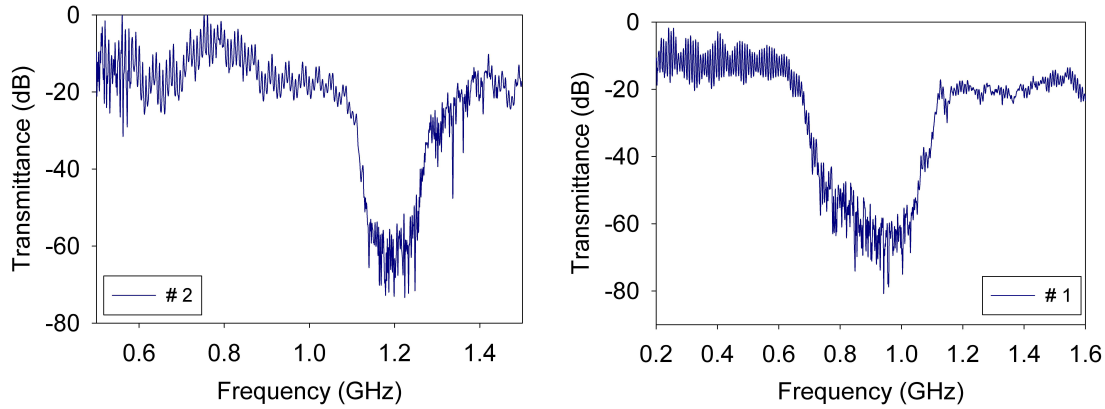

Figure 7.3 Transmission through pSi Bragg mirrors showing rejection bands centred at (Left) 1.2 GHz and (Right) 0.9 GHz.

7.1.1 Symmetric and Asymmetric Bragg Mirrors

As discussed in chapter 3 the response of a Bragg mirror will depend upon the properties of the layers making up the multilayer. Since the velocity of longitudinal waves through pSi depend upon the porosity, the time of flight of waves within each layer will depend on the porosity and the layer thickness. In order to obtain the same time of flight $\tau_1=\tau_2$ of waves in each of the A and B layers, the higher porosity layers through which the waves travel faster, must be thicker than the lower porosity layers. By adjusting the porosity and thickness of the AB layers accordingly, the Bragg mirror's symmetry can be controlled. A number of Bragg mirrors with different degrees of symmetry were fabricated and the transmission properties of each mirror was measured using the experimental set-up described in chapter 5.4. For the balanced Bragg mirrors with $\tau_1=\tau_2$ only the fundamental mode and higher order odd modes were observed, as shown in figure 7.4 (left). The fundamental mode is located at 0.55 GHz with a 0.22 GHz bandwidth (fractional bandwidth of 40%) and 50dB rejection, the M=3 higher order mode is measured at 1.65 GHz with at least 20dB rejection. The times of flights in the A and B layers for this particular sample were ~0.5ns.

For the unbalanced pSi Bragg mirrors fabricated, the time of flights are not the same, $\tau_1\neq\tau_2$ and both odd and even higher orders were observed in the transmission

measurements. An example of an unbalanced pSi Bragg mirror is shown in figure 7.4 (right), and it can be seen that there are four stop bands within the measurable range. The fundamental mode is located at 0.7 GHz with bandwidth of 0.17 GHz, and higher order modes are located at higher frequencies with the M=2 mode at 1.4 GHz, M=3 at 2.1 GHz and M=4 at 2.8GHz. The experimental data is in excellent agreement with the simulated response of this Bragg mirror with the porosity and thicknesses parameters fabricated. The simulated fit shows agreement of the measured stopband depth at the M=3 mode, however the measured stopband depths of the other modes are not as deep as the fitted data due to experimental limitations. The locations of the stopbands that were measured coincide with the predicted bandgap positions.

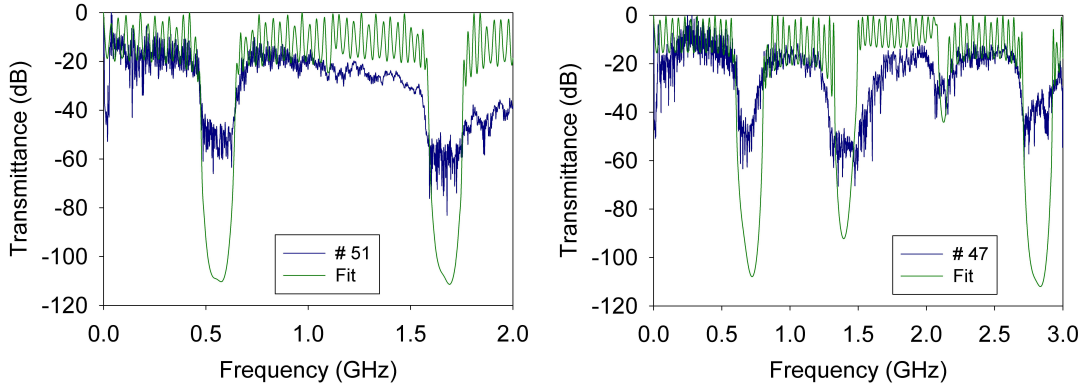

Figure 7.4 Transmission through pSi Bragg mirrors that are (Left) balanced showing odd modes M=1 and M=3, and (Right) unbalanced exhibiting four stop bands for both odd and even modes.

7.1.2 Effect of Etch Breaks on Porous Silicon Bragg Mirrors

The fabrication of micron-thick pSi layers by electrochemical etching requires the inclusion of etch breaks to obtain consistent porosities. The inclusion of etch breaks was investigated and it was found that the position at which etch breaks were included in the etch cycle affect the properties of the mirrors. For example, two Bragg mirrors were fabricated from the same piece of P++ Si wafer using identical current densities and etch times. This produced two Bragg mirrors, each with the 'A' layer of thickness

d_1~2.1µm and the 'B' layer of thickness d_2~1.7µm which was confirmed by SEM measurement. The transmittance of these 'identical' Bragg mirrors is shown in figure 7.5. Using the Bruggeman EMA to analyse both Bragg mirrors to find the layer porosities, whilst keeping other parameters such as the coupling liquid used during experimental measurement constant, the porosities of the 'A' and 'B' layers were found to change by ~2%. This accounts for the 14 % shift (80 MHz) shift in stopband location seen for the M=3 mode for sample #51 when compared to sample #50.

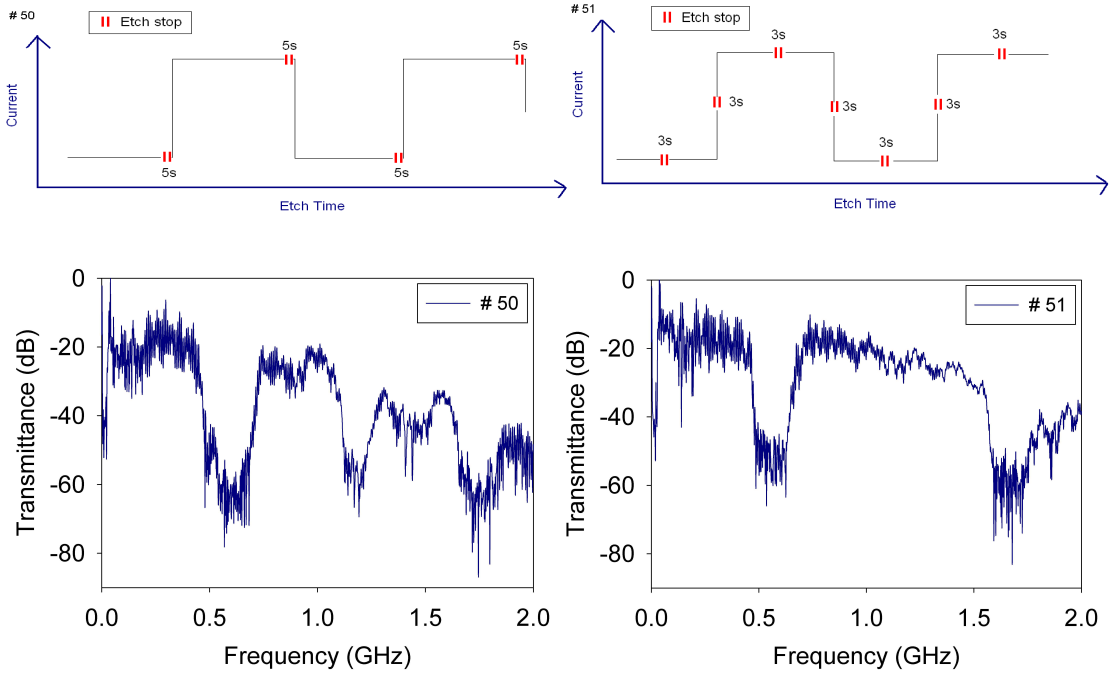

Figure 7.5 (Left) Bragg mirror #50 compared with (right) Bragg mirror #51, this mirror has the lowest frequency stopband observed in this investigation.

The fundamental stopband of each mirror is located at 0.57 GHz with a bandwidth of 0.25 GHz. It can clearly be seen that sample #50 has a second order mode at 1.14 GHz whereas sample #51 has no second order mode. For the layer porosities and thicknesses etched, both of these Bragg mirrors should be balanced and have a symmetry of 1, i.e. the ratio of the time taken for acoustic waves to travel through the A and B layers of the mirror, τ_1 and τ_2 respectively, is $\tau_1/\tau_2=1$. Therefore, neither mirror should exhibit even ordered modes.

The change in porosity between the two Bragg mirrors of ~2% does not account for the appearance of the even mode for the Bragg mirror sample #50. The only difference in the etch parameters between the two 'identical' Bragg mirrors are the positions of the etch stops. These are shown at the top of figure 7.5 where 5s etch stops were included at each current density step for sample #50 (i.e. two etch breaks per AB pair). For sample #51, etch stops of 3s were included at each current density step and additionally mid-layer during fabrication (i.e. four etch breaks per AB pair). The inclusion of the additional etch break for sample #51 has given a more uniform porosity through each layer of the Bragg mirror. An additional etch break was needed to prevent chirp in the porosity of each layer for sample #50 since this has the affected transmittance properties of the mirror and a second order stopband has been observed.

7.2 Rugate Filters

The first pSi optical rugate filter made by electrochemical etching was by Berger et al[106] and only now have the first rugate filters based on pSi been fabricated for acoustic applications. In order to effectively represent a continuously varying porosity profile that is used to describe a rugate structure, the number of steps used during the electrochemical etching process has been taken into consideration. For instance, using only one step between two layers A and B of different porosity will represent a Bragg mirror, but including an additional number of steps between layers A and B will create a smoother transition from one porous layer to another. From looking at the simulated transmittance properties of a pSi based Bragg mirror, and then gradually increasing the number of steps in porosity between the layers A and B, it was possible to obtain the minimum steps needed in order to suppress higher order modes and create an equivalent response representing that of a rugate filter. The minimum number of steps required, based on modelling, was 8 steps per A or B layer (16 steps per unit cell) where the pSi rugate filters showed heavily suppressed higher order modes. Figure 7.6 shows a Bragg mirror and rugate filter both with symmetry of τ_1/τ_2=0.8 with the same AB layer porosities. The thickness of the AB layers for the rugate filter sample #38 are slightly higher than those for the Bragg mirror, hence the location of the fundamental mode at 0.68 GHz at a lower frequency, when compared to the Bragg mirror sample #37 at 0.83 GHz. The symmetry of both mirrors is the

same and the rugate profile shows an almost non-existent second order mode, with the Bragg mirror showing a second order mode near 1.6 GHz. The rugate filter has a reduced bandwidth of 0.16 GHz for the rugate filter compared to the bandwidth of 0.24 GHz for the Bragg mirror, this is 67% of the Bragg mirror's bandwidth.

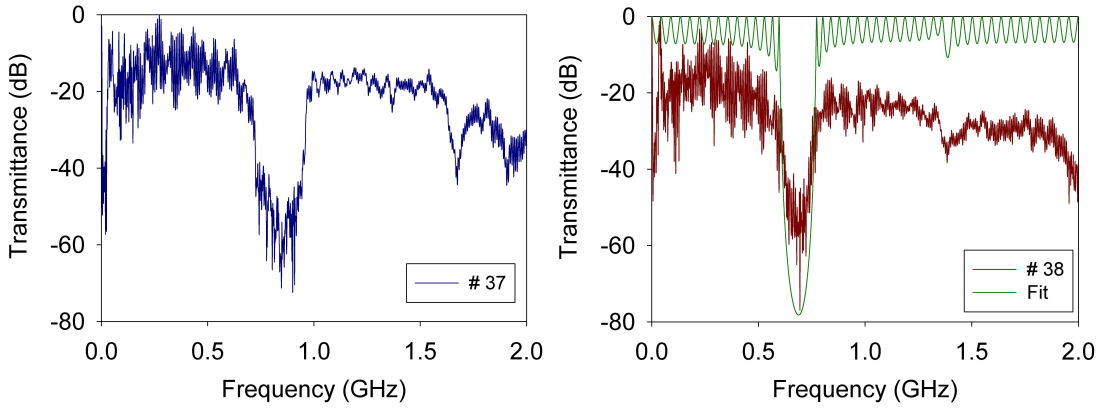

Figure 7.6 (left) Bragg mirror and (right) rugate filter with fit, with the same AB layer porosities of p_1=0.43 and p_2=0.57.

Samples #42 and #43 have the same nominal maximum and minimum porosities and number of etch cycles to compare the properties of a Bragg and rugate porosity profile. The expectation is that the fundamental stop band bandwidth of the rugate filter is π/4 or (78%) that of the bandwidth of the Bragg mirror.[107] This is the case for the simulated data presented in chapter 3. However the measured rugate filter bandwidth of figure 7.7 is 68% that of the Bragg mirror equivalent bandwidth. Due to the transmission measurement being limited by the noise floor of the VNA and transducers, the depth of the measured stop bands were limited while the simulation is lossless. The transmittance of samples #42 and #43 shown in figure 7.7 have the same measured fundamental stopband depth of 40 dB, with sample #42 having a fundamental Bragg frequency of 0.64 GHz and bandwidth of 0.25 GHz. The higher order harmonic of the rugate filter sample #43 is heavily suppressed. Measurements at higher frequencies for this particular rugate filter and Bragg mirror were noisy so only frequencies up to 1.5 GHz have been shown.

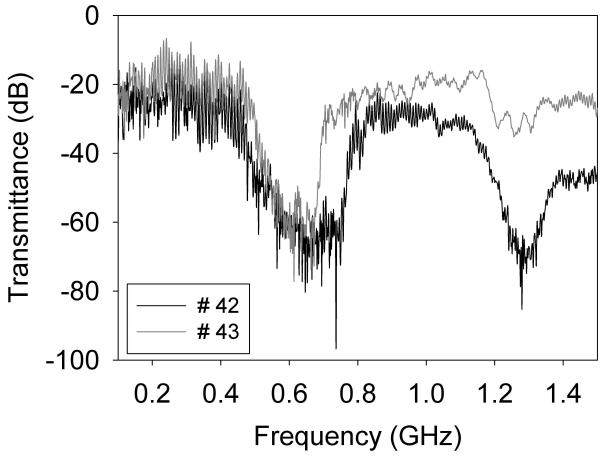

Figure 7.7 Reduction of higher orders for a rugate filter compared to a Bragg mirror.

The optical response of a Bragg mirror and rugate filter with the same layer thicknesses and porosities was measured and the result shown in figure 7.8, where the Bragg mirror is shown on the left and the rugate filter is shown on the right. Note that both of these mirrors displayed stopbands at a frequency of 1.13 GHz with bandwidths around 100 MHz. The effective refractive index of layer A was n_1~1.9 and for layer B was n_2~1.8 with N=20 pairs of layers. The high order optical modes for the Bragg mirror are located in this infrared region of the spectrum at 1.02 μm and 1.22 μm. Using equation (3.19) and substituting the correct effective refractive index and thickness for each of the layers, these modes are found to be the M=7 and M=6 modes respectively. The stronger peak seen is an odd mode and these mirrors had symmetry of 0.95; the even mode is not seen for the rugate filter.

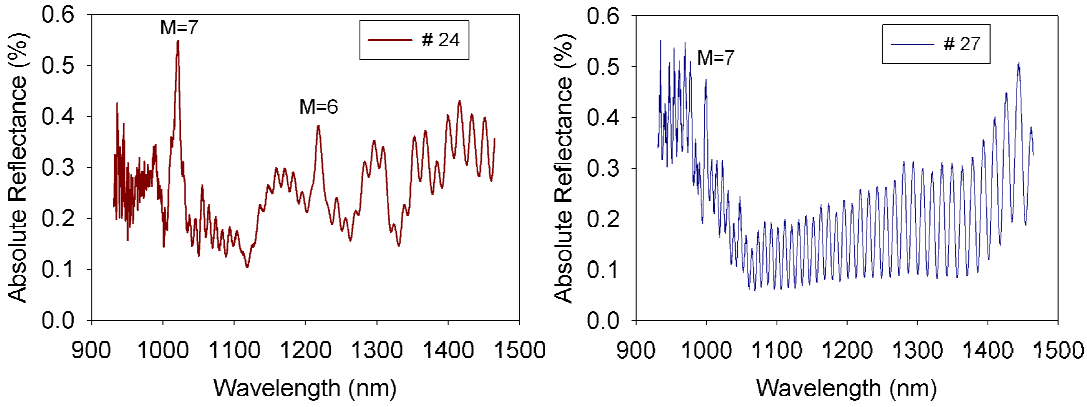

Figure 7.8 Optical response of a (left) Bragg mirror and (right) rugate filter in the infrared region of the spectrum.

7.2.1 Effect of Etch Breaks on Porous Silicon Rugate Filters

The effect of the inclusion of etch breaks during the fabrication process of pSi rugate filters has been investigated in this section. Sample #26 was etched without the inclusion of etch breaks and sample #27 was etched with the inclusion of etch breaks. The acoustic response through both of these rugate filter samples is shown below in figure 7.9 where it can be seen that for the mirror etched without etch breaks, the fundamental stopband was located at a lower frequency than that of the other sample. This stopband shift towards a lower frequency is the consequence of chirp across the mirror. Without the inclusion of etch breaks the etch rate decreases due to the excess hydrogen bubbles in the porous layer. This leads to thinner layers with a chirp in porosity across the mirror. However, a chirped Bragg mirror that has thinner layers will have a fundamental stopband located at higher frequencies than that of an unchirped Bragg mirror with thicker layers. The shift in the stopband location towards lower frequencies for the chirped mirror is due to the increase in porosity of the layers which has a stronger influence on stopband location than layer chirp. The chirp on the porosity for sample #26 has a greater influence on stopband location than the chirp on the layer thickness.

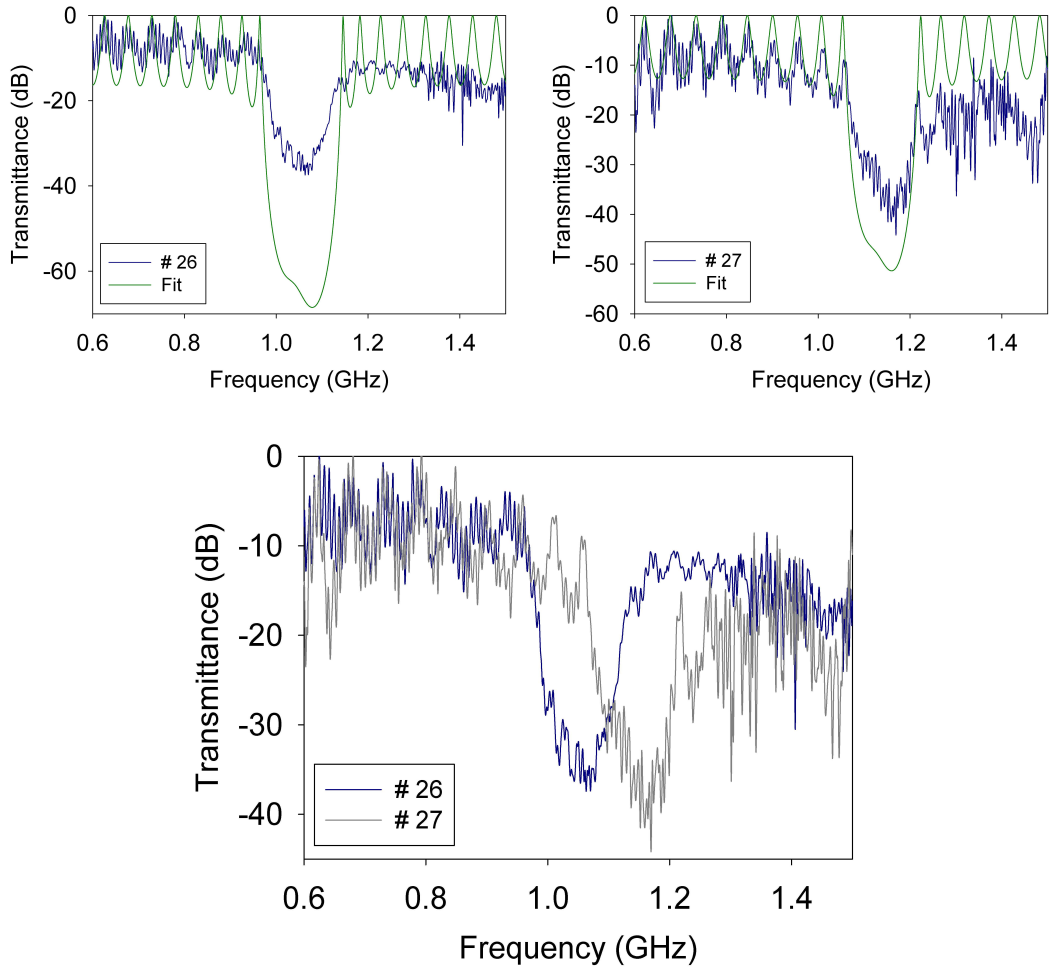

Figure 7.9 Rugate filter without (top left) and with etch breaks (top right) with simulated fit to experimental data and the direct comparison of the two data (below).

Figure 7.9 has demonstrated the significant effect that inclusion of etch breaks during the fabrication of the samples has on the stopband properties of the resulting acoustic filter.

7.2.2 Porous Silicon Acoustic Rugate Filter with a Single Stopband

In order to fabricate an acoustic rugate filter that exhibits only the fundamental stopband, careful consideration has to be given to the symmetry of the mirror, the conditions under which it is fabricated, for example the inclusion of etch breaks, and to the acoustic impedance profile of the mirror. A pSi rugate filter has been fabricated using the etch cycle previously shown in figure 4.10 of chapter 4. The inclusion of etch breaks were important to avoid chirp on the mirror and the mirror symmetry was designed to have $\tau_1/\tau_2=1$ so that only odd order modes would be exhibited. Finally, the acoustic impedance profile of the mirror was important in the reduction of higher order modes. The acoustic response of this rugate filter designed to exhibit only the fundamental mode near 1 GHz is shown below in figure 7.10 and no higher order modes are observed.

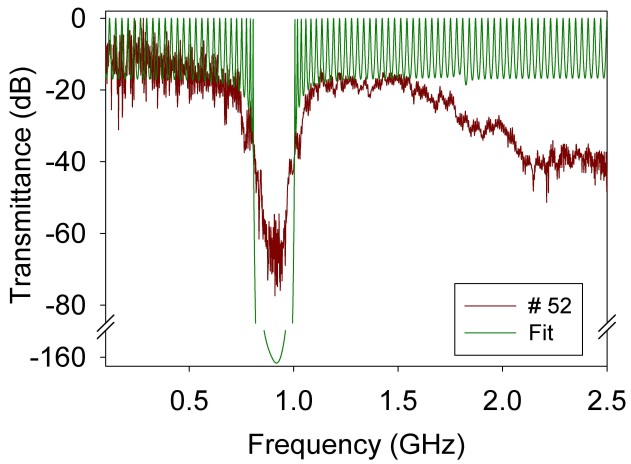

Figure 7.10 PSi acoustic rugate filter exhibiting only the fundamental stopband at 0.95 GHz with bandwidth of 0.2 GHz and stopband depth of 40 dB.

7.3 Fabry-Perot Filters (Microcavities)

Acoustic microcavities have been designed using the insertion of a defect layer sandwiched between two Bragg mirrors that gives rise to a transmission peak within the stopband. The microcavities were designed to have fundamental stopbands near 1 GHz and the first acoustic microcavity measured for this investigation is shown in figure 7.11 where the transmission peak is observed in the stopband. The wide transmission peak for this sample gives the microcavity a Q-factor ~ 90. The Q-factors were found using the ratio of the central stopband frequency to the transmission peak bandwidth i.e. $f_c/\Delta f$ at the FWHM of the transmission peak.

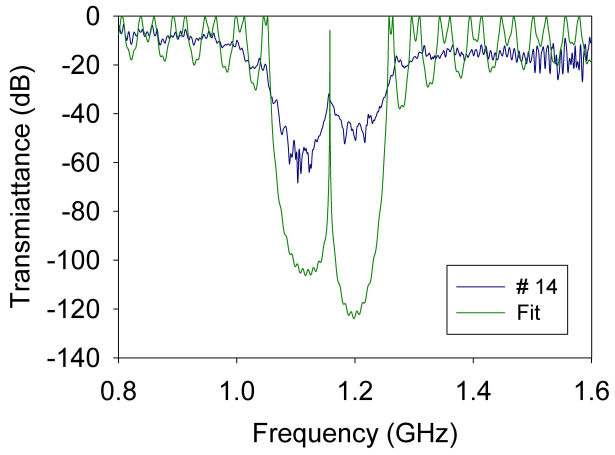

Figure 7.11 A pSi based acoustic microcavity exhibiting a stopband at 1.16 GHz with bandwidth 0.21 GHz, with a central transmission peak in the stopband for Q-factor ~ 90.

The design of the pSi microcavity was changed to obtain a fundamental stopband located closer to 1 GHz. The defect layer thickness was found to affect the location of the transmission peak inside the stopband as expected. The acoustic microcavity samples shown in figure 7.12 below were etched using the same fabrication parameters but with the exception that the defect layer in sample #39 is 2.4 μm and for sample #41 the defect layer is 2.8 μm thick. It can be seen that the thickness of the defect layer affects the location of the transmission peak inside the stopband.

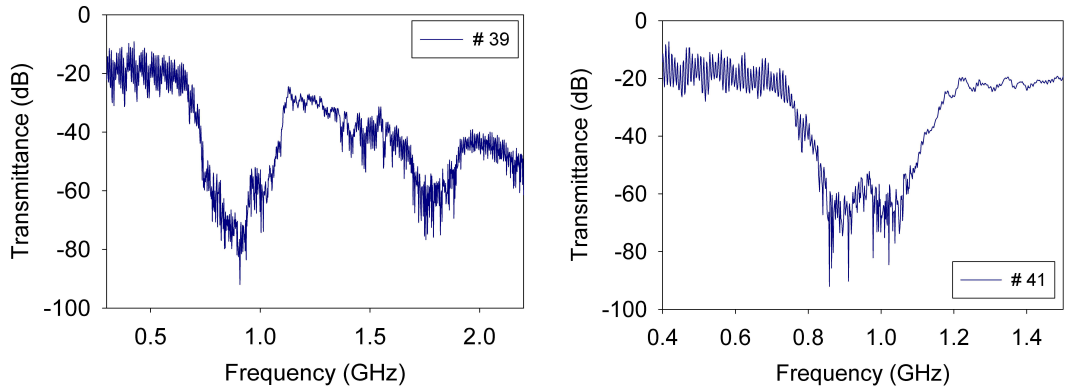

Figure 7.12 (Left) PSi based acoustic microcavity with the fundamental mode at 0.93 GHz with 0.4 GHz bandwidth and 50dB rejection with the second order mode located at 1.8 GHz. (Right) PSi acoustic microcavity previously shown in figure 4.12, with a transmission peak located in the centre of the stopband at 0.97 GHz.

The design of the acoustic pSi microcavities were improved to obtain a microcavity with a higher Q-factor. The Bragg mirrors either side of the defect layer were designed to have a symmetry of $\tau_1/\tau_2=1$ and included etch breaks to prevent chirp on the layers. This is more important for the acoustic microcavity samples because the mirror section is much thicker than that of the Bragg mirrors and rugate filters previously shown. The acoustic microcavities presented here typically have pSi mirror sections that are ~ 80 μm thick. The Bragg mirrors either side of the defect layer used in the microcavity structures had 15 pairs of layers, N=15. The porosity through the defect layer was kept constant and after consideration of these parameters in the design of the pSi microcavity, the Q-factor of the microcavity fabricated was found to be ~ 210 and is shown in figure 7.13 (right).

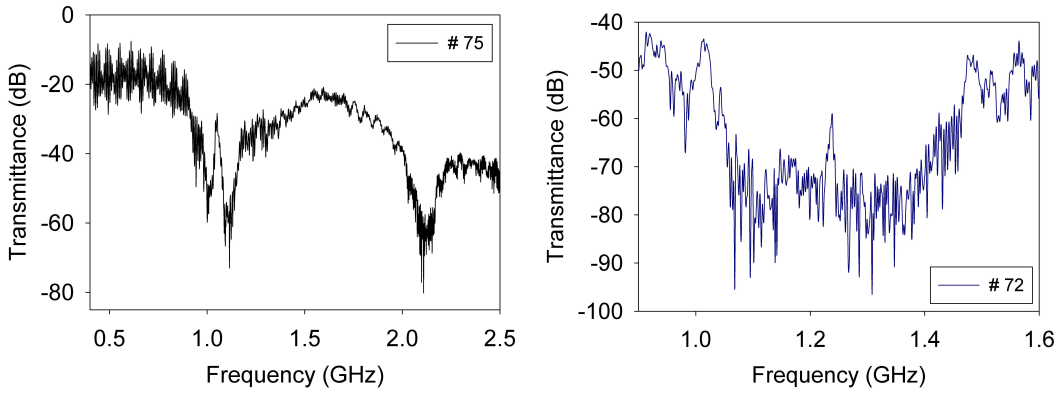

Figure 7.13 (Left) PSi acoustic microcavity with the fundamental mode at 1.06 GHz with 0.2 GHz bandwidth at 30 dB rejection. (Right) PSi acoustic microcavity with the fundamental mode at 1.23 GHz with a bandwidth of 0.4 GHz with 40 dB rejection and Q-factor ~ 210.

The microcavity shown on the left of figure 7.13 was designed to have a more prominent transmission peak inside the stopband. The layer thickness and porosities chosen for the Bragg mirrors either side of the defect layer were chosen to give a lower rejection level of 30 dB rejection so that the transmission peak appears to become more prominent.

7.4 Apodisation and Impedance-Matching

The control over the stopband position and transmission strength has been discussed in chapter 3, where the layer thickness and impedance along with the number of layer repeats, control much of the transmission properties of the pSi mirrors. Due to impedance mismatching of the mirror with the surrounding media, sidelobes appear either side of the main stopband which can reduce the quality of the mirror response. However, there is also some degree of control over the modulation seen in the sidelobes either side of the stopband using apodisation and index-matching. Apodisation has the effect of reducing the sideband oscillations and higher harmonics whilst index-matching layers further suppress sidelobes near the peak.[108] A number of apodisation functions including linear, Gaussian and quintic (fifth order polynomial) functions can be used to suppress the sidelobes and are applied across the entire

impedance profile of the mirror.[109] However, these functions give suppression of the sidelobes with a decrease in the reflectance of the mirrors so an apodisation function, such as a partial Gaussian, can be employed to adequately reduce sidelobes whilst maintaining a high reflectance in the stopband. Index-matching layers used in combination with an apodisation function give the best stopband shape and reflectance with minimal sideband modulations. Figure 7.14 shows an example of an optical rugate filter[110] with and without apodisation and index-matching layers. The apodisation function is applied to the effective refractive index modulation of the pSi rugate filter and index-matching layers are added either side of the mirror.

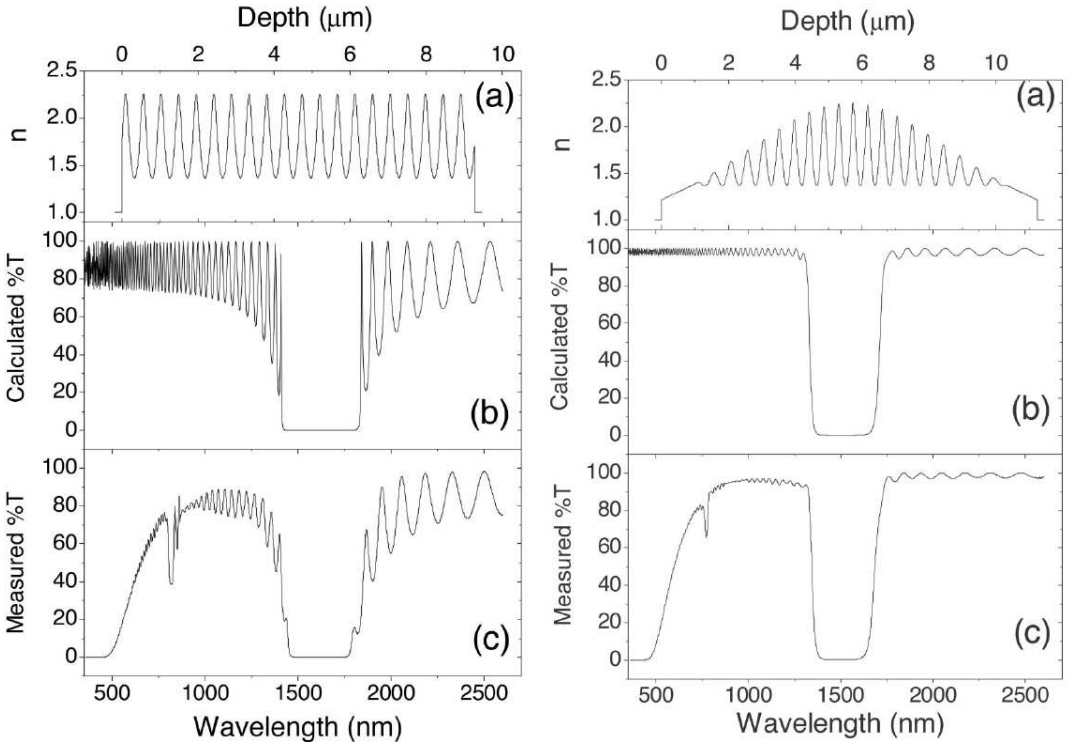

Figure 7.14 PSi rugate filter without (left) and with (right) an apodisation function of sin(x) from 0 to π including index-matching layers giving clear sidelobe suppression.[110]

Apodisation and index-matching layers can be added to the Bragg mirrors and rugate filters designed for acoustic applications that have been described in this thesis. The apodisation of these pSi samples is reasonably straight forward and has been done, however, the addition of index-matching layers for the pSi samples has not been done because it is unclear what acoustic impedance value was needed for index-matching.

The transducers used to measure the samples have ARCs and Ga-In eutectic is used as the coupling liquid in the experimental set-up.

A sine apodisation was applied to samples #83 and #81 without index-matching layers. Sample #83 was fabricated with the same etch parameters as sample #72 shown in figure 7.13 but with a full sine apodisation applied across the impedance profile of the microcavity. The acoustic response of the sine apodised samples are shown in figure 7.15 below. The effect on the acoustic response of the microcavity sample #83 is a wider transmission peak inside the stopband which has well defined vertical sides. The microcavity has the fundamental stopband at 1.19 GHz with a bandwidth of 0.33 GHz and 40 dB rejection.

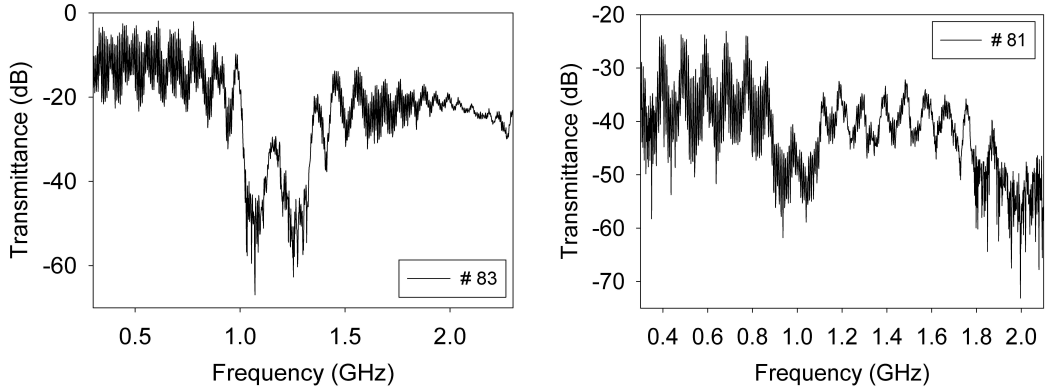

Figure 7.15 (Left) Sine apodised pSi acoustic microcavity and (Right) sine apodised pSi Bragg mirror.

The sine apodised pSi Bragg mirror does not show a well defined stopband. Sample #81 was etched with the same parameters as sample #45 previously shown in figure 7.2 but with a sine apodisation applied across the pSi Bragg mirror. The porosity contrast between layers in the Bragg mirror has been reduced by apodisation and the magnitude of reflection from the mirror has been reduced. Figure 7.16 below highlights the control over the porosity profile of the pSi multilayers where an optical rugate filter with a double band has been fabricated. The superposition of two refractive index profiles has enabled two filters to be superimposed. In future work, two or more acoustic impedance profiles could be superimposed to produce a superposition of acoustic filters.

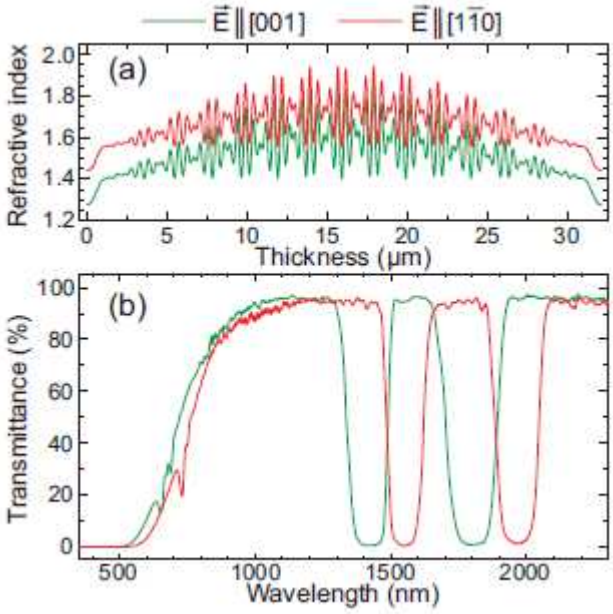

Figure 7.16 Double-band optical rugate filter with two periods and the dependence of the electric field measured in different crystallographic directions.[111]

7.5 Collaborative Work with the University of Nottingham

Since BAW devices in use today can operate at ~ 7 GHz frequencies it is useful to study the suitability of pSi multilayers at frequencies above 1 GHz. As previously discussed in chapter 3 the higher the target operating frequency of the multilayer, the thinner the layers need to be. This section discusses the preliminary investigation of pSi Bragg mirrors designed for use around 20 GHz and the results presented here are from a collaborative effort with members of the physics department at the University of Nottingham[112]. Samples designed for higher frequencies at ~ 20 GHz are roughly an order of magnitude thinner than the thickness of the multilayers designed for < 1 GHz because the frequency scales linearly with layer thickness. For these thinner samples the variation in layer thickness at different points along the sample will be more prominent because interface (and surface) roughness effects become more noticeable. Samples designed for use at higher frequencies are more difficult to fabricate due to the smaller scale of the features determining the response of the

overall structures. More care must be taken to ensure high quality interfaces, for example this can be done for pSi by etching at lower temperatures.

7.5.1 Fabrication and Characterisation of Porous Silicon Multilayers for 20 GHz Applications

In the interest of gauging the potential use of the pSi material for ~20 GHz frequency range, five pSi multilayered samples were designed to have fundamental modes at frequencies up to ~ 20 GHz. Note that the samples described in this section 7.9 are different to samples appearing with the same number elsewhere in the text and whose parameters are given in the appendix. The parameters used during the fabrication of the samples are shown in table 7.1 where the doping level of the Si wafer used for samples 1 - 4 was 1 – 5 mΩ cm (SSP) and for sample 5 was 1 – 10 mΩ cm (DSP). The thickness of the Si wafers prior to etching for samples 1 - 3 was 525 μm, sample 4 was mechanical polished with an optical finish to ~ 80 μm and the sample 5 wafer was 320 μm.

Sample #	I_1 (mA)	I_2 (mA)	t_1 (s)	t_2 (s)	N	p_1	p_2	d_1+d_2 (nm)
1	484	667	1.09	0.89	15	0.68	0.71	192
2	500	600	0.70	0.64	25	0.71	0.75	139
3	500	600	0.52	0.48	25	0.71	0.75	109
4	484	667	1.09	0.89	15	0.70	0.74	255
5	484	667	1.09	0.89	15	0.62	0.66	263

Table 7.1 Etch parameters used for the fabrication of these samples.

All samples were characterised using SEM imaging of the pSi multilayers and the contrast of the image was used to extract a contrast profile across the sample which is analogous to the porosity profile of the pSi section due to the electron densities in the regions of Si material. The SEM images shown in figure 7.17 represent sample 4 where the pSi multilayer on the cSi substrate is shown with detail of the pSi multilayered structure with layers of high and low porosity shown. The overall thickness of the porous mirror region is ~3.8 μm and the cross-section analysis of the

porosity profile gave the thicknesses of the layers. The areas with higher electron densities are seen as lighter areas whereas regions void of material are seen as black.

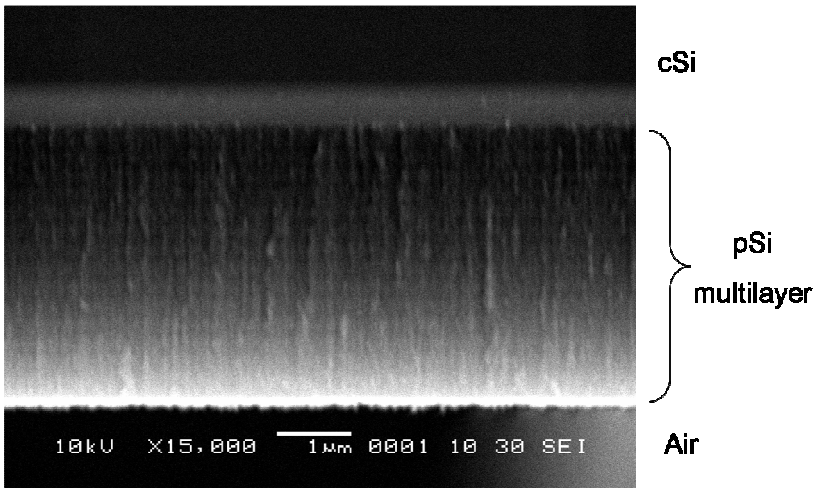

Figure 7.17 SEM image of sample 4 where the pSi Bragg mirror is seen on the substrate with the pSi multilayer shown with dark areas indicating high porosity and light areas low porosity.

The layers were seen on the contrast profile with the porosity change associated with the layer interfaces so the thickness of one pair of layers (d_1+d_2) was deduced and a mean value taken for all of the layers. For sample 4 the thickness of one pair was 255 nm. Using the layer thickness measurements, the porosities of the layers were determined. Fitting the measured optical response using the experimental set-up previously described by figure 5.1 using the thickness parameters found from the SEM images, the porosities can be determined. An example of the optical spectra obtained from sample 4 is given below in figure 7.18 where it can be seen that the first order stopband is located in the visible region at 780 nm due to the individual layers being hundreds of nanometers thick for application at frequencies of ~ 20 GHz. The interference fringes of the simulated data were fitted to the measured spectra to obtain the layer porosities. The slowly varying reflectance modulation at shorter wavelengths seen superimposed on the measured stopband could be as a result of the mechanical polishing of the wafer before the pSi sample was etched. This caused the slight mismatch of spectra between the measured and simulated data, however this is

unimportant because only the interference fringes from the multilayer itself are needed to deduce the porosities using the fringe spacing either side of the stopband.

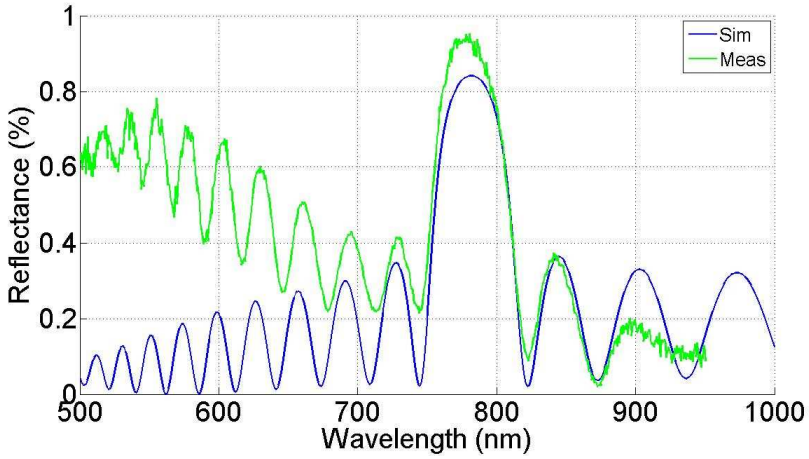

Figure 7.18 Optical response of sample 4 showing the measured and fitted data.

Using the parameters for layer thickness and porosity found for the multilayers by characterisation techniques, the location of the band-gaps can be predicted as shown in figure 7.19.

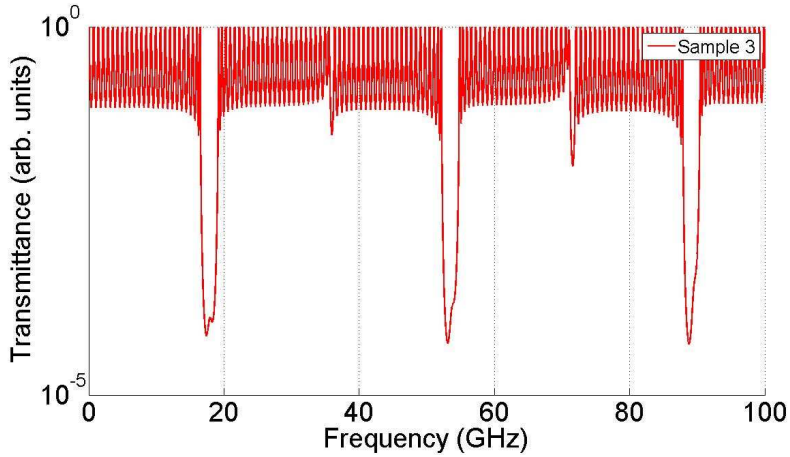

Figure 7.19 Predicted locations of the band-gaps based on the measured layer thicknesses and porosities deduced from optical response data for sample 3.

7.5.2 Pump-Probe Experiment on Porous Silicon Multilayers for 20 GHz Applications

Once the pSi multilayers had been characterised the acoustic response of the pSi layers was measured by the University of Nottingham using a pump-probe experiment. Pump light pulses incident on the surface generate bulk acoustic waves that propagate though the layers and the echo is studied using a probe pulse where the multiple reflections due to impedance mismatching from the multilayer structure are seen in the reflected signal measured using a photo-detector (figure 7.20). This is a non-destructive technique. A laser with low 5 kHz repetition rate and short pulse duration <100 fs gave a high power pulse incident on the surface of the pSi multilayer. The femtosecond laser had a pump wavelength of 800 nm that was focussed and incident on a thin Al layer on the surface of the pSi multilayer. The photons are absorbed in a thin layer of the Al film surface and the absorption of energy at the surface generated a strain pulse due to the expansion of material from the temperature change. Pressure waves were generated that propagated into the pSi layers and the change in pressure of the material gives rise to a change in the local refractive index due to the stress-optic effect. The propagating waves are reflected and transmitted at boundaries with an impedance mismatch, such as at the boundaries between individual layers, so that when the echo returns the pressure waves create a change in the reflectance at the pSi surface. This reflectance change due to the changing refractive index is detected by the probe wavelength. A delay introduced between the pump and probe wavelength using a partially reflective mirror and translation stage gave a time delay in the arrival of the reflected propagating waves resolved by the photo-detector. The time-resolved measurement does not detect changes in vibration at the film surface, it detects changes in the local refractive index due to stress pulses in the material.

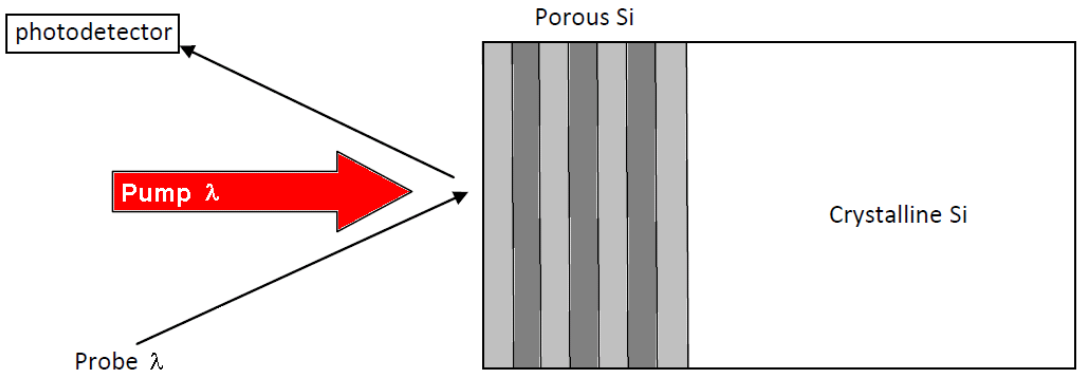

Figure 7.20 Pump-probe experimental set-up to measure the response of the pSi multilayers.

The detected light pulses as a function of time are shown in the insets of figure 7.21 where the initial change in reflectivity is due to the arrival of the pulse at the surface of the pSi. The oscillations in reflectance can be seen over time; in order to study the acoustic waves due to stress-optic effects the background reflectance changes are subtracted. The reflectance changes are recorded scanning the delay time from zero to 500 ps. It is assumed that the focussed spot size (order of microns) is large compared to the wavelength of the propagating waves meaning that plane waves propagate through the material. Measurement of the period of the strain oscillation gives oscillations corresponding to phonons of a certain frequency. This data set is Fourier transformed to image reflectance peaks at each corresponding frequency which represent coherent elastic vibrations in the pSi nano-structure. The time window chosen to perform the Fourier transform determines the resolution of the peaks in the frequency domain where a shorter time window leads to a lower resolution in frequency. The spectra measured for samples 2 and 4 are shown in figure 7.21 where coherent elastic oscillations with a frequency of 40 GHz are predominantly seen for sample 4. It is unclear whether the reflectance peaks seen using this pump-probe experimental approach are identical to the stopband locations observed using acoustic transmission measurement technique. The dispersive properties of the pSi material are unknown so dispersion effects depending on frequency are unknown. The quality of samples designed for higher frequencies of 20 GHz is likely to be lower than those designed for lower frequencies at 1 GHz due to the thinner layer thicknesses chosen. The echo shape can indicate the roughness of a boundary or surface since the pulse

broadens on reflection. The effects of heating due to the femtosecond laser is unknown, however it is reasonable to assume that some effects due to oxidation within the pSi layers will exist in the 20 μm spot size of the incident laser. This will cause the frequency of the coherent oscillations to shift.

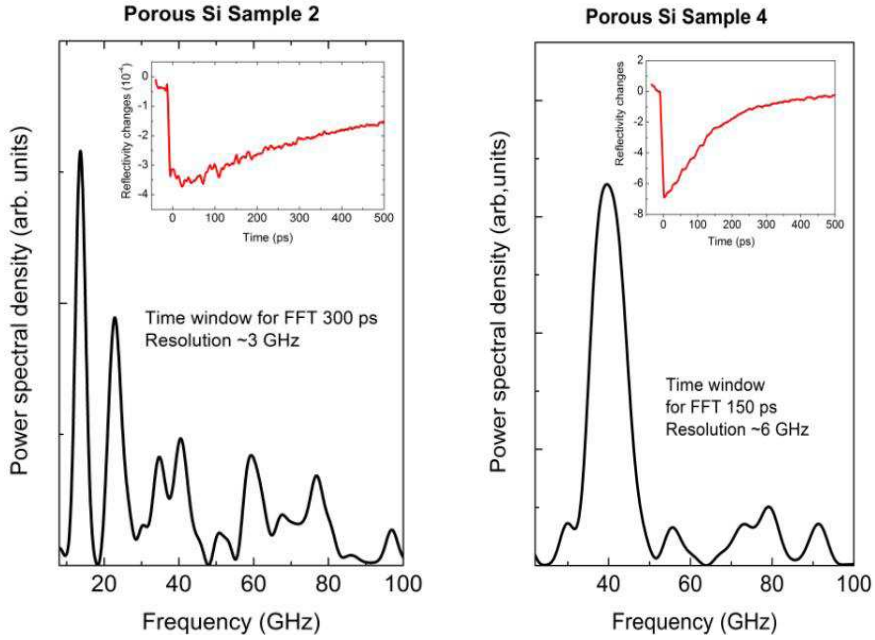

Figure 7.21 The pump-probe spectra measured for samples 2 (left) and 4 (right).

The coherent oscillations measured on sample 3 is given in figure 7.22 for the different areas measured for sample 3. Five points on the surface of the sample were chosen (1-5) and measured twice (a or b). For detection points 1a, 5a and 5b the first coherent peak is around 20 GHz and oscillations are seen at later times, possibly corresponding to higher order modes where the second echoes return. The spectrum gathered at detection point 4a shows a variation compared to the other detection points. This could be due to sample quality, heating effects or dispersive effects.

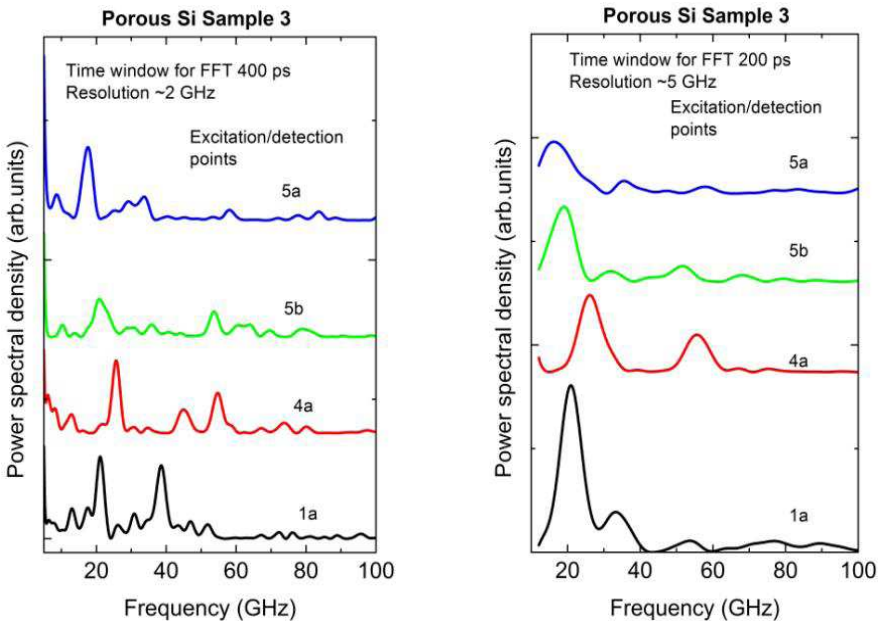

Figure 7.22 The pump-probe spectra measured for sample 3 for different areas on the surface of the pSi multilayer for (left) 2 GHz and (right) 5 GHz resolutions.

PSi multilayered mirrors for acoustic applications have been shown in this chapter. PSi based Bragg mirrors have been designed to possess certain layer thicknesses and porosities for desired acoustic responses of the mirrors. Bragg mirrors with the fundamental stopband near 1 GHz have been designed and fabricated and acoustic transmission measurements through the mirrors have shown the existence of stopbands. Deeper stopbands have been observed in the pSi Bragg mirrors when the numbers of bilayers in the mirrors were increased. A study on the effect of Bragg mirror symmetry on the stopbands observed in the transmission spectra of the mirrors showed that balanced Bragg mirrors only exhibited odd order modes, and unbalanced mirrors exhibited both odd and even order modes. The effect of including etch breaks during the fabrication of the pSi multilayers has been investigated and it was found that the positioning of the etch breaks during the fabrication process is important if a balanced mirror is needed. PSi based acoustic rugate filters with the fundamental mode near 1 GHz have been fabricated using a sinusoidal variation in the acoustic impedance profile of the multilayer stack. An acoustic rugate filter was fabricated where no higher order modes were observed due to the symmetry of the mirror

chosen. The pSi rugate filters showed suppressed higher order modes in comparison to the pSi Bragg mirrors as expected. The importance of the inclusion of etch breaks during the fabrication process was highlighted comparing the acoustic transmission through a rugate filter made with and without the inclusion of etch breaks during fabrication. The rugate filter without etch breaks during fabrication showed a stopband shifted towards lower frequencies as would be expected for a chirped mirror with higher porosity layers. The acoustic response of pSi Fabry-Perot filters showed transmission peaks in the stopbands. These microcavity filters were found to have Q-factors around 165. These pSi Fabry-Perot filters can be optimised in future studies to obtain Q-factors closer to those currently used in industry. Using pSi material gives control over the porosity, and hence acoustic impedance variation, throughout the multilayer. PSi Bragg mirrors with apodisation applied to the impedance profile were briefly investigated and the effect of apodisation observed in the acoustic transmission measurements. PSi based Bragg mirrors for acoustic frequencies near 20 GHz were fabricated for collaborative research and preliminary results showed the existence of stopbands at these higher frequencies. At higher frequencies the acoustic loss in pSi becomes more apparent due to dispersion effects and loss due to scattering at interfaces within the mirrors. The next chapter discusses the acoustic loss measured for a small set of pSi samples and the elastic properties of pSi are also discussed.

8 Loss and Elastic Properties of Porous Silicon

In chapter 2, the constants describing the elastic properties of a cubic material were discussed and understanding the elastic properties of a material enables the prediction of how the material may behave under different conditions. The behaviour of Si in its porous form can be modelled using a selection of theoretical predictions, each of which has been developed for a different set of assumptions. The many morphologies of pSi make it difficult to accurately model because the pore size and morphology changes depending on doping level and fabrication conditions. The filling of the pores also influences the elastic behaviour of the material. For example, the porous nature of some rocks, such as sandstone, will reflect acoustic waves differently under separate conditions such as for dry and saturated (below water table) circumstances. The porous rock can be modelled as a porous medium with pores that are air-filled or completely filled with liquid. Ultrasonic properties of bone, also a porous material, have been studied to understand multiple reflections for medical diagnosis. Some materials are deliberately made to include pores in order to form an acoustic absorber such as acoustic insulation for buildings to keep out the noise of traffic. Much of the naturally occurring porous materials are randomly ordered and anisotropic. Porous Si-based films have a degree of periodicity in one or more crystallographic directions and are anisotropic in nature. PSi can be described as a cellular solid with an open pore structure. The pores are open at one end and inter-connected by nano-cSi bridges, the pores are closed at the substrate end. Cellular solids have a regular structure and the cell structure determines the modified mechanical properties of the parent material.[113] Given the various forms of porous media and the enormous differences in morphology at the microscopic level, a unified theory of the elastic properties of porous media is not available. PSi itself has a large range of pore morphologies controlled by wafer doping so it is difficult to develop an elastic property theory for Si in its porous form independent of pore size and morphology. However, it is possible to exploit similarities between porous media theories to apply a suitable model to the mesoporous Si used in this investigation. An attempt to predict some of the elastic properties of pSi has been made and is discussed in this chapter. In

addition to discussing elastic properties of pSi, the attenuation of acoustic waves through pSi is also discussed. It is important to investigate loss in this pSi material for acoustic applications because when using pSi material as a multilayer, the bandgaps seen in multilayered systems are smaller when the attenuation of the acoustic wave through the material is taken into consideration.[114]

8.1 Loss Mechanisms

Energy losses in a material arise from different mechanisms. A perfect material will have no loss since there will be no attenuation loss factor and no scattering due to imperfections or material inclusions. However, since perfect materials do not exist there will be attenuation of the elastic deformations as the waves propagate through materials, resulting in a decrease in amplitude as the waves progress. There will be specular reflection (and refraction) due to impedance mismatching at boundaries and also diffuse reflection due to scattering from rough interfaces at the boundary. For wave transmission through multiple boundaries there are lower transmitted intensities due to scattering at each interface compared with the incident wave intensity. This is shown in figure 8.1 where an initial signal I_0 passes through three boundaries, these are at the surface of the pSi, the pSi/cSi interface and the last boundary at the surface of the substrate. At each boundary a proportion of the initial signal is lost due to specular reflections $R_{1,2,3}$ and diffuse reflections (or scattering) $S_{1,2,3}$. As the signal propagates a distance d through the porous silicon region of the sample it undergoes an apparent attenuation β, and an apparent attenuation α through the cSi substrate of thickness D. $I_1^{(0)} = I_2^{(0)}$ is the first transmitted signal through the pSi sample on the substrate. The subsequent signals relate to multiple reflections within each of the layers. Different levels of scattering within the material matrix will occur depending on the grain or inclusion size of the material. This attenuation may also be dependent on the orientation of the inclusions. For a probe wavelength of similar size to the inclusions or imperfections within the material, there will be greater levels of scattering at these 'scatter centres' than if the wavelength was much greater than the size of the imperfections.

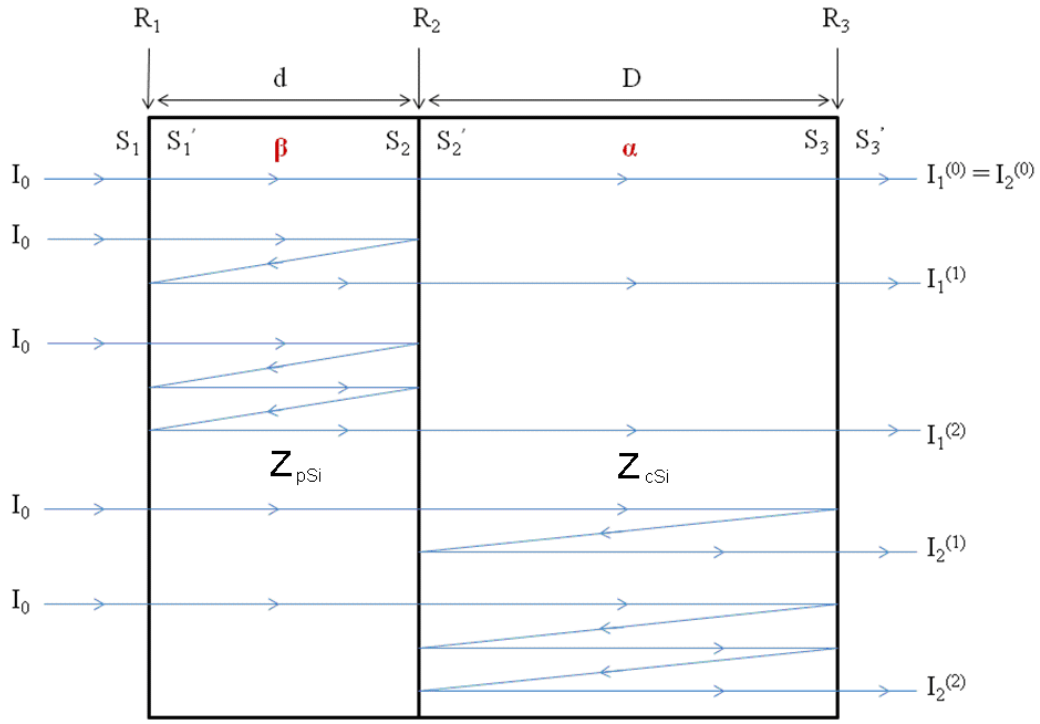

Figure 8.1 Multiple Reflections within each of the sample layers.

8.1.1 Attenuation

The term 'acoustic attenuation' used here is also referred to as 'acoustic absorption' or 'acoustic loss' and is the dissipation of acoustical energy in the transmitting medium (or at the boundaries of the medium) and its degradation into some form of heat energy.[115] The unit generally used to express acoustic energies and intensities is the decibel (dB) and acoustic attenuation loss is usually given as dB/m.

The propagation of ultrasound through a material is due to the elastic deformations of individual particles and is accompanied by energy losses within the material that are converted to thermal energy. These losses can be attributed to the thermal conductivity α_T of the material and due to internal friction which is usually referred to as viscous damping α_V.[116] The principal physical mechanisms contributing to this viscous damping are the thermo-elastic and Akhieser mechanisms. Thermo-elastic attenuation is due to irreversible heat conduction from compression regions to rarefraction regions in a longitudinal wave.[117] For Akheiser damping, in all materials

at a finite temperature there will be an equilibrium distribution of thermally excited acoustic waves known as phonons. As a coherently excited wave propagates through the material this phonon equilibrium is disturbed and the result is energy absorption (or damping) and this is known as Akhieser damping. Scattering at grain boundaries within the crystalline material can also occur although this is not always attributed to viscous damping because the attenuation due to this mechanism is not always proportional to the square of the frequency unlike Akheiser damping.

Insulators generally have the lowest levels of acoustic attenuation with semiconductors being the next type of material for lossiness. For both insulators and semiconductors the loss mechanism can be mainly attributed to the Akhieser mechanism. For metals the predominant damping mechanism depends upon the type of wave propagating through the material. This is because thermoelastic loss only occurs in longitudinal waves since shear wave propagation does not produce any change in the size of the volume elements. Thermoelastic effects therefore contribute to around a half of the longitudinal wave attenuation in metals with the rest being due to Akhieser effects. For shear waves the damping mechanism is mainly believed to be due to Akhieser damping.[117]

For example, the lowest attenuation factor measured at 1GHz has been for the insulator Yttrium aluminium garnet for the propagation of longitudinal waves along a cube-edge. This material has an attenuation factor of α=20-32dB/m.[117] For longitudinal waves propagating along a cube edge in the semiconductor pure silicon the attenuation factor is 1000dB/m.[117] Attenuation measurements taken by Kor, Mishra and Tripathi in 1973 for pure silicon in the [100] direction (cube edge) at T=298°K found the attenuation value to be 857dB/m. Attenuation values for longitudinal waves along a cube edge for metals such as copper are 27,000dB/m, and along a face-diagonal for gold α=20,000dB/m.

For ultrasonic wave propagation through the semiconducting cSi used in the following attenuation measurements, the main damping mechanism is most likely due to Akhieser damping.[118] A much smaller proportion of the attenuation could be attributed to thermoelastic losses within the longitudinal wave propagation through

the material matrix. The proportion of attenuation due to each mechanism seen in crystalline silicon will differ to that seen for pSi. PSi should have higher overall attenuation levels than crystalline silicon due to the large number of pores acting as scattering centres. PSi has a much larger surface to volume ratio than cSi and the increase in surface area will lead to more interfaces and boundaries which the propagating ultrasonic waves will encounter. Following the text of Auld[117], a description of loss is given below to aid the understanding of loss mechanisms in the pSi and cSi layers.

First, consider a lossless medium. Hooke's law in an ideal lossless medium for a spring is F=kx where *F* is the applied force, *k* is the spring constant and *x* is the spring displacement. Following this analogy, for an elastic wave propagating through an ideal material with strain ε_{ij} and stress σ_{ij} it was shown in section 4 that Hooke's law is given by $\sigma_i = c_{ij}\varepsilon_j$. Now considering loss in a system, the response of the spring in a damped system is represented with an additional damping term shown in the following differential equation (8.1).

$$F = kx + k'\frac{\partial x}{\partial t} \tag{8.1}$$

Similarly, an elastic wave propagating through a lossy medium is given by equation (8.2) where η_{ij} is the viscosity term; for a cubic system this is analogous to the elastic stiffness tensor.[119] The viscosity is the degree of resistance to deformation due to the applied stress and strain.

$$\sigma_i = c_{ij}\varepsilon_j + \eta_{ij}\frac{\partial \varepsilon_j}{\partial t} \tag{8.2}$$

Consider an x-propagating longitudinal wave in the [100] cubic direction. For lossless wave propagation the particle displacement $\underline{u}$ wave function is given by equation (8.3) and for a wave propagating in a lossy medium by equation (8.4).

$$\underline{u} = \underline{x}e^{i(\omega t - kx)} \tag{8.3}$$

$$\underline{u} = \underline{x}e^{-\alpha x}e^{i(\omega t - kx)} \tag{8.4}$$

The corresponding strain field is given by

$$\varepsilon_x = \frac{\partial u_x}{\partial x} = (-ik - \alpha)\underline{u} \tag{8.5}$$

and substitution into equation (8.2) for a material with cubic symmetry with wave propagation in the x-direction gives equation (8.6).

$$\sigma_x = c_{11}\varepsilon_x + \eta_{11}i\omega\varepsilon_x = -i(k - i\alpha)(c_{11} + i\omega\eta_{11})e^{i\omega t}e^{-i(k-i\alpha)x} \tag{8.6}$$

For the varying x-field for the wave propagating along the [100] direction the equation (8.7) of motion is

$$\frac{\partial \sigma_x}{\partial x} = \rho\frac{\partial^2 u_x}{\partial t^2} \tag{8.7}$$

giving

$$-i(k - i\alpha)\sigma_x = -\rho\omega^2 u_x \tag{8.8}$$

Then substituting for u_x and σ_x gives

$$(k^2 - \alpha^2 - 2i\alpha k)(c_{11} + i\omega\eta_{11}) = \rho\omega^2 \tag{8.9}$$

and separation of this into the real and imaginary parts leads to equations (8.10) and (8.11).

$$c_{11}(k^2 - \alpha^2) + 2\alpha k\omega\eta_{11} = \rho\omega^2 \tag{8.10}$$

$$i[(k^2 - \alpha^2)\omega\eta_{11} - 2\alpha k c_{11}] = 0 \tag{8.11}$$

Simultaneously solving equations (8.10) and (8.11) by subtracting one from the other for (k^2-α^2) and 2αk gives

$$k^2 - \alpha^2 = \frac{\rho}{c_{11}} \frac{\omega^2}{\left(1 + \left[\frac{\omega \eta_{11}}{c_{11}}\right]^2\right)} \tag{8.12}$$

And

$$2\alpha k = \frac{\rho}{c_{11}} \frac{\omega^3 \eta_{11} / c_{11}}{\left(1 + \left[\frac{\omega \eta_{11}}{c_{11}}\right]^2\right)} \tag{8.13}$$

Eliminating *k* from these two relations above leads to the following equation (8.14).

$$\alpha^2 = \frac{\rho \omega^2}{2c_{11}} \left(\frac{1}{\left(1 + \left[\frac{\omega \eta_{11}}{c_{11}}\right]^2\right)^{1/2}} - \frac{1}{\left(1 + \left[\frac{\omega \eta_{11}}{c_{11}}\right]^2\right)} \right) \tag{8.14}$$

For most solids the viscosity coefficient is sufficiently small that $\left(\frac{\omega \eta_{11}}{c_{11}}\right)^2 << 1$ even for frequencies as high as 1 GHz so the expression in equation (8.14) reduces to the following much simpler equation before giving equation (8.16).

$$\alpha^2 = \frac{\omega^4}{4} \frac{\rho}{c_{11}} \left(\frac{\eta_{11}}{c_{11}}\right)^2 \tag{8.15}$$

Giving

$$\alpha = \frac{\omega^2}{2} \left(\frac{\rho}{c_{11}}\right)^{1/2} \left(\frac{\eta_{11}}{c_{11}}\right) \tag{8.16}$$

Therefore, the attenuation factor is proportional to the square of the frequency.[117] For pSi, the attenuation is unknown, however it is reasonable to assume that there will be a dependence of the attenuation on morphology because the velocity has been found to have a strong dependence on pore morphology. Figure 5.13 shown earlier in chapter 5 shows a reduction in the power of the transmitted signal towards higher frequencies. The transmitted signal was normalised to the response of the transducers shown in figure 5.12. At a frequency of 1 GHz the difference between the transmitted power with and without the sample in place between the transducers is 13dB, at 2 GHz the difference in power is 21dB and at 2.7 GHz is 25dB. This loss in transmitted power through the sample is not proportional to the square of the frequency; this reduction in power could be due to coupling losses or scattering at interfaces.

8.1.2 Scattering at Boundaries

The temperature at which the porous silicon layers are etched in HF will influence the roughness of each interface within the layers.[120, 121] Scattering of the acoustic waves at each boundary will cause acoustic losses due to diffuse reflections.[122] The incident wavelength upon the boundary is important with respect to the interface roughness as it can strongly influence the amount of scattering observed. For example, an incident wave of similar wavelength to material features such as pore size or other scattering feature will cause more scattering than a large wavelength incident upon a much smaller feature which will hardly scatter at all. Ultrasonic techniques are therefore very useful in determining the quality of thin films and layers as the use of high levels of frequency enable small features on the micro-scale to be studied.[123]

The current density and etch time influences the porosity and thickness of the porous silicon layers fabricated. It has previously been shown that the thicknesses of single porous silicon layers are directly related to the interface roughness at the porous silicon and crystalline silicon boundary.[120] Generally, the greater the thickness of the etched layer then the greater the interface roughness of the layer. The interface roughness between layers can be measured by profilometry, AFM or studying Fresnel coefficients using optical reflection measurements.[124, 125] The method of choice used

for measuring the interface roughness of single layered samples fabricated with layers of varying thickness presented here is by AFM. This is one of the easiest ways to obtain the surface morphology using real space imaging. It is important to know the interface roughness and scattering effects when it comes to multilayered structures such as distributed Bragg Reflectors. During the fabrication of these multilayers there is a periodic alternation between two current densities and the interfaces possess different roughnesses at each current change. If the interface roughness is some function of the layer thickness then there will be a limit to how thick these multilayers can be fabricated before scattering effects influence the quality and performance of such devices. It has been shown that device fabrication using lower current densities produces layers with rougher interfaces than those etched with higher current densities.[120] As discussed in chapter 5, the roughness of the backside of the Si wafer was found to be 713nm which is close to the wavelengths of acoustic waves at 1GHz propagating through the cSi substrate region. The backside of the Si wafer will therefore give the largest contribution to scattering at the boundary due to scattering theory.[126]

8.1.3 Measured Loss in Single-Layered Porous Silicon

Attenuation measurements on p-type Si with respect to doping level has previously been investigated by other groups[127, 128] but no attenuation measurements for p++ pSi has been found in the literature. The acoustic loss in p++ pSi samples has been measured along the [100] direction for samples of varying porosities using acoustic transmission measurements with the experimental set-up that was described in figure 5.6. Some of the samples used for the loss measurements presented in this section are the same as the samples introduced in table 5.1 which include B1, B2, B3, B8, B6 and B4, in addition to the samples shown in table 8.1.

Sample	Porosity	d of pSi layer (μm)
B3b	0.65	76
B9	0.54	78

Table 8.1 Additional samples used for the loss measurements.

Ultrasonic measurements at 1 GHz were used to study the round trip reflections within the pSi layer, attached to the Si wafer, using a Fourier transform of reflected peaks within the sample. The amplitude reduction seen in the initial peak (from one round trip reflection) from the porous layer compared to subsequent peaks (for an increasing number of round trips in the porous layer), has been used to obtain an acoustic loss value as follows.

The Fourier transform of the frequency data set measured for each pSi sample (see chapter 5) was used to find the attenuation through the pSi layer, where a series of peaks were seen. The thickness of each pSi layer is known from SEM measurements. In order to find the attenuation of acoustic longitudinal waves through the pSi layer and cSi substrate regions, it was necessary to determine the origin and amplitude of transmitted peaks through the samples. Each of the peaks seen on the Fourier transform correspond to reflections in each region of the samples. An example of the Fourier transform of the transmitted signal through a single pSi layer was shown previously in figure 5.9 of chapter 5. The first peak of the spectrum corresponds to the first arrival of the transmitted acoustic wave through the entire sample. The second peak usually corresponds to one reflection in the pSi layer followed by subsequent peaks from increasing number of reflections within the pSi layer. The peak corresponding to one round trip reflection in the cSi substrate layer is at later times in the spectrum compared to the pSi reflections due to the cSi substrate region being much thicker than that of the pSi layer. Round trip reflections from the pillar transducers can also be seen in the spectrum. Figure 8.2 below shows the round trip reflections from one of the pSi samples with porosity of 0.49 and thickness of 72μm, shown on a logarithmic scale. The magnitude of the peaks have been normalised with the first peak arrival seen at 200 ns being normalised to 10.

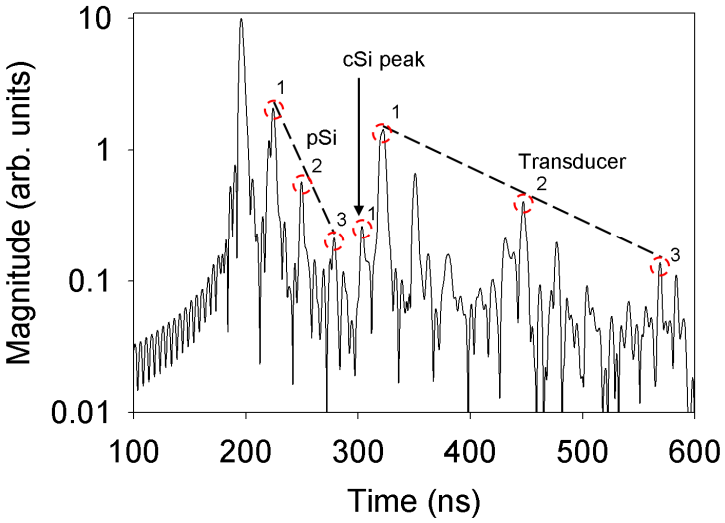

Figure 8.2 Fourier transform peak amplitudes from a single-layered pSi sample with peaks corresponding to sets of reflections within the pSi layer and cSi substrate region.

The loss in the amplitude of the signal due to multiple reflections within the sample is due to loss at each boundary which is due to an impedance mismatch given by equations (3.17) and (3.18). A proportion of the reflected signal at each interface will be specular and a proportion will be diffuse. The diffuse reflections are 'lost' from the transmitted signal due to scattering, however, the specular reflections within the layers will contribute towards the amplitude of the transmitted signal. The values of acoustic loss found using consecutive peaks includes all origins of loss i.e. an attempt to separate the scattering loss due to impedance mismatching from the attenuation loss through the porous region has not been done.

The ratio of the amplitude of a wave propagating along the [100] direction in a lossy medium is the attenuation from x_1 to x_2 (where $x_2 > x_1$). The attenuation coefficient β_{dB} has the units of decibels per unit distance (dB/μm) and can be found using either intensities or amplitudes of the peaks, as shown in equation (8.17) and (8.18) respectively, where x is the attenuation distance between consecutive peaks.

$$\beta_{dB} x = 4.343 \ln\left(\frac{I_1}{I_2}\right) \tag{8.17}$$

which is equivalent to

$$\beta_{dB} x = 8.686 \ln\left(\frac{A_1}{A_2}\right) \tag{8.18}$$

For each of the porous samples measured, the attenuation coefficient β_{dB} was found looking at the intensity reduction between consecutive peaks using equation (8.17). An average was taken for the attenuation found between peaks 1 to 2, and for peaks 2 to 3. The results have been plotted as a function of sample porosity shown below in figure 8.3. There is no clear dependence of the attenuation coefficient on porosity. This could be due to the fact that reflection losses at the boundaries have not been considered in the calculation of the attenuation coefficient.

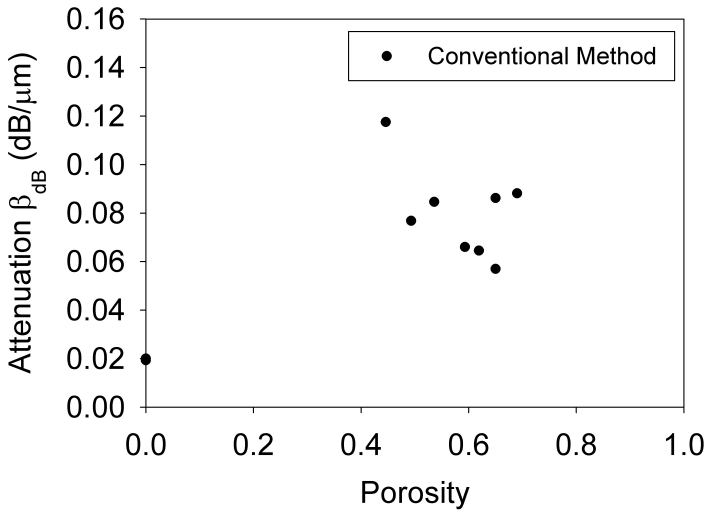

Figure 8.3 Attenuation as a function of porosity for p++ pSi for measurements in the [100] crystallographic direction at a frequency of 1GHz.

In addition to the porous samples measured, two Si wafers >300 μm thick that were SSP were also measured and the peak reflections studied to obtain an attenuation value of 0.02 dB/μm for each wafer. Note that these attenuation measurement are for p++ Si for longitudinal waves propagating in the [100] direction along a cube edge. The measured attenuations for these p++ Si wafers are higher than the attenuation measurement taken by Kor, Mishra and Tripathi (1973) for longitudinal waves propagating in the [100] direction for pure Si which was 0.000857 dB/μm. This

suggests that the doping level of the Si affects the attenuation of longitudinal waves in this crystallographic direction. In general, the losses found in the porous layers were higher than the losses found for the Si wafers.

Since there was no dependence of attenuation coefficient on porosity, a 'series method' to separate the loss due to reflection and the loss due to attenuation has been considered and is described as follows. The losses in the porous layer of each sample used in this investigation have been found using a 'series method' approach which is described as follows. This approach has been used to attempt to separate loss due to reflections at boundaries from the attenuation through a region of material. This is because the reflectance at each boundary will depend on sample porosity and could skew the attenuation measurement found through the porous region.

If the loss due to multiple reflections within the porous layer is considered, there will be a contribution to the reduction in amplitude between consecutive peaks due to an attenuation term and an impedance mismatch term. For an initial signal of I_0 such as for the peak shown in figure 8.2 at 200 ns, the loss will be as shown in equation (8.19) where β is the actual attenuation loss through the pSi layer (with units per μm) and α is the loss in the cSi layer. The loss due to one round trip reflection within the porous layer is shown in equation (8.20) and for two round tip reflections by equation (8.21). Note that the symbols used for labelling follows that used in figure 8.1.

$$I_1^{(0)} = I_0 e^{-2\beta d} e^{-2\alpha d} \tag{8.19}$$

$$I_1^{(1)} = I_1^{(0)} R_1 R_2 e^{-4\beta d} \tag{8.20}$$

$$I_1^{(2)} = I_1^{(0)} R_1^2 R_2^2 e^{-8\beta d} \tag{8.21}$$

Considering this series of loss, the *n*th term for the *n*th round trip reflection in the porous layer will be given by,

$$I_1^{(n)} = I_1^{(1)n} \Big/ I_1^{(0)[n-1]} \tag{8.22}$$

which is equivalent to,

$$I_1^{(n)} = I_1^{(0)} [e^{-4\beta d} R_1 R_2]^n \tag{8.23}$$

By similar analogy, the loss in the cSi substrate layer for the *n*th round trip reflection is found to be,

$$I_2^{(n)} = I_2^{(0)}[e^{-4\alpha D} R_2 R_3]^n \qquad (8.23)$$

If the reflection peaks in the porous layer are plotted on a logarithmic scale of intensity against the number of round trips, ln(I) against n, as shown in figure 8.4, then the gradient *m* is $\ln[e^{-4\beta d}R_1R_2]$ as shown in the following equation (8.24).

$$m = \ln(R_1 R_2) - 4\beta d \qquad (8.24)$$

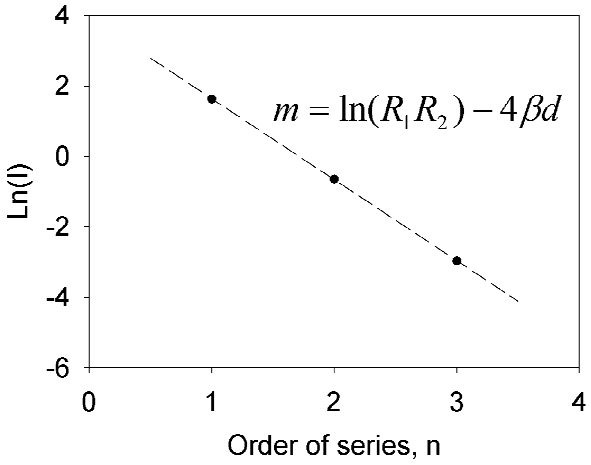

Figure 8.4 Reflection peaks in the porous layer on a logarithmic intensity scale against round trips.

This gradient *m* can be related to a reflection loss term $ln(R_1R_2)$ and also an attenuation term $4\beta d$. For each sample this method has been used to find the fraction of the signal transmitted through each sample by looking at the magnitude (or intensity) of the consecutive reflection peaks. Note that for two of the samples which were around 20 μm thick it was difficult to distinguish between separate peaks in the Fourier transform so that the fraction of acoustic waves transmitted could not be obtained.

The reduction in transmitted signal due to the reflections at the boundaries was taken into account simply by rearranging equation (8.24) to give equation (8.25). The values

of reflections at the R_1 and R_2 interfaces were found based on the known sample porosity using equation (3.17) discussed earlier in chapter 3 combined with equation (3.27). Substituting the R_1 and R_2 reflectance values with the gradient m found as shown in figure 8.4, the attenuation coefficient β through one micron of porous material has been found for each of the samples. The sample thicknesses were measured using the SEM and the results are plotted against sample porosity shown in figure 8.5.

$$\beta = \frac{\ln(R_1 R_2) - m}{4d} \tag{8.25}$$

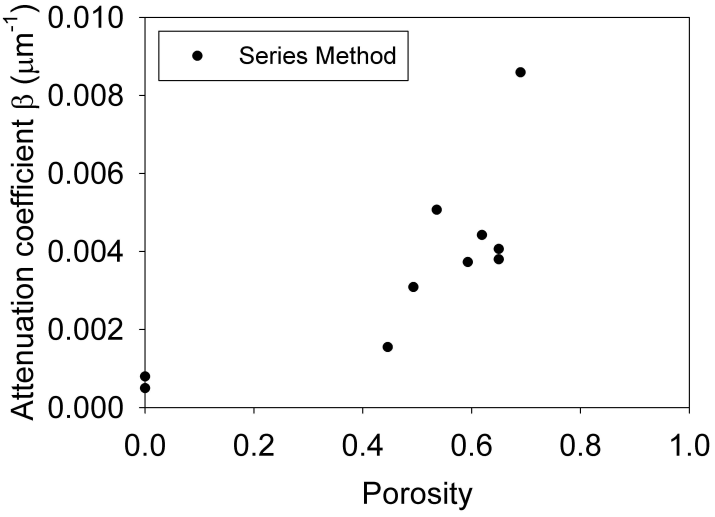

Figure 8.5 Attenuation coefficient for longitudinal acoustic waves through one micron of porous material as a function of porosity, for p++ pSi with measurements in the [100] crystallographic direction.

There is a weak relationship between attenuation coefficient and sample porosity. The samples with lowest porosity have the smallest attenuation coefficients. Given the small size of the data set, more measurements would need to be taken to establish a definite relationship between the attenuation coefficient and sample porosity. These attenuation values are given after the reflection losses have been taken into account. The weak dependence on porosity after considering the reflection losses suggests that the reflection losses are larger than the attenuation loss in the porous layer.

These attenuation measurements for p++ porous layers are lower than those given in one recent study of the attenuation loss in nano-crystalline Si using picosecond ultrasonics, the loss was found to be (2600 ± 660 cm^{-1}).[129] This may simply be because for the porous layer measurements shown in figure 8.5, the reflection losses have been considered.

The attenuation coefficient β_{dB} for the porous material was seen to generally be higher than that for the cSi wafers. However, no strong trend of the attenuation on sample porosity was observed which led to consideration of the reflection losses within the sample. For the attenuation β found, there was a slight increase in apparent attenuation with porosity. This could be due to the larger surface to volume ratio of the pSi due to the presence of the pores give the propagating ultrasonic waves more scattering centres to encounter. However, measurements on a larger data set would give a much clearer relationship of the attenuation dependence on porosity.

8.2 Elastic Properties of Porous Silicon

Ultrasonic measurements performed in the [100] crystallographic direction of boron doped p++ pSi found the relationship between longitudinal velocity V_L and porosity p to be empirically described by equation (8.26). For the mesoporous Si samples used in this investigation, the value of the exponent $k = 0.6$, the value of which depends on morphology due to doping level of the Si wafer used. For comparison, ultrasonic measurements performed by other groups for pSi with a slightly lower doping level (p+) than those used in this investigation found that $k = 1.095$.[130]

$$V_L = V_0(1-p)^k \tag{8.26}$$

The relationship between the longitudinal wave velocity in the [100] crystallographic direction and the elastic stiffness constant c_{11} is given for bulk cSi by equation (8.27) for a material with density ρ.

$$V_L = \sqrt{\frac{c_{11}}{\rho}} \tag{8.27}$$

By substitution and rearrangement of the terms, the porosity dependence of the elastic constant c_{11} for the p++ samples can be found based upon longitudinal velocity

measurements through the different pSi samples with varying porosities and is shown by equation (8.29). The value for the elastic constant c_{11} for pure cSi is 166 GPa.[131]

$$c_{11}^{pSi} = c_{11}(1-p)^{2k+1} \tag{8.28}$$

$$c_{11}^{[p++]pSi} = c_{11}(1-p)^{2.2} \text{ GPa} \tag{8.29}$$

The elastic constant c_{11} for the p++ samples that have been measured are shown in figure 8.6. For comparison, the elastic constant found for wafers with slightly lower doping levels for p+ samples is also shown. This elastic constant is for measurements in the [100] direction. Using the ultrasonic measurement technique described earlier in section 5.4, it is only possible to measure this c_{11} constant on the [100] wafers. In order to find the dependence of the other constants on porosity, such as for the c_{12} and c_{44} elastic constants, porous layers etched onto [110] and [111] Si wafers would be needed and this was beyond the scope of this particular investigation. However, it is possible to compare the c_{11} measurements made on the p++ samples with existing data for p-doped pSi although doping level will vary. The elastic constant for the pSi layers was found to be smaller than that for bulk Si and have a strong dependence on porosity.

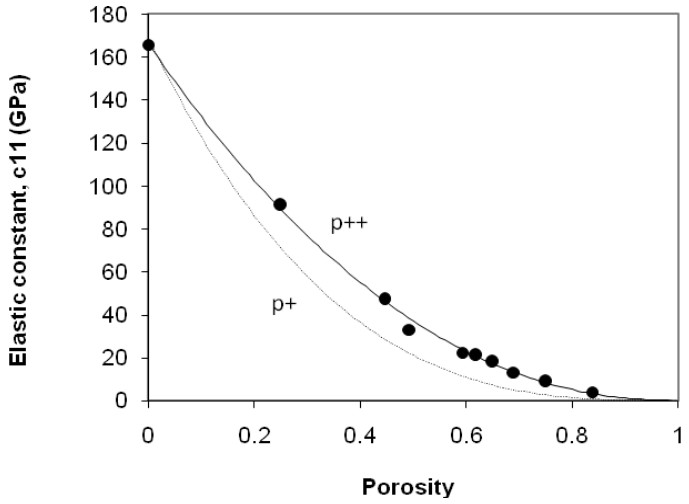

Figure 8.6 Comparison between the c_{11} elastic constant found empirically for p+ (dashed line), and p++ (solid line) pSi based upon longitudinal velocity measurements (circles).[132]

The directional dependence of the elastic properties of a cubic crystal system were discussed earlier in section 2.1. In particular, the Young's modulus of Si in different crystallographic directions was described, now the Young's modulus of pSi will be discussed. In order to describe the directional dependence of the Young's modulus of pSi on porosity, the c_{11}, c_{12} and c_{44} elastic constant must be known. Since only the c_{11} constant has been measured for the p++ samples, existing data for p+ pSi has been used to model the Young's modulus of pSi.

Assuming that the pSi layers retain the cubic symmetry of the parent wafer, it is then possible to investigate the directional dependence of Young's modulus as a function of porosity using the following equations. Previous results from the literature[132] for p+ pSi yielded the following dependence of the stiffness constants c_{11}^{pSi}, c_{12}^{pSi} and c_{44}^{pSi} on porosity $0 < p < 1$.

$$c_{11}^{pSi} = 168.5(1-p)^3 \text{ Gpa} \quad (8.30)$$

$$c_{12}^{pSi} = 62.6(1-p)^{6.23} \text{ GPa} \quad (8.31)$$

$$c_{44}^{pSi} = 79.0(1-p)^{2.3} \text{ GPa} \quad (8.32)$$

It is worth noting that the elastic constant values for pure cSi are
$c_{11} = 166$ GPa $c_{12} = 64$ GPa and $c_{44} = 79$ GPa[133]
which are close to the values found[132] for the case of zero porosity, $p = 0$.

Assuming that a similar representation of the dependence of the stiffness constants upon porosity can be used to describe cubic p++ pSi, the elastic constants need only to be multiplied by a 'porosity factor' f in order to account for the porosity dependence as follows. The porosity dependence may not affect all three of the elastic constants equally so let the porosity factor for the c_{11} constant be f_{11}, and similarly for the other two constants (f_{12} for the c_{12} constant, and f_{44} for the c_{44} constant) where $c_{ij}^{pSi} = c_{ij} f_{ij}$ and the porosity factor has the form, $f_{ij} = (1-p)^x$. It has been found that the exponent value, x for the c_{11} constant for p++ pSi differs from that found for p+ pSi showing that the doping level of the Si wafer influences its value. The extent to which other factors may influence the exponent value is unclear, for example, it may differ between samples depending on the method of fabrication.

Substituting the dependence of the p+ elastic stiffness constants given by equations (8.30 – 8.32) into equations (2.9 – 2.11) the porosity dependence of the stiffness constants can be used to describe the porosity dependence of the compliance constants s_{ij}. Substitution of these into equation (2.8), the porosity dependence of Young's modulus in each direction E_{ijk} can be modelled. From the resulting relations given by equations (8.33 – 8.35) it can be seen that E_{100} does not depend upon the c_{44} constant but in the [110] and [111] crystallographic directions the Young's modulus E does depend upon the c_{44} elastic stiffness constant.

$$E_{100}^{pSi} = \left[\frac{c_{11}f_{11} + c_{12}f_{12}}{(c_{11}f_{11} - c_{12}f_{12})(c_{11}f_{11} + 2c_{12}f_{12})} \right]^{-1} \tag{8.33}$$

$$E_{110}^{pSi} = \left[\frac{c_{11}f_{11}}{2(c_{11}f_{11} - c_{12}f_{12})(c_{11}f_{11} + 2c_{12}f_{12})} + \frac{1}{4c_{44}f_{44}} \right]^{-1} \tag{8.34}$$

$$E_{111}^{pSi} = \left[\frac{c_{11}f_{11} + 3c_{12}f_{12}}{3(c_{11}f_{11} - c_{12}f_{12})(c_{11}f_{11} + 2c_{12}f_{12})} + \frac{1}{3c_{44}f_{44}} \right]^{-1} \tag{8.35}$$

The directional dependence of Young's modulus on porosity has been modelled using SigmaPlot 10.0 where the parameters are as follows.

$f_{11}=(1\text{-}p)^3$ $\quad f_{12}=(1\text{-}p)^{6.23}$ and $\quad f_{44}=(1\text{-}p)^{2.3}$

$c_{11} = 168.5GPa$ $\quad c_{12} = 62.6GPa$ and $\quad c_{44} = 79.0GPa$

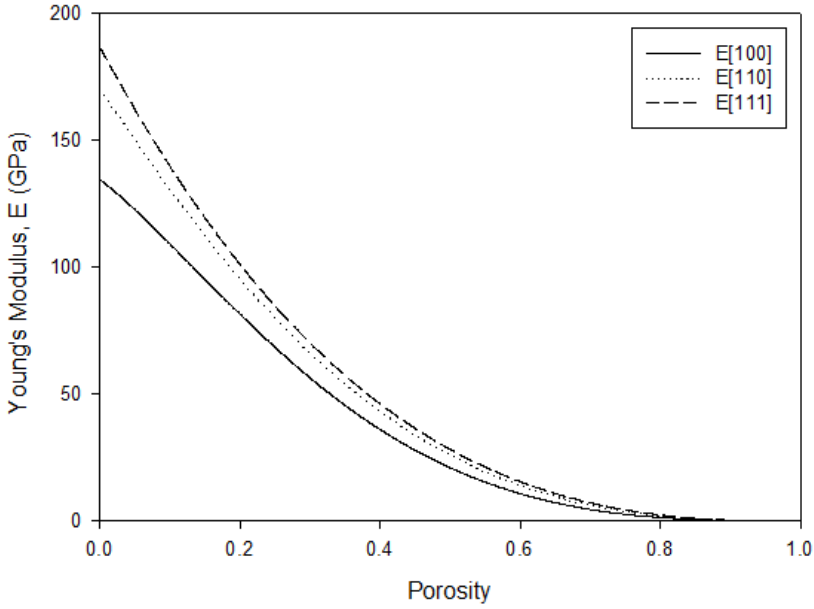

Figure 8.7 Porosity and directional dependence of Young's Modulus E_{ijk} for p+ pSi.

The directional and porosity dependence of Young's modulus for p+ pSi with cubic crystal symmetry is shown in figure 8.7 and the dependence of E on porosity is stronger for lower porosities than it is for those above 60%. In all crystallographic directions the Young's modulus decreases as a function of porosity. Other groups have measured the Young's modulus of p-type pSi by nano-indentation[134] and a similar dependence of the Young's modulus upon porosity for p+ pSi has also been found.

8.2.1 Influence of Pore Geometry on the Young's Modulus of Porous Silicon

The geometry of the pores within a porous material has been shown to influence the material's effective elastic properties.[135] The response of the physical properties of a porous material are based upon the type of porosity i.e. the morphology of the pores. The Young's modulus was modelled for materials containing four different types of pore geometries, these being for cylindrical, cubic, spherical and cross-shaped pores. A 'generalised method of cells' (GMC) has been used to model the effect that pore morphology has on the Young's modulus. The GMC considers a material that possesses a periodic structure such that a repeating, representative volume element can be identified in the form of a unit cell. Each unit cell is then comprised of many

sub-cells that can contain a known material so that a pore shape can be defined and the effective elastic properties of the unit cell can be modelled. There is a limiting value of porosity that can be modelled for each pore shape that arises as the outer edge of the pore is extended to the sides of the unit cell where the model breaks down.

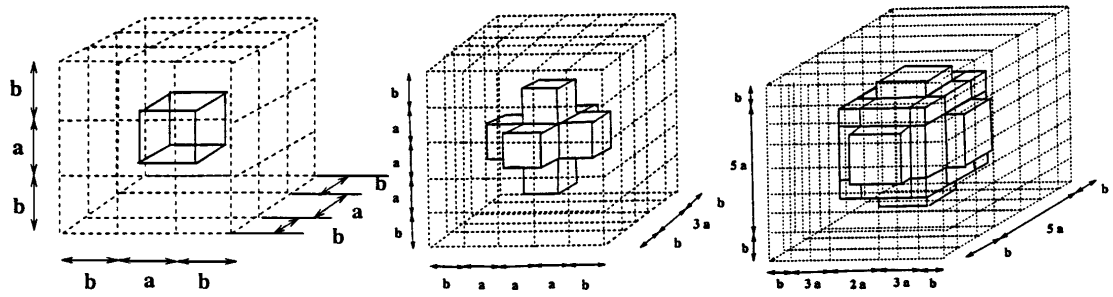

Figure 8.8 (Left) Cubic pore, (middle) cross-shaped pore and (right) spherical pore.[135]

A minimum solid area (MSA) model was applied to the GMC representation for three different well-defined pore shapes because the effective properties of porous media have previously been associated with pore shape and packing arrangements and these are related to the minimum area that transfers load. Application of this model to a Si material for the unit cell containing spherical, cubic and cross-shaped pores yielded the following result for the porosity dependence of Young's modulus on pore geometry (figure 8.9). The Young's modulus is highest for cube-shaped pores and lowest for cross-shaped pores. The model breaks down for the cross shaped pores just above a porosity of 60% because the unit cells begin to merge into one another as the pore volume is increased. For spherical pores the model breaks down at 80% porosity.

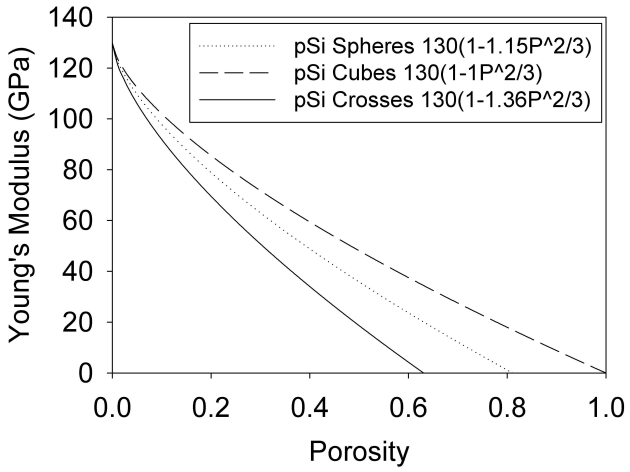

Figure 8.9 Effect of pore geometry on Young's modulus for pSi using $E_{cSi[100]}$ = 130GPa.

Effective medium models demonstrate the importance of cell morphology in determining the behaviour of acoustic waves in a porous material.[136] However, pSi is generally difficult to model due to the variety of pore size and shape that can be achieved which depend upon many parameters such as doping level and fabrication conditions. Other groups have studied the affect of aspect ratio of pores on effective elastic moduli within a porous material such as for foamed aluminium[137] and the fabrication technique and resulting morphology of pSi structures has also been investigated.[138] The range of models available make it possible to predict the elastic constants of a material such as pSi using a set of assumptions and initial conditions and understanding of the elastic properties gives insight into the behaviour of this material when it is used as a multilayer for acoustic applications.

This chapter has discussed the loss mechanisms for acoustic waves travelling through a material. The acoustic loss through pSi layers has been studied and it was found that the loss through the porous regions were higher than the loss found for the cSi region. Reflection losses were taken into consideration to find a dependence of loss on porosity. The elastic properties of pSi material assuming cubic symmetry has been studied by using the Young's elastic modulus for different crystallographic directions. The Young's modulus was found to decrease with increasing porosity values. The c_{11} elastic constant for p++ pSi has been given and the effect of pore geometry on the Young's elastic modulus was also considered.

Conclusions

PSi multilayers have been electro-chemically etched from heavily doped p++ Si wafers to fabricate mesoporous Si Bragg mirrors, rugate filters and microcavities for acoustic applications. The electro-chemical etching technique used a hydrofluoric acid and ethanol mix, that acted as the electrolyte during fabrication, with the doped Si wafers acting as the electrodes. The LabView controlled current density enabled the Si wafers to be etched top-down to produce pSi films on the bulk Si substrates. The porosity of the pSi layers produced was controllable with the current-time etching profile during the fabrication process. The Si wafers were etched to produce multilayers with square-wave and sinusoidal porosity profiles through the mirrors and filters. The pSi multilayers were etched along the [100] crystallographic direction.

Using single pSi layers, the acoustic impedance of the pSi material was determine and the dependence on porosity found. Control of the porosity profile throughout the multilayers directly allowed for control over the acoustic impedance profile of the pSi multilayers which were characterised by SEM and AFM imaging in addition to the optical and acoustic experimental measurements. Using a cross-sectional SEM image through the stack of pSi layers, the layer thicknesses were deduced and AFM imaging found the rms surface roughness of the back surface of the Si wafer to be ~ 0.7 μm which gave an idea of the interface quality.

The layer porosities were measured using optical interferometry and the optical response from the pSi layers gave an effective refractive index of the porous layers. The Bruggeman EMA was used to determine the layer porosities based on the effective refractive index measured. Simulation programs written on the MatLab platform were used to run simulations of longitudinal acoustic waves through the pSi multilayers using the TMM. It was found that the simulated response of multilayered pSi gave stopbands that were in good agreement with experimental observations.

Acoustic transmission measurements were performed using a pair of ultrasonic transducers where transmission measurements on single layered pSi determined the

acoustic longitudinal wave velocity dependence upon porosity. This velocity dependence on porosity was used to design the BAW multilayers, examples include pSi Bragg mirrors, rugate filters and microcavities.

All-silicon mirrors with specific desired frequency responses have been fabricated in this investigation. Fabry-Perot filters, that exhibit a transmission peak within a stop-band, were created for use in the frequency range of interest at 1 GHz. The pSi Bragg mirrors fabricated showed stopbands with 50 dB rejection at 1 GHz with fractional bandwidths up to 40 %. Microcavities based on pSi for fundamental stopbands at 1 GHz were shown to have Q-factors near 165.

The ability to easily control the porosity and therefore the acoustic impedance profile of the structures using the electrochemical fabrication technique, made it possible to create smoothly varying porosity profiles such as those used for rugate filters. These single frequency filters showed that a single transmission band without higher order harmonics can be obtained. As expected from their optical analogues, the acoustic rugate filters showed suppression of the higher order stopbands and had bandwidths 67 % of the Bragg mirrors designed with the same porosities and layer thicknesses. The pSi rugate filters fabricated in this research are the first pSi-based rugate filters studied for acoustic applications. Multilayers with apodisation functions were also fabricated to modify the filter frequency response and this further highlights control over the filter design using the pSi material.

This research should make it possible to create other acoustic devices with smoothly varying acoustic impedance profiles, such as those needed for anti-reflection coatings used in transducers, index-matching layers or filters that have apodization functions, and a superposition of filters suitable for a wide range of frequencies. The acoustic loss through single layered pSi was also studied in this investigation and it was found that the loss in pSi is larger than that measured for bulk Si. This work could be extended to determine the suitable of pSi based multilayers for acoustic applications at frequencies above 20 GHz where careful consideration of the acoustic loss at higher frequencies could be made.

Acknowledgements

Firstly, I would like to acknowledge the ongoing support that I have received from my supervisor Dr. Paul A. Snow. He has guided me throughout the course of this research and I truly would not have managed to complete this work without his invaluable support.

Thank you to Wendy Lambson for friendly technical assistance in the fabrication lab who always had time to spare if I needed a piece of equipment or more etching acid. Thank you to Prof. Dmitry Kovalev for the use of the optics lab and equipment and thanks go to my 'etching buddy' Dr. Bernhard Goller for our porous silicon discussions. Thank you to the staff in the Centre for Electron Optic Studies for the use of the scanning electron and the atomic force microscopes.

I would also like to thank the people in the Physics Department at the University of Bath, all of whom are friendly and give a pleasant working environment. I have thoroughly enjoyed researching this doctorate so thank you to everyone who has helped or supported me. Thank you to my close friends for always being there for me. Special thanks go to Alex McMillan, my best friend who keeps my feet firmly on the ground and has always been there for me whether for work or personal reasons.

Finally, I would like to thank my family for always being there for me, especially my Nan, without her unconditional support I know that I would not be where I am today.

This work was funded by EPSRC, Project No. EP/C010469/1.

Appendix

BM- Bragg Mirror, MC- Microcavity, RF- Rugate Filter

Sample #	Fabrication Date	Type of Multilayer	I_1 (mA)	I_2 (mA)	t_1 (s)	t_2 (s)	N	p_1	p_2	d_1 (μm)	d_2 (μm)
1	05/02/2008	BM	-	-	-	-	20	0.62	0.68	1.5	1.3
2	23/03/2009	BM	510	600	9.1	8.0	30	0.58	0.64	1.0	1.0
3	23/03/2009	BM	510	600	9.1	8.0	30	0.56	0.61	1.0	1.0
6	25/03/2009	MC	750	850	7.4	6.9	21/1/20	0.68	0.72	1.0	1.0
8	24/03/2009	BM	800	900	7.1	6.7	8	0.70	0.73	1.0	1.0
9	23/03/2009	BM	460	330	1.4	1.9	30	0.66	0.62	0.2	0.2
14	13/07/2009	MC	510	600	10.9	9.6	20/1/20	0.58	0.64	1.3	0.8
23	29/07/2009	RF	600	510	-	-	15	-	-	1.1	1.1
24	16/09/2009	BM	510	600	10.9	9.6	20	0.59	0.63	1.1	1.1
26	16/09/2009	RF	510	600	-	-	20	0.63	0.69	1.0	1.0
27	17/09/2009	RF	510	600	-	-	20	0.61	0.67	1.1	1.1
37	22/01/2010	BM	493	690	14.3	12.6	15	0.43	0.57	1.6	1.7
38	22/01/2010	RF	493	690	-	-	15	0.43	0.57	2.0	2.1
39	24/02/2010	MC	400	575	14.0	13.9	15/1/15	0.53	0.68	1.3	1.4
41	01/03/2010	MC	400	575	14.0	13.9	15/1/15	0.53	0.64	1.2	1.4
42	24/02/2010	BM	470	690	15.5	15.6	15	0.59	0.73	1.6	1.8
43	24/02/2010	RF	470	690	-	-	15	0.58	0.72	1.6	2.1

Sample #	Fabrication Date	Type of Multilayer	I_1 (mA)	I_2 (mA)	t_1 (s)	t_2 (s)	N	p_1	p_2	d_1 (μm)	d_2 (μm)
44	24/02/2010	BM	534	700	10.4	11.0	5	0.63	0.70	1.2	1.3
45	24/02/2010	BM	534	700	10.4	11.0	10	0.62	0.70	1.3	1.2
46	24/02/2010	BM	534	700	10.4	11.0	15	0.63	0.71	1.3	1.2
47	24/03/2010	BM	500	600	16.4	12.0	15	0.61	0.71	2.2	1.1
50	28/04/2010	BM	484	684	22.9	17.0	15	0.61	0.72	2.1	1.7
51	28/04/2010	BM	484	684	22.9	17.0	15	0.65	0.74	2.1	1.7
52	28/04/2010	RF	484	684	-	-	30	0.61	0.73	1.2	1.2
59	20/05/2010	BM	350	510	0.9	1.2	20	0.58	0.64	0.1	0.1
72	26/08/2010	MC	434	650	11.5	7.7	10/1/10	0.63	0.71	1.0	0.8
75	26/08/2010	MC	510	600	10.9	9.6	15/1/15	-	-	-	-
81	11/10/2010	BM	534	700	10.4	11.0	-	-	-	-	-
83	11/10/2010	MC	434	650	11.5	7.7	10/1/10	-	-	-	-

References

[1] V. Lehmann, Electrochemistry of Silicon: Instrumentation, Science, Materials and Applications (Wiley-VCH, Weinheim, Germany, 2002).
[2] L. T Canham, Appl. Phys. Lett, **57** (10) 1046 (1990)
[3] Properties of Porous Silicon, Edited by Canham, Leigh © 1997 Institution of Engineering and Technology
[4] R.J.M. Fonseca, J.M. Saurel, A. Foucaran, J. Camassel, E. Massone, and T. Taliercio, "Acoustic investigation of porous silicon layers," *J. Mat. Sci.* **30**, 35-39 (1995)
[5] G.T. Andrews, Elastic and structural properties of supported porous silicon layers, Ph.D thesis, Memorial University of Newfoundland (1999)
[6] A. Reinhardt and P.A Snow, "Theoretical study of acoustic band-gap structures made of porous silicon", *phys. Stat. sol. (a)*. **204**, 1528-1535 (2007)
[7] 'Elastic Properties of Porous Silicon Superlattices' PhD Thesis, Anna Maria Polomska, Memorial University of Newfoundland (2009)
[8] William M. Merrill, Rodolfo E. Diaz, Michael M. LoRe, Mark C. Squires and Nicolaos G. Alexopoulos, IEEE Transactions on antennas and propagation 47 No. 1, (1999)
[9] Thin Film Bulk Acoustic Wave Resonator and Filter Technology, K.M. Lakin, K.T. McCarron, J. Belsick, and J.F. McDonald, TFR Technologies Inc (2001)
[10] Thin Film Bulk Acoustic Wave Resonators (FBAR) for Wireless Applications, R. C. Ruby, P. Bradley, Y. Oshmyansky, A. Chien, J. Larson III, Agilent Technologies, published in AnalogZONE
[11] Solidly mounted thin film electro-acoustic resonator utilizing a conductive Bragg reflector, Johannes Enlund, David Martin, Ventsislav Yantchev, Ilia Katardjiev, Sensors and Actuators A 141 (2008) 598–602
[12] Fabrication and frequency response of solidly mounted resonators with 1/4λ mode configuration, Chung-Jen Chung, Ying-Chung Chen, Chien-Chuan Cheng, Kuo-Sheng Kao, Thin Solid Films 516 (2008) 5277–5281
[13] S. Akiyama, F.J Grawert, J. Liu, K. Wada, G.K Celler, L.C Kimerling and F.X Kaertner, "Fabrication of highly reflecting epitaxy-ready Si-SiO_2 Bragg reflectors", *IEEE Photonics Technology Letters*, **17**, 1456-1458 (2005)
[14] Solidly mounted resonators consisting of a molybdenum and titanium Bragg reflector, Ching-Liang Wei, Ying-Chung Chen, Chien-Chuan Cheng, Kuo-Sheng Kao, Appl. Phys. A 90, 501–506 (2008)
[15] M.J.P. Musgrave, Crystal acoustics – Introduction to the study of elastic waves and vibrations in crystals (Holden-Day, 1970)
[16] A.P. Cracknell, *Ultrasonics* (Wykeham Publication, 1980)
[17] 'Random heterogenous materials : microstructure and macroscopic properties', Salvatore and Torquato, ISBN 0387951679, New York (2001)
[18] T.J. Plona, "Observation of a second bulk compressional wave in a porous medium at ultrasonic frequencies," *Appl. Phys. Lett.* **36**, (4) 259-261 (1979)
[19] J.D. Eshelby, "The determination of the elastic field of an ellipsoidal inclusion, and related problems," *Proc. Royal Society of London A, Math. and Phys. Sciences* **241**, No. 1226, 376-396 (1957)
[20] J.D. Eshelby, "The elastic field outside an ellipsoidal inclusion," *Proc. Royal Society of London A, Math. and Phys. Sciences* **252**, No. 1271, 561-569 (1959)
[21] R.E. Challis, M.J.W. Povey, M.L. Mather, and A.K. Holmes, "Ultrasound techniques for characterizing colloidal dispersions," *Rep. Prog. Phys.* **68**, 1541-1637 (2005)
[22] B.A. Auld, Acoustic fields and waves in solids vol. 1 2nd Ed (RE Kreiger, 1990)
[23] D.C. Kay, Theory and problems of tensor calculus (McGraw-Hill, 1988)
[24] J.F. Nye, *Physical properties of crystals – Their representation by tensors and matrices* (Oxford University Press, 1985)
[25] Solid State Physics, Gerald Burns, Academic Press Inc. ISBN 0-12-146070-3 (1990)
[26] G. T. Andrews, J. Zuk, H. Kiefte, M. J. Clouter, and E. Nossarzewska-Orlowska, Appl. Phys. Lett. **69** 1217 (1996)
[27] 'Elastic Properties of Porous Silicon Superlattices', Anna Maria Polomska, PhD Thesis, Department of Physics and Physical Oceanography, Memorial University of Newfoundland (2009)
[28] A. Cazzani and M. Rovati, "Extrema of Young's modulus for cubic and transversely isotropic solids", *International Journal of Solids and Structures*,**40**, 1713-1744 (2002)
[29] Mechanical properties of Si *http://www.ioffe.ru/SVA/NSM/Semicond/Si/mechanic.html#Elastic*

[30] P. N. Keating, 'Theory of the Third-order Elastic Constants of Diamond-Like Crystals', Phys Rev **149** 674 (1966)
[31] T. Böhlke and C. Brüggemann, "Graphical representation of the generalized Hooke's law," *Technische Mechanik* **21**, 145-158 (2001)
[32] B.A. Auld, Acoustic fields and waves in solids vol. 1 2nd Ed (RE Kreiger, 1990)
[33] M. Moret, S. Ruffenach, O. Briot, B. Gil, and R.L. Aulombard, "High Reflectivity AlGaN/GaN Bragg Mirrors Grown by MOCVD for Microcavities Applications", Materials Research Society
[34]Saddik, Boesch, Stemmer and York, *Appl. Phys. Lett.* **91**, 043501 (2007)
[35] P.A. Snow, E.K. Squire, P.St.J. Russell and L.T Canham, "Vapor sensing using the optical properties of porous silicon Bragg mirrors", *J. Appl. Phys.* **86**, 1781-1784 (1999)
[36] P. Allcock and P.A. Snow, "Time-resolved sensing of organic vapors in low modulating porous silicon dielectric mirrors, *J. Appl. Phys.* **90**, 5052-5057 (2001)
[37] V. Torres-Costa and R.J. Palmer J. Mater Sci **45,** 2823 (2010)
[38] F. Cunin, T.A. Schmedake, J.R. Link, Y.Y. Li, J. Koh, S.N. Bhatia, and M.J. Sailor, Nature Mat. **1** 39 (2002)
[39] E. Lorenzo, C. J. Oton, N. E. Capuj, M. Ghulinyan, D. Navarro-Urrios, Z. Gaburro and L. Pavesi, Appl. Opt, **44** (26), 5415 (2005)
[40] S. Ilyas, T. Böcking, K. Kilian, P. J. Reece, J. Gooding, K. Gaus, M. Gal, Opt. Mat. **29**, 619 (2007)
[41] A. Reinhardt and P. A. Snow, Phys. Stat. Sol, **204** (5), 1528 (2007)
[42] L. C Parsons and G. T Andrews, Appl. Phys. Lett, **95,** 241909 (2009)
[43] G. N. Aliev, B. Goller, D. Kovalev and P. A. Snow, Appl. Phys. Lett, **96**, 124101 (2010)
[44] G. N. Aliev, B. Goller, D. Kovalev and P. A Snow, Phys. Stat. Sol C **6** 1670 (2009)
[45] Phonon Dispersion in Silicon Nanocrystals, Valentin et al, J. Phys.: Conf. Ser. **92** 012048 (2007)
[46] 'Zone-Folded Longitudinal Acoustic Phonons In Porous Silicon Superlattices', Parsons and Andrews
[47] Kuo, Pan, and Pu, J. Appl. Phys. **103**, 093533 (2008).
[48] S.M.Rytov, Sov. Phys. *Acoust 2*, **68** (1956)
[49] W. H. Southwell, J. Opt. Soc. Am. A, **5** (9), 1558 (1988)
[50] B. G. Bovard, Appl. Opt, **32** (28), 5427 (1993)
[51] 'Porous Silicon Microcavities', Review by Claudio Vinegoni, Massimo Cazzanelli and L Pavesi, (2000)
[52] Han-Youl Ryu, Hong-Gyu Park, and Yong-Hee Lee, IEEE Journal of Selected Topics in Quantum Electronics **8**, 891 August (2002)
[53] REECE PJ et al. Appl Phys Lett **81** 4895 (2002)
[54] V. Lehmann, Electrochemistry of Silicon: Instrumentation, Science, Materials and Applications (Wiley-VCH, Weinheim, Germany, 2002).
[55] R. W. Fathauer, T. George, A. Ksendzov, and R. P. Vasquez, "Visible luminescence from silicon wafers subjected to stain etches," *Appl. Phys. Lett.* 60, 995-997 (1992).
[56] V. Lehmann, R. Stengl and A. Luigart, On the morphology and the electrochemical formation mechanism of mesoporous silicon, Materials Science and Engineering B 69, 11 (2000)
[57] B. A. Auld, *Acoustic Fields and Waves in Solids*, 2nd ed. Krieger, Malabar-Florida, (1990), Vol. 1.
[58] Dynamics of porous silicon formation by etching in HF + V_2O_5 solutions, Kurt W. Kolasinski, Justin D. Hartline, Bryan T. Kelly, Julia Yadlovskiy, **108** issue 7 & 9 (2010) 1033-1043.
[59] P. Allongue, "Porous silicon formation mechanisms," in *Properties of Porous Silicon*, L. Canham, ed., (INSPEC, London, UK, 1997) 3-11.
[60] Cellular solids structure and properties, Lorna J. Gibson, Michael F. Ashby, Cambridge University Press (1999) ISBN: 0521495601
[61] S. Setzu, G. Lerondel, and R. Romestain, "Temperature effect on the roughness of the formation interface of p-type porous silicon," *J. Appl. Phys.* 84, 3129-3133 (1998).
[62] Optical properties of multilayered porous silicon S. Setzu a,b, P. Ferrand a, R. Romestain a, Materials Science and Engineering B69–70 (2000) 34–42
[63] Roughness of the porous silicon dissolution interface G. Lerondel,a) R. Romestain, and S. Barret J. Appl. Phys. 81 (9), 6171 (1997)
[64] F. Frascella, Fabrication and modification of porous silicon layered and multilayered structures for optical sensing devices, PhD thesis 2008.
[65] A. Halimaoui, "Porous silicon formation by anodisation," in *Properties of Porous Silicon*, L. Canham, ed., (INSPEC, London, UK, 1997) 12-22.
[66] G. Sotgiu, L. Schirone, and F. Rallo, "On the use of surfactants in the electrochemical preparation of porous silicon," *Thin Solid Films* **297**, 18-21 (1997).

[67] V. Chamard, G. Dolino, and F. Muller, Origin of a parasitic surface film on p+ type porous silicon, Journal of Applied Physics 84, 6659 (1998)
[68] 'Influence of experimental parameters on physical properties of porous silicon and oxidized porous silicon layers', J. Charrier, V. Alaiwan, P. Pirasteh, A. Najar, M. Gadonna, Applied Surface Science **253** 8632 (2007)
[69] M. Thönissen, M. G. Berger, S. Billat, R. Arens-Fischer, M. Krüger, H. Lüth, W. Theiss, S. Hillbrich, P. Grosse, G. Lerondel, U. Frotscher, 'Analysis of the depth homogeneity of p-PS by reflectance measurements', Thin Solid Films **297** (1997) 92-96
[70] J. Charrier, V. Alaiwan, P. Pirasteh, A. Najar, M. Gadonna, Applied Surface Science **253** 8632–8636 (2007)
[71] Electronic States and Luminescence in Porous Silicon Quantum Dots: The Role of Oxygen, M. V. Wolkin, J. Jorne, P. M. Fauchet, G. Allan and C. Delerue **82** 1 Phys. Rev. Lett. (1999)
[72] Andrew Briggs, *Acoustic Micoscopy* 2nd Ed. ISBN 9780199232734 (2010)
[73] E. Lorenzo, C. J. Oton, N. E. Capuj, M. Ghulinyan, D. Navarro-Urrios, Z. Gaburro, and L. Pavesi, Appl. Opt. 44, 5415 (2005).
[74] S. Ilyas, T. Böcking, K. Kilian, P. J. Reece, J. Gooding, K. Gaus, and M. Gal, Opt. Mater. **29**, 619 (2007).
[75] P. A. Snow, E. K. Squire, P. St. J. Russell, and L. T. Canham, J. Appl. Phys. **86**, 1781 (1999).
[76] V. Torres-Costa and R. J. Palmer, J. Mater. Sci. **45**, 2823 (2010).
[77] F. Cunin, T. A. Schmedake, J. R. Link, Y. Y. Li, J. Koh, S. N. Bhatia, and M. J. Sailor, Nature Mater. 1, 39 (2002).
[78] A. de Bernabé, R. Jiménez, M. García-Hernández, and C. Prieto, Thin Solid Films **317**, 255 (1998).
[79] M. Grimsditch, R. Bhadra, I. K. Schuller, F. Chambers, and G. Devane, Phys. Rev. B 42, 2923 (1990).
[80] M. S. Salem, M. J. Sailor, T. Sakka and Y. H. Ogata, JAP **101** 063503 (2007)
[81]W. H. Southwell, J. Opt. Soc. Am. A **5**, 1558 (1988).
[82] W. H. Southwell, Appl. Opt. 36, 314 (1997).
[83] A. Reinhardt and P. A. Snow, Phys. Status Solidi **204**, 1528 (2007).
[84] Rugate Filter with Specified Bandwidth: a New Rule of Thumb, W. H. Southwell, TuD3.pdf OSA/OIC (2007)
[85] S. Setzu, P. Ferrand, R. Romestain, Materials Science and Engineering B69–70 (2000) 34–42
[86] 'Refractive Indices of Infrared Optical Materials and Color Correction of Infrared Lenses', Herzberger and Salzberg, JOSA **52** 420 (1962)
[87] 'Colour Correction in Optical Systems and a New Dispersion Formula', Journal of Modern Optics, 6:3, 197 - 215
[88] 'Properties of Group IV, III-V and II-VI Semiconductors', Sadao Adachi, ISBN 0-470-09032-4 Wiley (2005)
[89] Properties of Porous Silicon, Edited by Canham, Leigh © 1997 Institution of Engineering and Technology
[90] 'Form-Anisotropy of 2d Nanostructures: Modelling Approaches Comparison', A. Lutich, N. Gaponik, A. Eychmüller and S. Gaponenko, Phys. Stat. Sol. A (2009) **206** 2834
[91] 'Colours in Metal Glasses and in Metallic Films', J. C. Maxwell Garnett, Philos. Trans, R. Soc. London 203, 385 (1904)
[92] Aliev, Snow, Goller and Kovalev, PSST Conference (2008)
[93] R.J.M. Da Fonseca, J.M. Saurel, A. Foucaran, J. Camassel, E. Massone, T. Taliercio and Y. Boumaiza, *J. Ma-ter Sci*., **30**, 35 (1995).
[94] H.J. Fan, M.H. Kuok, S.C. Ng, R. Boukherroub, J.-M. Baribeau, J.W. Fraser and D.J. Lockwood, *Phys. Rev. B*, **65**, 165330 (2002).
[95] 'Solidly mounted resonators consisting of a molybdenum and titanium Bragg reflector', Ching-Liang Wei, Ying-Chung Chen, Chien-Chuan Cheng, Kuo-Sheng Kao, Appl. Phys. A 90, 501–506 (2008)
[96] Y.P. Zhao, I. Wu, C.F. Cheng, U. Block, G.C. Wang and T.M. Lu, "Characterization of random rough surfaces by in-plane light scattering," *J. Appl. Phys.* **84**, 2571-2582 (1998)
[97] Y.P. Zhao, G.C. Wang and T.M. Lu, "Diffraction from non-gaussian rough surfaces," *Phys. Rev. B* **55**, 13 938- 13 952 (1997)
[98] S. Setzu, P. Ferrand, and R. Romestain, "Optical properties of multilayered porous silicon," Mat. Sci. and Engin. **B69-70** 34-42 (2000)
[99] G. Lerondel and R. Romestain, "Fresnel coefficients of a rough interface," *Appl. Phys. Lett.* **74**, (19) 2740-2742 (1999)

[100] G. Lerondel ,R. Romestain, and S. Barret, "Roughness of the porous silicon dissolution interface," *J. Appl. Phys.* **81**, 6171-6178 (1997)
[101] H. E. Bennett and J. O. Porteus, JOSA **51** 123 (1961)
[102] 'Derivation of a matrix describing a rugate dielectric thin film', Bertrand G. Bovard, Applied Optics, **27** 1998 (1988)
[103] 'Principles of Optics', Born and Wolf, Third Revised Edition (1965)
[104] C. L. Mitsas and D. I. Siapkas, Appl. Opt. **34**, 1678 (1995)
[105] Image courtesy of University of Florida

[106] M. G. Berger, R. Arens-Fischer, M. Thönissen, M. Krüger, S. Billat, H. Lüth, S. Hilbrich, W. Theiß, and P. Grosse, Thin Solid Films 297, 237 (1997)

[107] W. H. Southwell, Appl. Opt. 36, 314 (1997).

[108] Rugate filter sidelobe suppression using quintic matching layers, Southwell 1989

[109] 'Using apodization functions to reduce sidelobes in rugate filters', William H. Southwell 28, 23 Applied Optics (1989)

[110] Lorenzo et al. Appl Optics 44 5415 (2005)

[111] 'Dichroic rugate filters based on birefringent porous silicon', Ishikura et al, Optics Express, 16, 20, 15538 (2008)

[112] A. Kent, A. Akimov, W. Maryam and E. Young at the University of Nottingham 2010.

[113] L. J. Gibson and M. F. Ashby, Cellular Solids: Structure and Properties, (CUP, Cambridge, 1999)
[114] J. He, J. Sapriel, R. Azoulay, Phys. Rev. B **40** 1121 (1989)
[115] International Dictionaries of Science and Technology- SOUND, 1974
[116] S. Kocis and Z. Figura, *Ultrasonic measurements and technologies* (Chapman and Hall, 1996)
[117] B.A. Auld, *Acoustic fields and waves in solids vol. 1 2nd Ed* (RE Kreiger, 1990)
[118] Journal of the Acoustical Society of America, **36** 644 (1964)
[119] R.E. Challis, M.J.W. Povey, M.L. Mather, and A.K. Holmes, "Ultrasound techniques for characterizing colloidal dispersions," *Rep. Prog. Phys.* **68**, 1541-1637 (2005)
[120] S. Setzu, P. Ferrand, and R. Romestain, "Optical properties of multilayered porous silicon," Mat. Sci. and Engin. **B69-70** 34-42 (2000)
[121] S.E. Foss, P.Y.Y. Kan, and T.G. Finstad, "Single beam determination of porosity and etch rate *in situ* during etching of porous silicon," *J. Appl. Phys.* **97**, 114909 (2005)
[122] H.E. Bennett and J.O. Porteus, "Relation between surface roughness and specular reflectance at normal incidence," *J. Opt. Soc. Am*. **51**, 123-129 (1961)
[123] L. Lin, *On the generation and detection of ultrasonic plate waves in microporous polymeric material* (Ph.D thesis, Beijing Polytechnic University, 2003)
[124] G. Lerondel and R. Romestain, "Fresnel coefficients of a rough interface," *Appl. Phys. Lett.* **74**, (19) 2740-2742 (1999)
[125] G. Lerondel ,R. Romestain, and S. Barret, "Roughness of the porous silicon dissolution interface," *J. Appl. Phys.* **81**, 6171-6178 (1997)
[126] 'Relation Between Surface Roughness and Specular Reflectance at Normal Incidence', H. E. Bennett and J. O. Porteus, JOSA **51** 123 (1960)
[127] W.P. Mason and T.B. Bateman, "Ultrasonic wave propagation in doped n-germanium and p-silicon," *Phys. Rev.* **134**, (5A) 1387-1396 (1964)
[128] W.P. Mason and T.B. Bateman, "Ultrasonic attenuation and velocity changes in doped n-type silicon and their use in determining an intrinsic electron and hole scattering time," *Phys. Rev. Lett.* **10**, 151-154 (1963)
[129] 'Ultrasonic attenuation in amorphous silicon at 50 and 100 GHz', D. B. Hondongwa, B. C. Daly, T. B. Norris, B. Yan, J. Yang and S. Guha, Phys. Rev. B **83** 121303 (2011)
[130] R.J.M. Fonseca, J.M. Saurel, A. Foucaran, J. Camassel, E. Massone, and T. Taliercio, "Acoustic investigation of porous silicon layers," *J. Mat. Sci.* **30**, 35-39 (1995)
[131] P. N. Keating, 'Theory of the Third-order Elastic Constants of Diamond-Like Crystals', Phys Rev **149** 674 (1966)
[132] G.T. Andrews, *Elastic and structural properties of supported porous silicon layers* (Ph.D thesis, Memorial University ofNewfoundland, 1999)

[133] P. N. Keating, 'Theory of the Third-order Elastic Constants of Diamond-Like Crystals', Phys Rev **149** 674 (1966)
[134] D. Bellet, P. Lamagnere, A. Vincent, and Y. Brechet, "Nanoindentation investigation of the Young's modulus of porous silicon," *J. Appl. Phys.* **80**, 3772-3776 (1996)
[135] C.T. Herakovich and S.C. Baxter, "Influence of pore geometry on the effective response of porous media," *J. Mat. Sci.* **34**, 1595-1609 (1999)
[136] C.K, Young, G.T Andrews, M.J. Clouter, Y. Ke, W.J, Choyke, A. Polomska, and R.P. Devaty, "Brillouin spectra of porous p-type 6H-SiC," *Materials science forum vols*. **527-529**, (2006)
[137] L.P. Chao and J.H. Huang, "Prediction of elastic moduli of porous materials with equivalent inclusion method," J. Reinforced Plastics and Composites, **18**, 592-605 (1999)
[138] Y. Shishkin, Y. Ke, W.J, Choyke, and R.P. Devaty, "Fabrication and morphology of porous p-type SiC," *J. Appl. Phys.* **97**, 044908 (2005)